2015

Study of Periodic Forcing with a Dielectric Barrier Discharge Device for the Control of Flow Separation on a NACA 0012

Joseph P. Dygert

Study of Periodic Forcing with a Dielectric Barrier Discharge Device for the Control of Flow Separation on a NACA 0012

Joseph P. Dygert

Thesis submitted to the
Benjamin Statler College of Engineering and Mineral Resources
at West Virginia University
in Partial Fulfillment of the Requirements
for the degree of

Master of Science
in
Aerospace Engineering

Patrick H. Browning, Ph.D.
Wade Huebsch, Ph.D.
John Kuhlman, Ph.D.

Department of Mechanical and Aerospace Engineering

Morgantown, West Virginia
2015

Keywords: Dielectric Barrier Discharge, Electrohydrodynamics, Plasma Aerodynamics, Active Flow Control

ABSTRACT

Study of Periodic Forcing with a Dielectric Barrier Discharge Device for the Control of Flow Separation on a NACA 0012

Joseph P. Dygert

The continued high global demand for passenger and freight air traffic as well as increased use of unmanned aerial vehicles (UAVs), in spite of rising fuel costs and several tragic cases involving loss-of-control events, has resulted in researchers examining alternative technologies, which would result in safer, more reliable, and better performing aircraft. Aerodynamic flow control may be the most promising approach to this problem having already proven its ability to enable higher flow efficiency while also simultaneously improving overall flow control. Recent research in the area of aerodynamic control is transitioning from traditional mechanical flow control devices such as slats and flaps to plasma actuators. Plasma actuators offer an inexpensive and energy efficient method of flow control. In addition, plasma actuator technology has the potential of application to a host of other aircraft performance parameters including applications in radar mitigation and in situ wing deicing.

Dielectric Barrier Discharge (DBD), one of the most widely studied forms of plasma actuation, employs an electrohydrodynamic (EHD) device, which uses dominant electric fields and the respective electrically related body forces for actuation. Unlike momentum jets or other traditional flow control methods used on wings and tail surfaces, a DBD device operates without moving components or injecting any mass into the flow stream.

Work performed focuses on qualitatively investigating experimentally the use of DBD devices for flow separation control on a NACA 0012-based 2D wing model. Flow visualization techniques illuminated flow seed particles around the model to determine the state of the flow (i.e., attached or separated) for various actuator cases. The DBD was operated in a steady-on mode as well as for three different pulsing frequencies (only for low power testing) based on the Strouhal frequency for each flight condition and compared to the clean (i.e., plasma off) case. Some of the flow control results were compared to another active flow control scheme known as dynamic roughness (DR) which consists of surface mounted time dependent deforming elements that operate as a periodic forcing device that energizes the boundary layer. The potential use of DBDs for application to existing UAVs and aircraft was also evaluated based on applicability, power consumption, and other relevant factors.

Results of this work indicate that low power gapless DBD actuators are an effective form of separation control at low Reynolds numbers $\dot{O}(10^4)$ near the angle of attack where separation begins to occur. However, testing seems to indicate that gapless low power DBDs are underpowered to have any substantial flow control authority at higher Reynolds numbers and angles of attack. With improved materials for DBD construction and more testing, DBDs could potentially be an effective form of flow control on UAVs and manned aircraft in the future.

Dedication

I would like to dedicate this thesis to my father, Eric Dygert. At a young age he instilled in me the sense of importance to have a strong work ethic, to be honest, to plan for the future, to be observant, and to always “use your head”. He’s one the hardest working, intelligent persons I’ve ever known and is responsible for the person I am today.

Acknowledgements

I would like to acknowledge;

My advisor and committee chair, Dr. Patrick Browning, for his many hours of hard work and guidance. Without him, I would have been rather lost at times.

My committee members, Dr. Wade Huebsch and Dr. John Kuhlman, for their input and guidance.

Dr. Melissa Morris, for showing up at my house one morning with approximately 50 papers on various plasma aerodynamics aspects and demanding a summarized version of each within a month. She helped get me started on the road to graduation and success, and for that, I am very grateful.

Vinay Jakkali, for providing data from the dynamic roughness testing for comparison to my results and for providing data for the free stream turbulence intensity and the velocity profile of the wind tunnel.

Cory Villa of Corona Magnetics Inc., for his advice and help with selecting step-up transformers as well as guidance on safely operating them.

Dr. George Laity of Sandia National Laboratories, for his guidance on plasma related topics.

My undergraduate team: Amos Powell, Mike Fritzinger, Alexa Tweedlie, and Magdalena Krasny; for all their help in completing my experimental testing, even when it seemed like it would never be finished.

Lastly, I would like to thank my friends and family.

Table of Contents

List of Figures

List of Tables

Nomenclature

Abbreviations

A	Amperes
AC	Alternating current
DBD	Dielectric barrier discharge
CAD	Computer aided drafting
cm	centimeter
CNC	Computer numerically controlled
DC	Direct current
DR	Dynamic roughness
EHD	Electrohydrodynamics
EMP	Electromagnetic pulse
ft	feet
Hz	Hertz
in.	inch or inches
kHz	kilohertz
kV	kilovolts
LOC	Loss of control
NACA	National Advisory Committee for Aeronautics
m	Meter
mAh	milliampere hours
MHD	Magnetohydrodynamics
mm	Millimeter
Re	Reynolds number
RLC	resistive, inductive and capacitive circuit
S	Seconds
TI	Turbulence Intensity
UV	Ultraviolet
UAS	Unmanned aerial system
UAV	Unmanned aerial vehicle
V	Volts

VUV	Vacuum ultraviolet
W	Watts

Symbols

%BL	Percent blockage
δ(a)	Uncertainty in quantity “a”
Δ	Change in
°	Degrees
$\mathcal{O}$	On the order of magnitude of
$\boldsymbol{\alpha}$	Angle of attack
A	Area
$\boldsymbol{B}$	Magnetic field
c	Chord length unless otherwise stated as speed of light
CA	Cross sectional area
D	Diameter
$\boldsymbol{E}$	Electric field
f, f	Frequency
g	Gravitational acceleration
h	Height
$\mathcal{L}$	Gap length
L	Length
P	Pressure
p	Power
ρ	Density
R	Radius or universal gas constant
Re	Reynolds number
S	Span
St	Strouhal number
t	Thickness
T	Temperature
T	Thrust
u(a)	Relative uncertainty of quantity “a”
U	Free stream velocity

μ	Dynamic viscosity
V	Voltage
W	Width
Y	Y-component of object

Subscripts

1	Position 1
2	Position 2
a	Ambient condition
ce	Covered electrode
d	Disk
ee	Exposed electrode
e	Electron
frontal	Frontal projection
i	Ion
le	Leading edge
ley	Leading edge y-component
n	Neutral
op	Operational/operating
r	Ratio
rms	Root mean square
St	Strouhal number
ts	Test section
wing	With respect to the wing model
y	y-component

Introduction

With the world seeing a pronounced growth in the use of unmanned aerial vehicles (UAVs) in many civilian and military sectors, primarily in the area of small and miniaturized unmanned aerial systems (UAS), there is a renewed interest in low Reynolds number aerodynamics. The small size and slow cruise speeds of UAVs compared to traditional aircraft place the majority of these vehicles' operating regimes in a Reynolds number range of $10^4 – 10^5$ [1]. With these vehicles operating in low Reynolds number regimes they are susceptible to the presence of leading edge separation of the boundary layer at high angles of attack. This condition is critically important because it can lead to stall and possibly lead to catastrophic loss of control (LOC) events [2]. A study conducted by Tani, shows the presence of a separation bubble as shown in Figure 1, which occurs when the boundary layer detaches from the airfoil surface and further downstream reattaches to form a turbulent boundary layer [2]. The Reynolds number of the flow predominantly influences the size of the separation bubble and even a small disturbance can cause the bubble to burst. If the flow cannot naturally reattach due to entrainment of the flow from turbulence then the separation on the upper surface of the airfoil leads to stall.

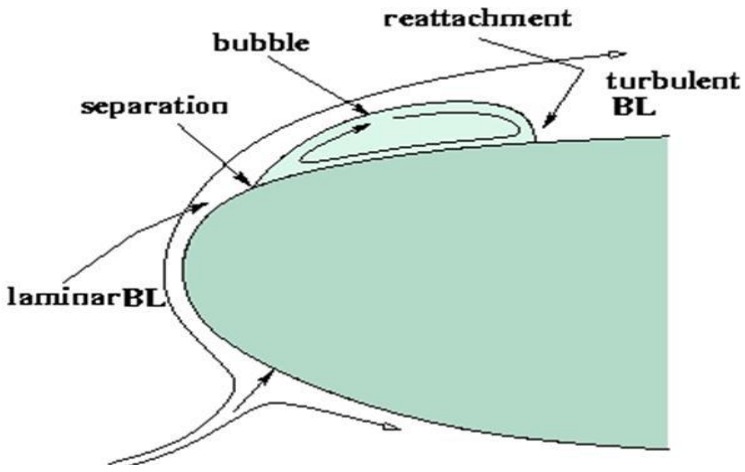

Figure 1: Laminar separation bubble [2]

Aiming to improve the performance of an airfoil at high angles of attack by eliminating leading edge separation, many different flow control techniques have been developed. Flow control techniques can be classified into both passive and active control methods. Some of the passive techniques include the use of static roughness or compliant walls, while some of the active methods involve blowing, suction, and controlled motion of the solid wall. One of these active control methods that is receiving increased levels of interest is the use of various types of plasma actuators. Plasma actuators typically involve some electrode configuration supplied with some high voltage current (either direct or alternating) and can include arrangements of various magnets. Devices or actuators that have electric fields $\boldsymbol{E}$ that follow the relationship as seen in Eq. (1);

$$\boldsymbol{E} > \boldsymbol{B}c \qquad \textbf{Eq. (1)}$$

where c is the speed of light and $\boldsymbol{B}$ is the magnetic field are known as electrohydrodynamic (EHD) devices [3]. This would lead to body forces related to the electrical field being significantly larger than magnetic related body forces. If the magnetic field, either produced by current or by magnets, is large in comparison to the electric field then the devices are classified as magnetohydrodynamic (MHD) devices. This would result in magnetic body forces being significantly larger than electric body forces. Both types of devices have seen an increased interest in the study of flow control in various regimes due to their versatility, robustness due to lack of moving parts, and their numerous variables available for optimization, such as materials, various geometries and electrical characteristics. One of the EHD devices that has shown much interest to researchers is the dielectric barrier discharge (DBD), a configuration of electrodes with an insulating barrier powered by alternating current (AC). Various research groups have studied parameter optimization of DBDs such as frequency, voltage, voltage waveform, dielectric constant, and geometries [4] [5] [6] [7]. Groups have also studied other aspects such as the underlying physics of operation, chord placement, use of multiple actuators, and hybridization of actuators, among many others, with intents of maximizing flow control authority [8] [9] [10]. One of the areas that has been studied is the use of a DBD

as a pulsed or periodic forcing mechanism for increased lift, decreased drag, stall delay, and flow reattachment with the majority of periodic forcing flow control with DBDs moving into the regime of nanosecond pulsing [11] [12] [13]. This may however be unnecessary as many studies of periodic forcing show great potential when pulsed at a frequency that makes the Strouhal number equal to 1 (unity), also known as the Strouhal frequency. A DBD actuator dissipates more power in the form of dielectric heating at higher frequencies, and it often requires more complicated electrical circuits, so it could be favorable to operate them at lower pulsing frequencies consisting of lower base frequencies. Some of the devices studied for periodic forcing have been DBDs, synthetic jets, and dynamic roughness. Synthetic jets are a form of active flow control that operate by utilizing orifices that can be actuated usually via some membrane that allows for suction and ejection of fluid from and into the flow stream. They are inherently a periodic forcing device [14]. Dynamic roughness (DR) is another form of active flow control and is a form of periodic forcing, often used for the purpose of flow separation control. As opposed to static roughness, dynamic roughness utilizes small time-dependent surface mounted deforming elements or humps with amplitudes that are on the order of the local boundary layer height, to energize the local boundary layer. The deforming elements are pulsed/operated at various frequencies. Earlier studies conducted by researchers including, Grager et al. and Jakalli et al. , have indicated that at low Reynolds numbers, DR is effective in eliminating leading edge laminar separation bubbles, and is capable of reattaching completely separated flow at higher angles of attack [15] [16].

Problem Statement

With increased research into DBD flow control actuators, it is clear that they are physically viable devices for application to the delay or prevention of flow separation, and even for use for flow reattachment. However many of the studies done on flow separation with DBDs focus on steady operations or have moved into the nanosecond pulsing regime. Nanosecond pulsing shows promising results for improved aerodynamic characteristics but with faster pulsing repetitions it is required to operate at a high base AC frequency from which the pulses are made. With dielectric barrier heating effects being proportional to operational AC frequency, this allows for much of the converted electrical energy to go into waste heat instead of channeling into direct use for flow modification. These high frequencies also often require impedance matching circuits to attempt to match with the transformer's resonant frequency to prevent unnecessary power loss. Studies on periodic forcing mechanisms often show a significant increase in stall prevention as well as improved aerodynamic characteristics when operated at a frequency that sets the Strouhal number equivalent to unity, which in the case of UAV flight is many orders of magnitude lower than nanosecond pulsing, which would in turn require a lower base frequency. *The fundamental problem under study in the current work is whether a DBD, operated with a pulsed frequency near the Strouhal frequency with a base frequency matched to the circuit resonant frequency, can be an effective and efficient form of stall prevention and flow reattachment at low Reynolds numbers.*

Objectives

The goal of this work is to establish whether a DBD operated at low power per unit span (approx. 57 W/m for steady operation) and at pulsing frequencies near the Strouhal frequency is an effective and feasible form of flow separation control. This goal will be met by performing work to satisfy the following three objectives:

1. Investigate the control authority for flow separation of a dielectric barrier discharge as a method of periodic forcing near Strouhal number (*St*) equal to unity with a comparison of some operating cases to dynamic roughness (DR).
2. Compare the power requirements needed to operate both the DBD and DR systems.
3. Investigate the future feasibility of use of dielectric barrier discharge.

Review of Relevant Literature

History of Plasmas and Gaseous Electronics

In 1879, Sir William Crookes said to an audience at a meeting of the British Association for the Advancement of Science, regarding the work he had been performing with mysterious rays in "vacuum" tubes and glowing ores:

> ***"So distinct are these phenomena from anything which occurs in air or gas at the ordinary tension, that we are led to assume that we are here brought face to face with matter in a fourth state or condition, a condition so far removed from the state of gas as a gas is from a liquid. In studying this fourth state of matter we seem at length to have within our grasp and obedient to our control the little indivisible particles which with good warrant are supposed to constitute the physical basis of the universe…We have actually touched the border land where matter and force seem to merge into one another, the shadowy realm between known and unknown, which for me has always had peculiar temptations. I venture to think that the greatest scientific problems of the future will find their solution in this border land, and even beyond; here it seems to me, lie ultimate realities, subtle, far-reaching, wonderful [17]."***

The mysterious and intriguing, fourth state of matter that Crookes was discussing is now widely termed as plasma. The word plasma originates from the Greeks, meaning, "formed" or "molded" and in the mid nineteenth century the Czech physiologist used it to designate the clear fluid medium in blood that holds the other cells in place. In 1922, American Scientist Irving Langmuir commented on how the electrons, ions, and neutrals are like the cells in a fluid medium he called plasma [18]. Presently we define plasma as

any state of matter that has enough free charges so that electromagnetic forces are dominant. In practice, quite modest degrees of ionization (even as low as 0.1%) can be classified as a plasma [19]. Table 1 shows a chronological order of discovery of aspects and phenomena in plasma physics [17].

Table 1: Table of discoveries relating to plasma physics [17]

Date	Concept	Originator
1600	Electricity	William Gilbert
1742	Sparks	John Theophilus Desaguliers
1808	Diffusion	John Dalton
1808	Arc(discharge)	Humphry Davy
1817	Mobility	Michael Faraday
1821	Arc(name)	Humphry Davy
1834	Cathode and Anode	Michael Faraday
1834	Ions	Michael Faraday
1848	Striations	Jeremy Joseph Benoit Abria
1860	Mean Free Path	James Clerk Maxwell
1876	Cathode Rays	Eugen Goldstein
1879	Fourth State of Matter	William Crookes
1880	Paschen Curve	Warren de la Rue and Hugo Muller
1889	Maxwell-Boltzmann Distribution	Walther Nernst
1891	Electron(charge)	George Johnstone Stoney
1895	X rays	Wilhelm Conrad Röntgen
1897	Cyclotron Frequency	Oliver Lodge
1898	Ionization	William Crookes
1899	Transport Equations	John Sealy Townsend
1899	Energy Gain Equations	Hendrik Lorentz
1901	Townsend Coefficients	John Sealy Townsend
1905	Diffusion of Charged Particles	Albert Einstein
1906	Electron(particle)	Hendrik Lorentz
1906	Plasma Frequency	John William Strutt, 3rd Baron Rayleigh
1914	Ambipolar Diffusion	Hugo Von Seeliger
1921	Ramsauer Effect	Carl Ramsauer
1925	Debye Length	Peter Debye and Erich Hückel
1928	Plasma	Irving Langmuir
1935	Velocity Distribution Functions	William Phelps Allis

A common method of categorizing plasmas is to split them into two groups of thermal and non-thermal plasmas. Thermal plasmas are close to thermal equilibrium and have the following relationship:

$$T_e = T_i = T_n \qquad \textbf{Eq. (2)}$$

and also exhibit approximately Maxwellian temperature distributions. Examples of thermal plasmas include cutting torches, lightning, and stars. Non-thermal plasmas are not in thermal equilibrium and often have the following relationship:

$$T_e >> T_i \approx T_n \qquad \textbf{Eq. (3)}$$

with non-Maxwellian temperature distributions. Neon signs, fluorescent lights, and ozone generators are examples of non-thermal plasmas. Currently the majority of plasma physics research focuses on theory and technology aiming at achieving sustainable thermonuclear fusion. This is the case because fusion offers the potential for a nearly unlimited, safe, and secure energy source to combat predicted rises in global energy consumption. However plasma is beginning to prove useful in many areas such as industrial scale ozone production, medical and food sterilization and case, surface and materials processing and fabrication, plasma assisted ignition and combustion, and a wide range of aerodynamic applications [20].

Dielectric Barrier Discharge and other Barrier Discharges

Dielectric Barrier Discharge (DBD), also sometimes referred to as silent discharge (in contrast to an arc discharge), employs an electrohydrodynamic device that uses dominant electric fields and the respective electrically related body forces and generates a non-thermal plasma. DBDs are characterized by the presence of one or more dielectric insulating layers in the current path between the metal electrodes in addition to the discharge gap(s). A dielectric material, more commonly known as an insulator, prevents the flow of conduction current (flow of charged particles) below its break down value (dielectric strength) but does not impede electric fields. It is common in related literature for researchers to refer to DBD as either *symmetric* (i.e., both electrodes covered by dielectric) or *asymmetric* (i.e., with only one electrode placed under a dielectric layer). The content of this thesis will herein refer only to asymmetric DBDs due to the directional induced flow from an asymmetric DBD unlike that of a symmetric DBD, which makes asymmetric DBDs more widely studied for aerodynamic purposes. A discharge having at least one dielectric boundary has many similarities with discharges operated between metal electrodes. For example, the first ignition breakdown in a homogeneous electrical field is governed by the same Paschen law that is known from breakdown between metal electrodes [20]. This breakdown occurs once the applied voltage creates an electric field that surpasses the dielectric strength of air (but does not surpass the dielectric strength of the barrier) and the air becomes a plasma, which is a good conductor of electricity. Figure 2 shows a typical Paschen curve for air, nitrogen (N_2), and sulfur hexafluoride (SF_6) [21]. For example at a pressure of one atmosphere, air typically breaks down at roughly at 30kV/cm [22].

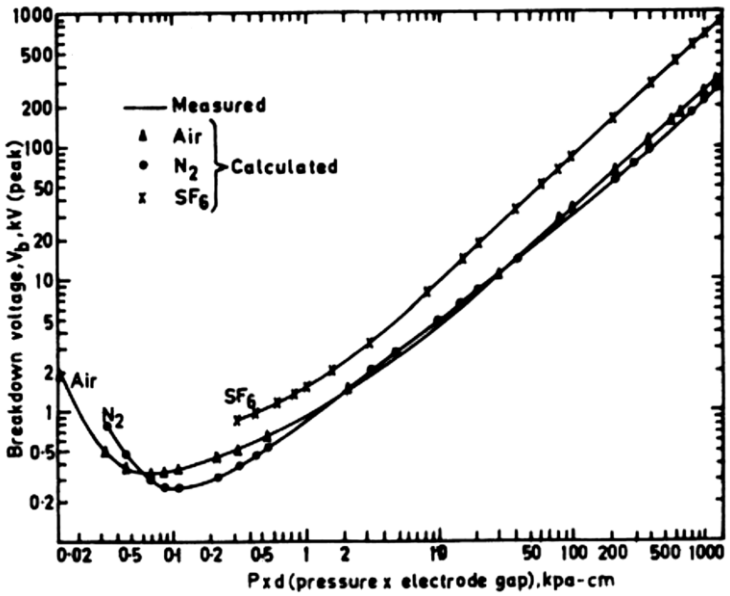

Figure 2: Typical Paschen breakdown curve [21]

After first ignition, charges deposit on the dielectric layer, alter the local electric fields, and dominate the operational behavior of the DBD device. One fundamental difference from discharges between bare metal electrodes is that DBDs cannot operate with direct current (DC) voltage potentials like most glow discharges because the capacitive coupling of the dielectric(s) and its prevention of conductive current flow necessitates an alternating electric field which drives a displacement current (time varying electric field) [20]. A DBD operates in two modes, which are commonly referred to as diffuse mode and filamentary mode. To the unaided eye, the diffuse mode seems like a continuous, diffuse, uniform glow; however, both modes are made up of "micro discharges" occurring at very high frequencies on the order of half the applied AC frequency which gives it the continuous appearance [23] [24]. In air at one atmosphere with any appreciable gap (i.e., a gap of more than a few millimeters), the diffuse mode is difficult to achieve and is very unstable. A slight change in any operating parameter (e.g., applied voltage, frequency, local variations in pressure, etc.) can cause transition to the more stable filamentary mode, which is more widely used in research and industrial applications [20]. Figure 3 depicts both modes of operation.

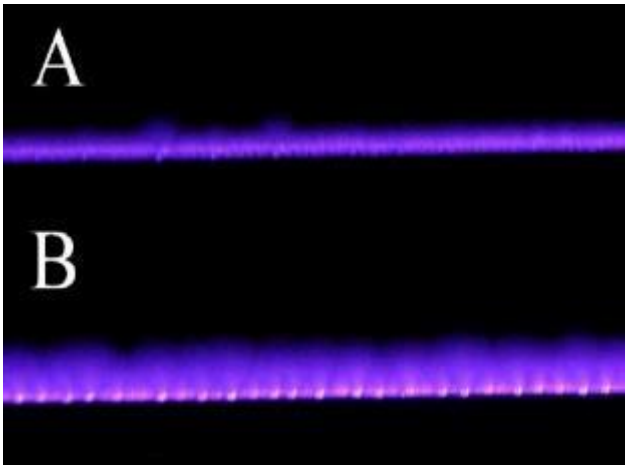

Figure 3: A) Diffuse mode B) Filamentary mode [23]

Several studies have been conducted in both operational regimes, to show that the produced thrust versus applied voltage follows an exponential relationship in the form of Eq. (4)

$$T \propto V_{rms}^{3.5} \quad \textbf{Eq. (4)}$$

This equation only holds prior to the onset of saturation [6]. As the applied voltage is increased, the actuator saturates and eventually arcs are formed between the electrodes through the dielectric, causing an electrical short and subsequent failure of the actuator. This occurs because the local electric field surpasses the dielectric strength of the barrier and it can no longer prevent conductive current. Once the actuator reaches its saturation point, the thrust versus applied voltage continues to follow an exponential relationship before arcing occurs, but of the form of Eq. (5) [6].

$$T \propto V_{rms}^{2.3} \quad \textbf{Eq. (5)}$$

During operation, a typical breakdown (creation of plasma region) is initiated with one free electron usually present due to cosmic radiation or from the previous discharge. When the electric field reaches the breakdown value, the free electron(s) produces secondary electrons by direct ionization of local fluid molecules and starts an electron avalanche. In certain cases, the avalanche can develop into a streamer,

also called a micro discharge, and once it reaches the dielectric barrier it builds up charge on the dielectric surface, collapsing the local electric field. This collapse of the local electric field leads to self-termination of the discharge [23]. The plasma ignites and extinguishes itself twice during each AC cycle. During the first half of the cycle, the voltage on the exposed electrode is negative-going. This is the “forward stroke” of the discharge, as referred to by researchers, where current travels from the exposed electrode to the surface of the dielectric. The current deposits charge on the dielectric surface, which then terminates the micro discharges. The actuator then enters its “backward stroke” once the applied voltage is positive-going. The electrons on the dielectric surface are now pulled back to the exposed electrode again colliding with and ionizing neutral particles in the gas along the way, and the plasma ignites for the second time in the AC cycle. The plasma quenches again once the voltage is no longer positive-going. An illustration of this is given in Figure 4.

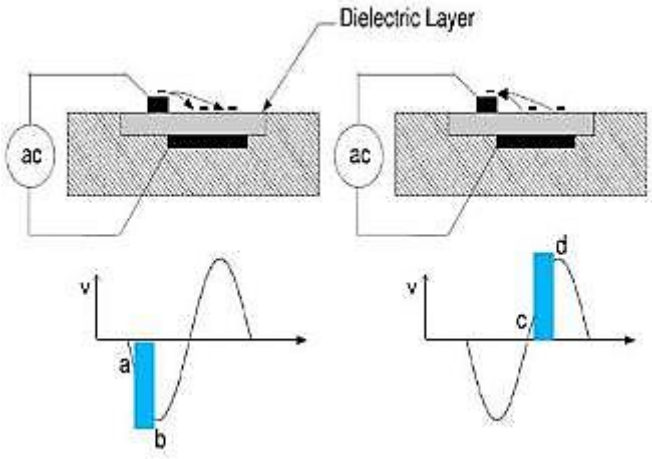

Figure 4: Forward stroke plasma formation) a to b; and
backward stroke plasma formation) c to d [4]

The number and structure of the plasma micro discharges are very different in the forward and backward discharges. In the forward stroke, there are more micro discharges; each micro discharge is more diffuse and carries less charge to the dielectric surface. In the backward stroke, there are fewer micro discharges; each micro discharge is more intense and carries more charge back to the exposed electrode. The forward stroke micro discharge current spikes are much smaller than the backward stroke micro discharge current

spikes. It should be noted that while the backward stroke current spikes are much larger than the forward stroke current spikes, the average current magnitudes for each half of the discharge are equal. This process repeats at such high frequency that it appears continuous to the human eye [24]. It is currently accepted that the bias in the current discharge is what gives rise to the preferred direction of momentum injection, with induced flow moving from the exposed electrode towards the covered electrode.

Other than dielectric barrier discharge, there exist several other types of barrier discharges, including resistive barrier discharges, sliding discharges and various other multiple electrode designs [9] [10] [25]. Resistive barrier discharge is similar to DBD in the sense that they are both electrode barrier discharges. In resistive barrier discharge however, there is a resistive barrier placed over one or all electrodes in place of the dielectric. This high-resistivity sheet plays the role of a distributed resistive ballast that inhibits the discharge current from reaching a high value and, therefore, prevents arcing [25]. Recent advances in barrier discharge research have led to the development of the so-called “sliding discharge”. By combining a surface dielectric barrier AC discharge together with a negative DC corona discharge at atmospheric pressure, a sliding discharge is generated. The ionization region of this discharge is considerably extended on the interelectrode gap with respect to that usually obtained with a pure DBD allowing for large interelectrode gap distances [9]. A DC corona discharge is an ionization of gases near a sharp edge of an electrode (usually a wire with small radius) or an electrode with small surface area with DC current.

Non-Aerodynamic Applications of DBDs

DBD devices have a wide range of applications to many areas due to their ability to operate within a wide range of geometries and operating conditions. Another important aspect of DBD devices is their non-thermal nature and the greater ease of obtaining this non-thermal equilibrium than with alternative techniques like low pressure discharges, fast pulsed high-pressure discharges or electron beam injection [20]. The most common usage of DBD devices in the past is for the generation of ozone (O_3) through plasma chemistry, which has been utilized on industrial sized scales. DBDs have also found a number of interesting industrial applications in addition to historical ozone generation. Choi et al. studied the mechanisms by which pulsed DBDs can be used for sterilization with regard to three different bacteria including E. coli [26]. Due to the wide range of plasma chemistry available on different time scales, DBDs have also been studied for their possible applications in air pollution control. Wilson et al. investigated cold oxidation techniques related to DBDs for possible modular air sterilization and air quality control devices [27]. The U.S Environmental Protection Agency has even studied the use of plasma devices including DBD for air pollution control [28]. Plasma assisted ignition and combustion have also become a noted area of study due to their possible applications for high speed flow combustion in devices such as supersonic/hypersonic jet engines [29] [30]. Various forms of surface cases on a range of materials have also increased interest in applications of DBDs. Borcia et al. investigated surface cases of polymer fibers and films. They studied the effects that duration, discharge energy and the inter-electrode gap distances had on wettability, wickability and the level of oxidation of the surface [31]. The generation of powerful coherent infrared radiation in CO_2 lasers and of incoherent ultraviolet (UV) or vacuum ultraviolet (VUV) excimer radiation in excimer lamps are the physical foundations of more recent developments in applications of DBDs. VUV excimer radiation generated in DBDs can excite phosphors to emit visible light. This is the basis of mercury-free fluorescent lamps and of flat plasma display panels [20].

Aerodynamic Applications of DBDs

In the past two decades, since J. Reece Roth obtained several U.S patents (5387842, 5414324, 5669583) on various plasmas and their generation techniques and his applications of them to flow control, DBDs have become one of the most widely studied forms of plasma actuation for flow control [32] [33] [34]. Unlike momentum jets or other traditional flow control methods used on wings, tails, and control surfaces, a DBD device operates without moving components or injecting any mass into the flow stream. It is currently accepted that DBD discharge can alter flow structures allowing for flow control due to four various processes: 1) momentum injection, 2) flow heating, 3) stream wise vortex generation, and 4) periodic forcing [23]. In momentum injection, the externally imposed electric field creates and accelerates free electrons and charged ions. Through collisions with neutrals, the ions and electrons impart momentum to the airflow, therefore increasing the overall momentum of the flow. This can be seen in Figure 5 and close up in Figure 6, where smoke during testing is accelerated towards the trailing edge of the wing from the leading edge location of the actuator with free stream velocity equal to zero.

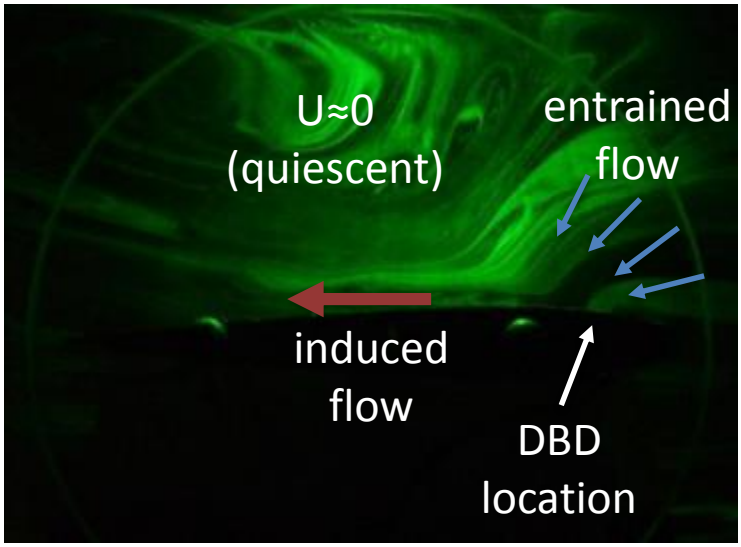

Figure 5: Visualization of momentum injection in still air

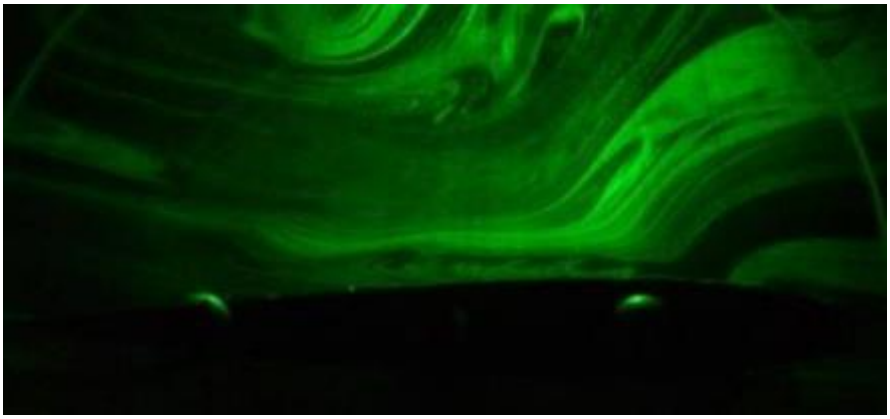

Figure 6: Close up of momentum injection in still air

Stream wise vortex generation works similarly to passive vortex generators with the DBD actuators placed so that their induced momentum is perpendicular to the free stream flow creating a vortex that will carry high momentum flow into the boundary layer near the airfoil surface.

In flow heating, the dielectric surface on the covered electrode significantly increases its temperature relative to the surrounding flow environment therefore altering the flow properties. Some of the effects this can lead to include shock suppression due to altered local speed of sound, and wave drag reduction. Taken from Leonov et al., Figure 7 shows an IR image of a dielectric barrier discharge after 30 seconds of operation [35].

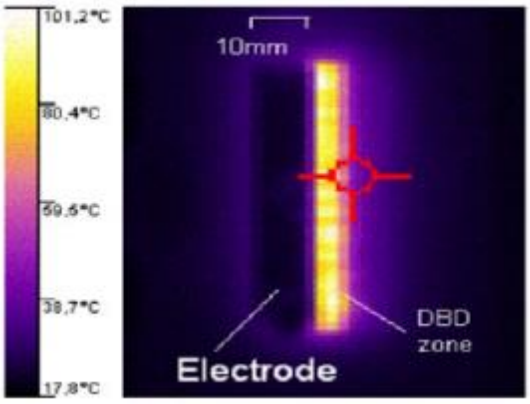

Figure 7: Dielectric surface heating [34]

In periodic forcing, which is the main emphasis of this study, the DBD is pulsed with an operating frequency, f , known as the Strouhal frequency so that the Strouhal number as shown in Eq. (6), is close to or somewhat above unity. In Eq. (6) *c* is the characteristic length; in this case equivalent to airfoil chord length and *U* is equivalent to the free stream velocity [23].

$$St = \frac{fc}{U} \qquad \textbf{Eq. (6)}$$

Some researchers have suggested the characteristic length be equivalent to the length from trailing edge to the point of separation, but in this study of leading edge separation that length is equivalent to the chord length. Bernard et al. studied the effects of the base AC signal frequency, pulsing frequency and duty cycle on the lift and drag coefficients of a NACA 0015 [11]. They found that the base AC frequency had two regimes where it affected the lift coefficient the greatest: one at 100 Hz (which for their setup was the Strouhal frequency) and then a second at any frequency over 1000 Hz. They found that around 50 Hz for the pulsing operation (which would be half the Strouhal frequency, or the subharmonic mode); they had the greatest improvement in both lift and drag coefficients. With the pulsing frequency equivalent to the Strouhal frequency, they still showed significant improvements over the baseline. For the effect of duty cycle, it was found that a duty cycle in the range of 6% to 50% gave the best results for lift coefficient while a duty cycle in the range of 40% to 50% gave the best improvement for drag coefficient [11]. This observed overlap of improved coefficients at 50% duty cycle is the basis for choosing a duty cycle of 50% for work carried out for this thesis. Jolibois et al. studied the effect of pulsed frequency and duty cycle on the attachment of a separated airflow over a NACA 0015 airfoil. They found that injected momentum for any pulsing frequency above 0.5 Hz was sufficient to reattach the flow; however, they were operating at 23 kV, which from Eq. (4) demonstrates that it would create a relatively large amount of induced thrust. Their velocity profiles also support that a frequency of 6 Hz pulsing (which would give a Strouhal number of one), and the plasma on in steady operation gave the best results for velocity profile

modification. They also observed that duty cycles at 50% in comparison to 10% and 25% gave the best results for velocity profile modification [8]. For He's dissertation he studied the effect of periodic forcing using a DBD for separation control over a NACA 0015 at Reynolds numbers of 180,000 and 257,000 and found that at the lower Reynolds number, a forcing near unity of the Strouhal number with a 10% duty cycle was sufficient to reattach the flow. He found that for the higher Reynolds number, a frequency slightly higher than the Strouhal frequency with a duty cycle also of 10% gave the best results for flow reattachment [36]. More recently, researchers that have been investigating various forms of steady and unsteady pulsing of the DBD actuator for flow control have been putting an experimental emphasis on nanosecond pulsing operation [12] [13] [37].

DBDs have many other aerodynamic applications other than just flow separation control. It can be useful by itself for aircraft performance, turbomachinery applications, and wind turbines, such as turbulent boundary layer control in both subsonic and supersonic regimes [38] [39] [40]. They have also been studied for noise control and mitigation for flow over bluff bodies and cylinders [41] [42]. Several researchers have also succeeded at installing DBDs and their required power supply equipment on to UAVs with varying results. In 2014, Wilm Friedrichs tested a UAV with DBDs located on part of the wingspan near the fuselage. He accomplished this by using a battery pack of 25 NiMH cells with nominal voltage of 30 V and capacity of 1900 mAh along with a GBS Elektronik Minipuls .1 high voltage frequency generator to power the DBDs. He noted that there was little to no effect the DBDs had on the performance of the UAV, however this could have been due to the DBD only being applied to limited portions of the span as seen in Figure 8 [43]. In 2011, Ved Chirayath used DBDs on a UAV to perform maneuvers without any moving control surfaces. He accomplished this using a 26.4 V lithium ion polymer battery with continuous nominal current of 40 A along with a custom built AC high voltage generator to power the DBDs. He reported being able to perform several roll maneuvers of the same characteristic with the same performance level as with moving traditional control surfaces [44].

Figure 8: UAV with DBD on partial span [43]

DBDs along with other forms of plasma actuation have many other potential applications aspects that could make them even more useful for aerospace applications. Among these include deicing and icing prevention as well as shock mitigation and control due to dielectric heating and local air heating caused by the actuators [45] [46]. Plasma interaction with electromagnetic waves allows that if certain plasma conditions (e.g., plasma density, plasma frequency) are met it can be used for radar cross section mitigation and electromagnetic pulse (EMP) protection which could be beneficial for military aircraft applications [47] [48]. It is however plausible that the electromagnetic radiation that is emitted from the actuators could cause interference with an aircraft's avionics and other electronics.

Experimental Work

The experimental work undertaken was the testing of the flow control authority of both a low power gapless DBD and a higher power, 1/8 in. gap DBD with plasma regions beginning at approximately 6% chord on a NACA 0012 airfoil, varying Reynolds number, plasma pulsing frequency, and angle of attack. The tested nominal Reynolds numbers: [25000, 50000, 75000, 10000, 125000], correspond to the Reynolds number regime of many small UAVs. For the low power testing various frequencies relating to the Reynolds numbers near unity of the Strouhal number as calculated by Eq. (6) as well as a clean case (no plasma) and a steady case (plasma on with no pulsing)were tested, as were a range of various nominal angles of attack (α): [13°, 14°, 15°, 16°]. For the high power, gapped DBD testing was carried out with only the clean and steady plasma cases and for angle of attack (α): [15°, 16°]. It was observed that the onset of stall would occur at the nominal angle of attack of 15°. The angle of attack would start at 13° for low power testing and 15° for high power testing in a test run and would be stepped up in the designated increments until reaching 16°, which has a percent blockage of 10.57% as derived in Appendix D. For each case of the low power testing, nine images where captured and then averaged together using Matlab to get a general idea of the condition of the flow (attached vs. separated). Compiled, or averaged, images were used to attempt to eliminate the possibility of misreading the flow behavior from an individual image. Figure 9 shows the experimental test matrix for angle of attack of 16°, this would be used for all angles of attack. White spaces indicate locations of data collection and gray spaces indicate that no data would be collected for the case.

AoA= 16°	clean	30Hz	40Hz	50Hz	70Hz	80Hz	90Hz	110Hz	120Hz	130Hz	150Hz	160HZ	170Hz	190Hz	200Hz	210Hz	Steady
Reynolds number																	
25000																	
50000																	
75000																	
100000																	
125000																	

Figure 9: Experimental test matrix for α = 16°

Experimental Setup

The experimental setup consists of the West Virginia University smoke wind tunnel, the model with the attached actuator, the power supply setup, and the data acquisition setup, which consists of the flow visualization equipment and a CNC rotary indexer, which allows for control of angle of attack. Figure 10 shows a CAD drawing depicting the layout of the test section with the laser system, camera, model, and CNC indexer, which are all parts of the data acquisition setup.

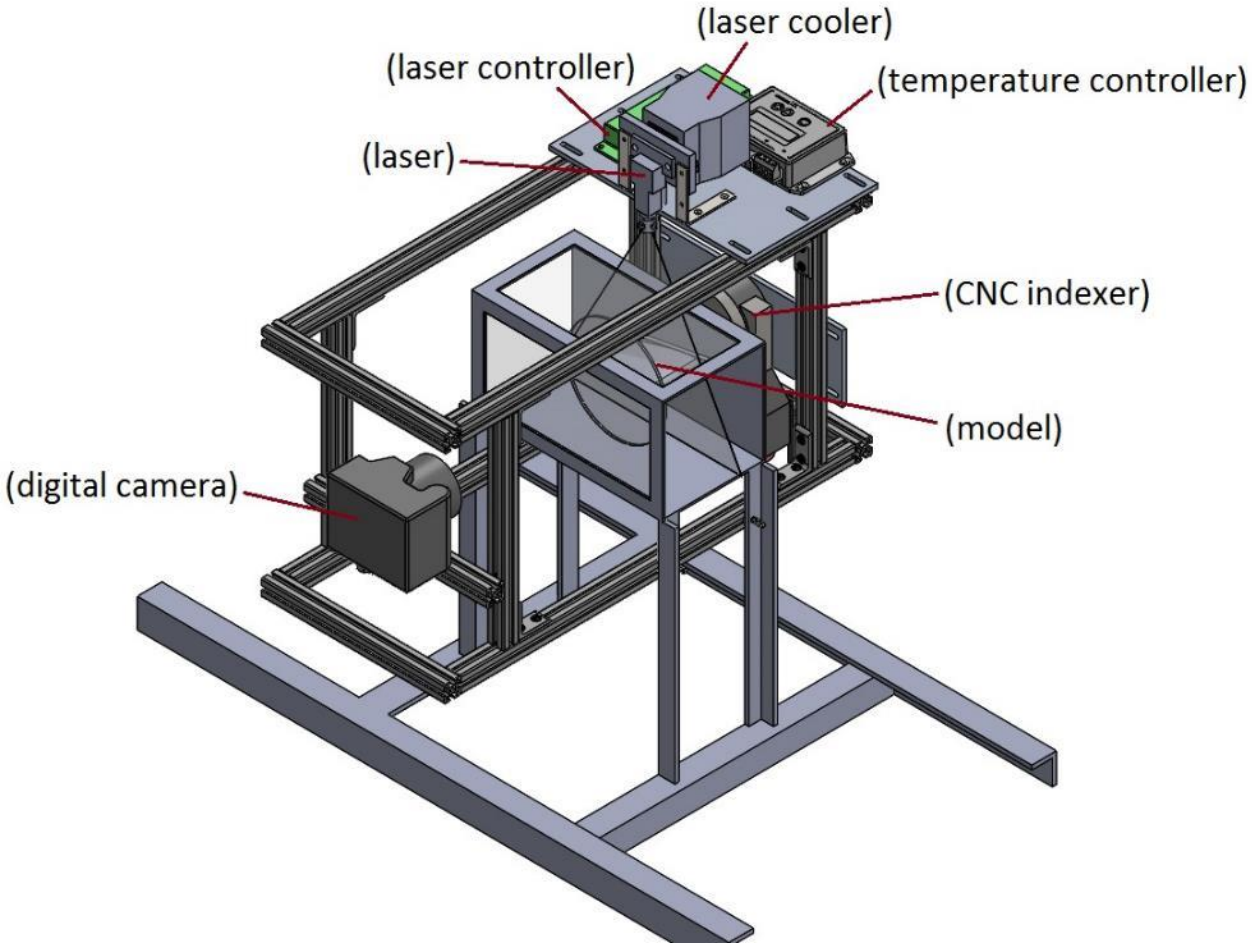

Figure 10: CAD of test section and equipment

Power Supply Setup

The waveform generator used for the experimental work was a BK Precision 4054 Function/Arbitrary Wave Generator. The signal was fed into a Crown XTi 4002 audio power amplifier (3200 W, bridged mono output), which was used to step up the current and driving voltage for the primary coil of the transformer. The custom high voltage step up transformer with a turn ratio of 1:140 was purchased from Corona Magnetics. Figure 11 gives a general illustration of the setup of the system used to power the actuator.

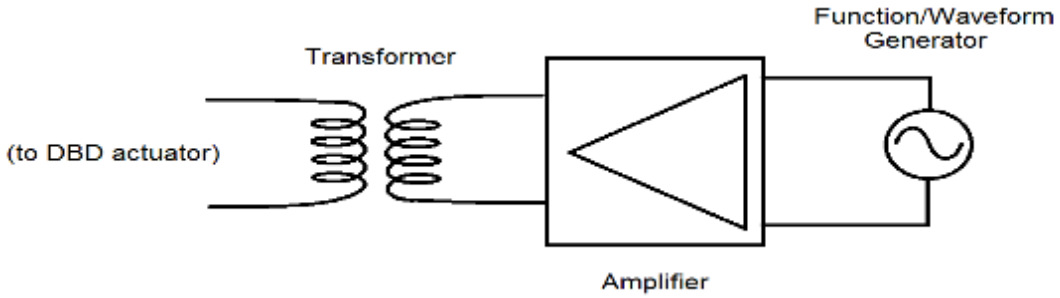

Figure 11: DBD actuator high voltage wave generation power supply schematic

The power drawn by the transformer-actuator RLC circuit is a function of the operation frequency. Consequently, the entire circuit must be energized near its combined resonance frequency to draw the least amount of power. Figure 12 shows the measured power for various frequencies (for the low power actuator) to illustrate the dependence of the power on the operating frequency. As can be seen from the figure, the circuit was in resonance at approximately 1400 Hz with a power draw of 2.90 ± 0.106 W while the DBD was operating steadily. This power draw is equivalent to approximately 57.2 W/m of actuator length. By comparison, the high power actuator with a 1/8 in. gap had a power draw of approximately 9.57 ± 0.174 W (≈188 W/m).

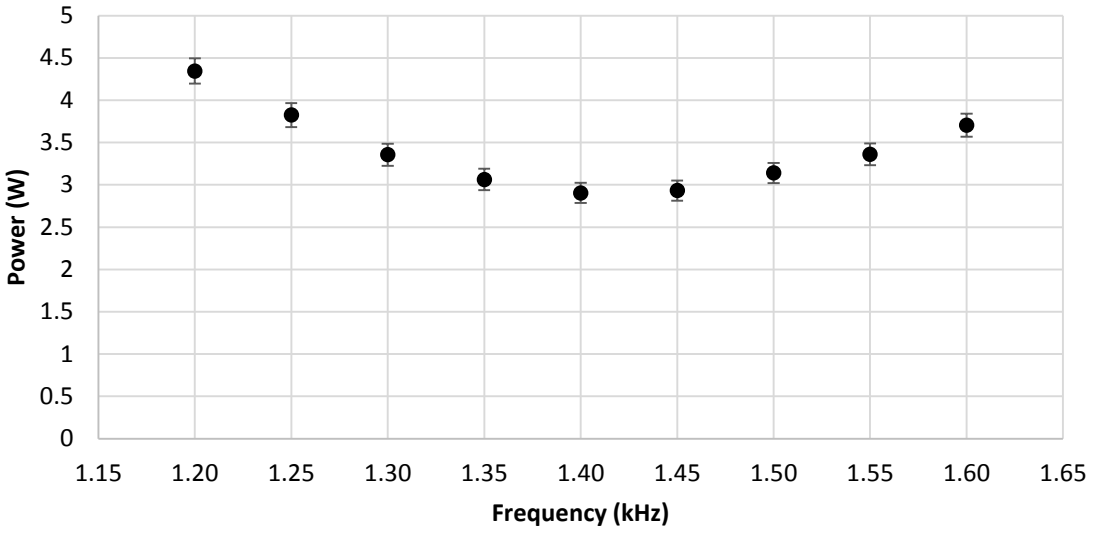

Figure 12: Gapless actuator resonance frequency testing

Once the base AC frequency was optimized for minimum power use at 1400 Hz for the low power actuator and 1700 Hz for the high power actuator, the pulsing frequencies were programmed into the waveform generator with each Reynolds number being tested for a combination of five frequencies for low power and two frequencies for high power testing. Tests for each Reynolds number selected were run for a clean case with no plasma (referred to as 0 Hz) and a steady plasma on case with the actuator running at the AC frequency of 1400 Hz (low power actuator) or 1700 Hz (high power actuator). The DBD drive signal was pulsed by operating the base AC signal at 50% duty cycle at varying pulse frequencies. For the low power testing three pulsing frequencies, with one below, one close to, and one above the Strouhal frequency, separated by 10 Hz each, were also investigated. For example, the Strouhal frequency for a Reynolds number of 25,000 is approximately 40 Hz so pulsing of the actuator took place at 30, 40, and 50 Hz as well as the clean (0 Hz) and steady (continuous operation at the base AC signal frequency) cases. At a Reynolds number of 125,000, the Strouhal frequency is approximately 200 Hz so pulsing occurred at 190, 200, and 210 Hz in addition to the clean and steady cases.

Actuator/Model Setup and Construction

The model is a rectangular, untwisted, NACA 0012-based wing with chord length of 3-15/16 in., a wingspan (width) of 3 in., and no dihedral or sweep characteristics with the actuator located so that the plasma region begins at approximately 6% chord due to construction restraints and to best match the location of dynamic roughness system. The electrodes are copper foil tape, and the dielectric material used is Kapton tape. The copper tape used for the electrodes has a width of ¼ in., consisting of 0.0014 in. thick foil with 0.0015 in. of acrylic nonconductive adhesive. The Kapton tape used for a dielectric has a width of ½ in. and consists of 0.001 in. thick film backed with 0.0015 in. of acrylic nonconductive adhesive. Figure 13 and Figure 14 show a generalized layout of model geometries.

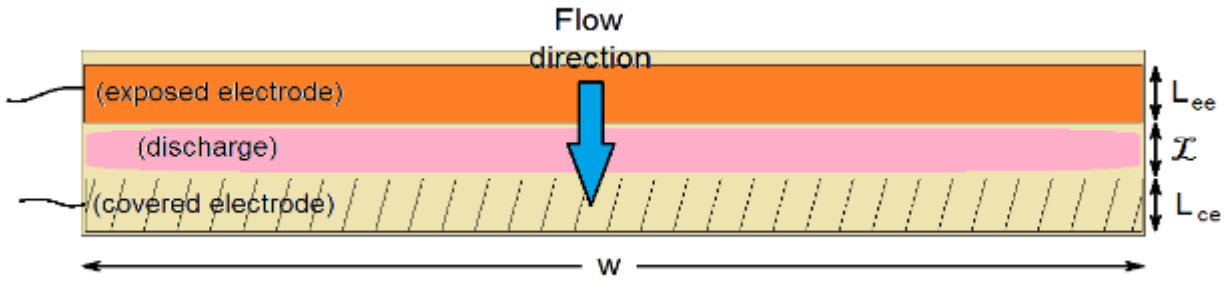

Figure 13: Actuator top view

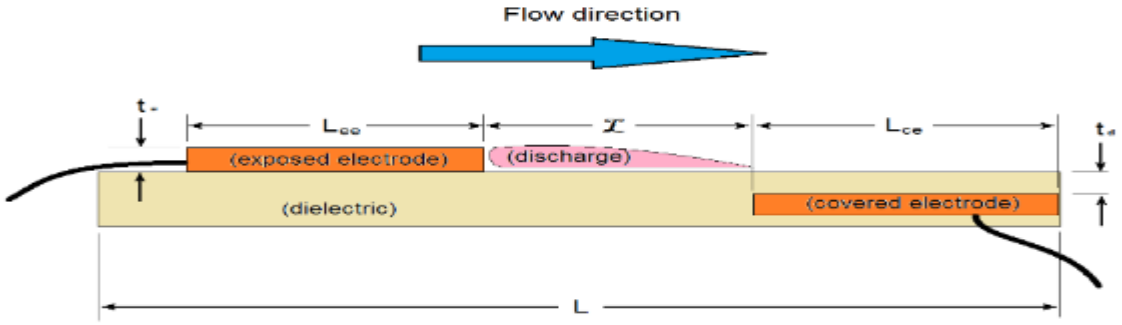

Figure 14: Actuator side view

Construction of the plasma actuator involved several steps:

Step 1) Measure and cut equal lengths of electrode foil with enough to cover the airfoil model span with extra for attachment of lead wires from the transformer.

Step 2) Round one of the edges of each electrode on the opposite end of the other as shown in Figure 15 to eliminate tip charge concentration.

Figure 15: Measured electrodes with a single rounded edge

Step 3) Place the covered electrode down on the wing making sure not to crease the foil, which would lead to areas of increased electric field strength allowing for localized arcing to occur at lower voltages.

Step 4) Cover the covered electrode with desired number of layers (3 layers where used for actuator construction of both actuators, for this testing) of Kapton tape, with the excess width being placed towards the direction of where the exposed electrode will be, as shown in Figure 16.

Figure 16: Covered electrode with excess dielectric towards the leading edge

Step 5) Finally, place the exposed electrode over top of the excess dielectric with desired gap width between the exposed and covered electrode as shown in Figure 17.

(Note: It is important to not have the edge of the dielectric exposed in the gap/plasma forming region, which will lead to arcing and subsequent combustion of the construction materials.)

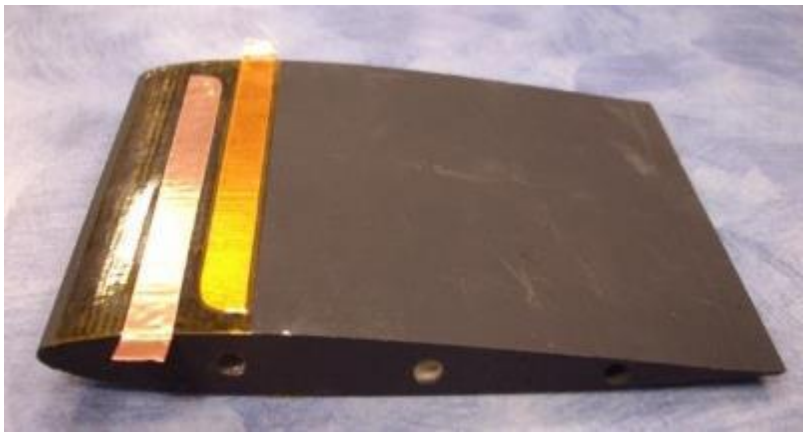

Figure 17: Fully constructed model (Example)

During construction, make sure to have the electrodes smooth and crease-free, as well as all air bubbles eliminated from under any layers of dielectric. Corke et al. re-analyzed experimental data from Forte et al. and have shown that a DBD device operates at its maximum efficiency when the gap distance between the inner sides of the electrodes ($\mathcal{I}$) is equivalent to the width of the covered electrode (L_{ce}) [5] [4]. However, it is difficult to maintain diffuse plasma, which is preferred for longevity reasons, in atmospheric pressure air with a gap larger than a millimeter or two. For the reason of construction limitations imposed by the placement of the actuator and the size of the electrodes as well as the desire to operate at the lowest possible voltage to increase actuator lifetime, a DBD actuator with negligible gap (nominally "gapless") design was used in the majority of the testing. In comparison, the high power actuator was only tested for limited cases due to the observed short lifetime of gapped high-voltage actuators. The finished models that were used in testing placed the beginning of the plasma region located approximately at 6% chord with a visual plasma extent of approximately 3/16 in. for the gapless low power actuator and

approximately 5/16 in. for the gapped high power actuator. Rinoie and Takemura observed that for the NACA 0012 that separation occurred near the leading edge at about 1% chord length and that the bubble that exists for the tested conditions would reattach around 10% chord [49]. This would place the active plasma region within the separation bubble region.

Data Acquisition

Data acquisition took placing using a flow visualization technique and an image-capturing device used to take nine images at each case that would later be averaged into one image.

Visualization Technique

The flow visualization effort primarily required three components: seed particles that would follow the flow, an illumination system to illuminate the seed particles, and an image-capturing device.

Seeding:

The flow was seeded with ~1-10 micron Di-Ethyl-Hexyl-Sebacate (DEHS) droplets. Olive oil was atomized using a pneumatic seeding instrument manufactured by LaVision, Inc.

Illumination:

The flow seed particles were illuminated by a NECSEL Green EVO Laser run at 15 amps with temperature controlled at 75°C. The coherent light emitting portion of the laser consists of several laser diodes, so a fixture with a glass rod insert was constructed to turn the several small point lights into a planar light sheet. Figure 18 shows the laser with the planar fixture and Figure 19 shows the laser with controller and cooling system.

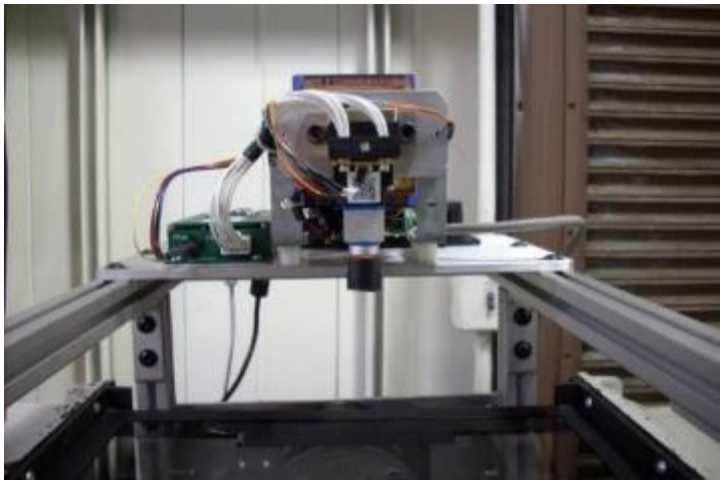

Figure 18: Laser

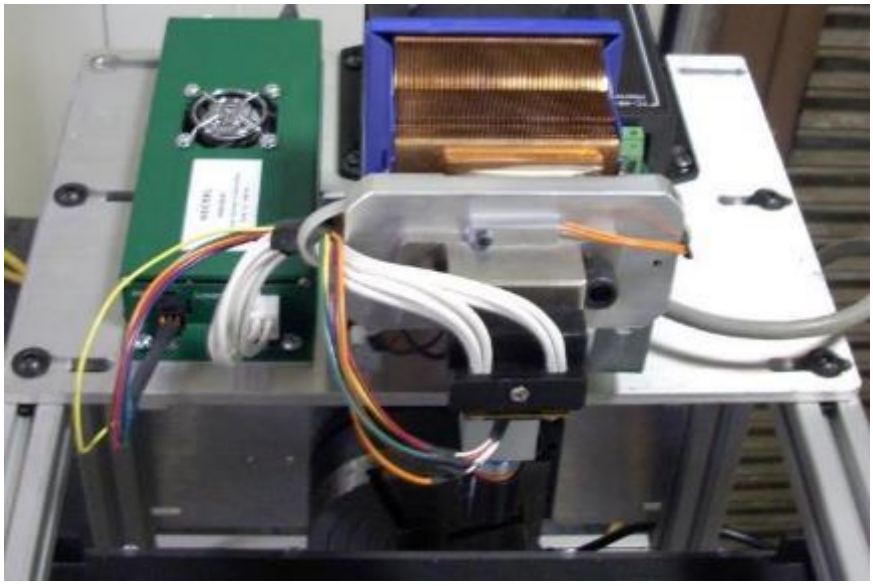

Figure 19: Laser controller and cooling system setup

Image Capturing Device:

The camera used for image capturing was a Nikon D5300 with a Nikon AI-S 55 mm lens (standard Nikon mount). Images were captured and saved to their respective folders using a software package called DigiCam Control. The camera settings were set at shutter speed of 1/2000 seconds, aperture f-stop of *f*/1.2, and a sensitivity ISO of 3200. At the highest Reynolds number of 125,000, the flow speed is about 20 m/s. This gives a flow through time over the wing of about .005s. At this speed and with the shutter speed of (1/2000)s, a single particle could travel about 10% of chord length during a single frame capture. Figure 20 shows the camera mounted and its position relative to the mounted model wing.

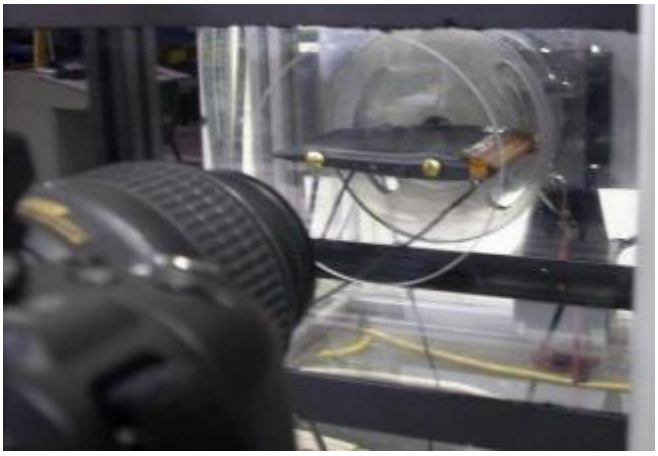

Figure 20: Camera and wing model setup

Experimental Testing

The experiments were conducted in the low-turbulence (max turbulence intensity, TI, of 1.80% with mean TI of 0.81%) flow visualization Eiffel-type wind tunnel, which can be seen in Figure 21.

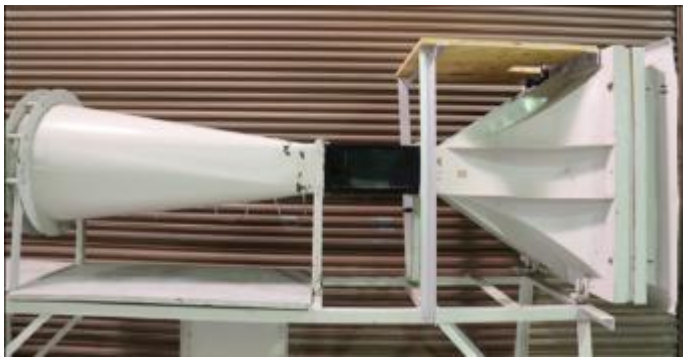

Figure 21: Flow visualization wind tunnel

The test section of the wind tunnel has a 6 in. x 6 in. cross section and a test section length of 12 in. with transparent walls on three sides. Installed in front of the test section are a series of screens with decreasing mesh size followed by a contraction section to help provide uniform flow (with an average speed of 67.06 ft/s with a max variation of 3.68%). The raw data for the velocity profile and TI can be seen in Figure 87, found in Appendix A. The wind tunnel test section with all the testing components components assembled can be seen in Figure 22.

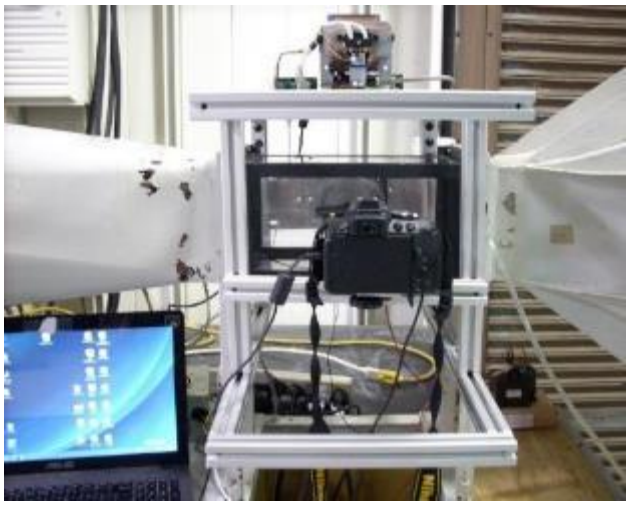

Figure 22: Up close testing setup

During low power testing, nine images were collected with a frame rate of 3 fps at each case starting at an angle of attack of 13° through the predefined positions to 16° angle of attack [50]. During high power testing five images were collected at each case. The images where simultaneously saved in files based on their Reynolds number and plasma operating frequency.

Experimental Procedure

The following procedure was used for all experiments:

1. Starting at angle of attack of 13° for low power gapless actuator testing or 15° for the high power gapped actuator testing, Reynolds number of 25,000 and clean (no plasma) a series of nine images (low power) or five (high power) is collected. This is considered one case.
2. Next the CNC indexer is used to step to the next angle of attack and given approximately 5 seconds for the flow to reach steady state. Then nine more (or five more) images are collected. This is considered another, individual case.
3. The angle of attack is then adjusted to each angle of attack with nine (or five) images captured at each.
4. Next the plasma is turned on to its lowest pulsing frequency at the starting angle of attack either 13° or 15° and then the model is stepped through each angle of attack with appropriate number of images being captured at each.
5. The plasma is then set to its next frequency and then run through the sweep again.
6. Once every sweep of every plasma frequency is completed, including clean and steady cases, the Reynolds number is adjusted to the next value and the entire process is repeated again.
7. After testing, for the low power testing the images where compiled using a Matlab code made specifically for this purpose. Figure 23 shows a flow chart of the operation of the Matlab code, while a listing of the code can be found in the Appendix B.

8. Once compiled, the images where then cropped using Matlab (code can be found in the Appendix B), and placed in groups to allow for comparison across all plasma frequencies.

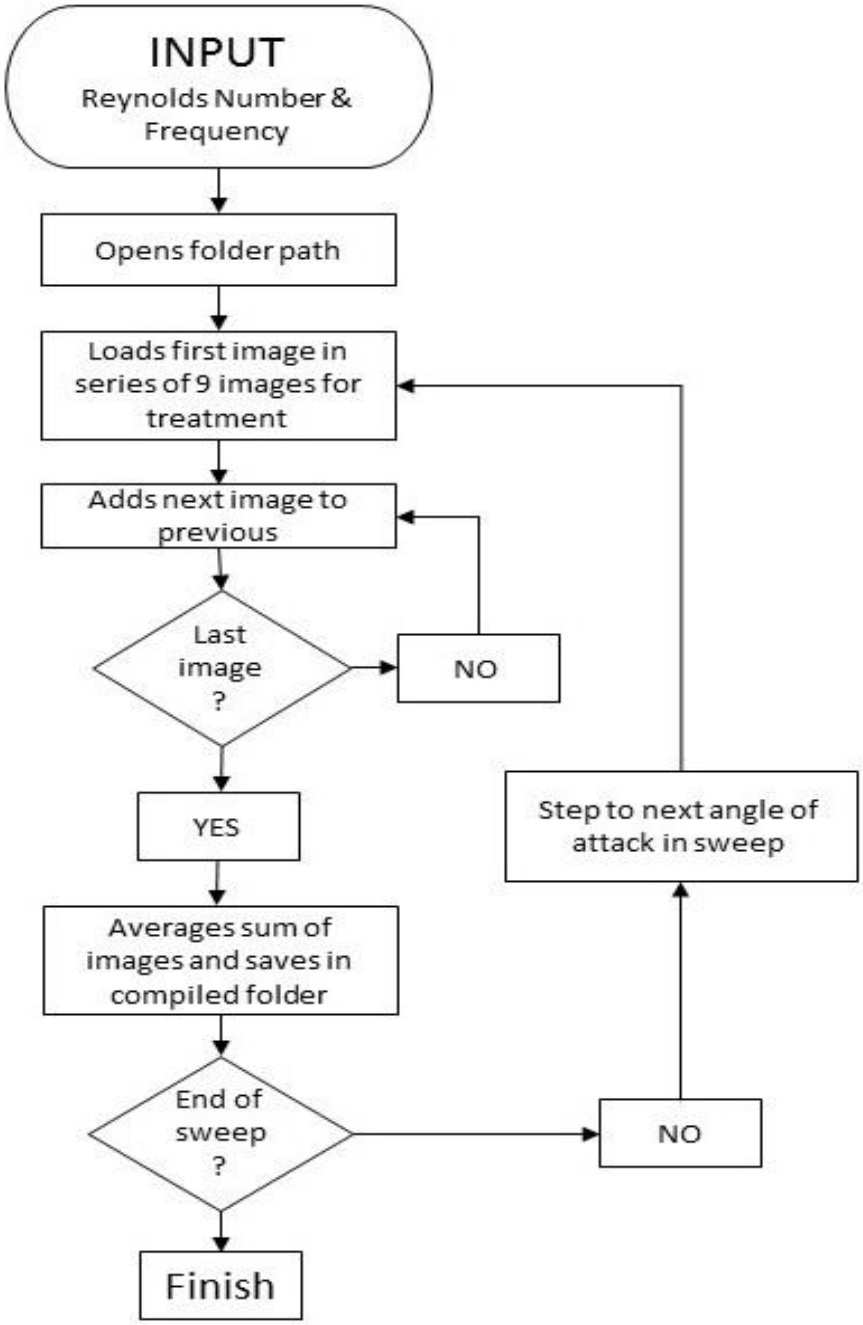

Figure 23: Matlab image processing flow chart

Before testing was conducted, a collection of 43 images was taken to see if there was a significant difference between compiling a few images with a significantly larger number of images. Figure 24 and Figure 25 depict the results of compiling 9 and 43 images, respectively. As can be seen from the images there is no significant difference.

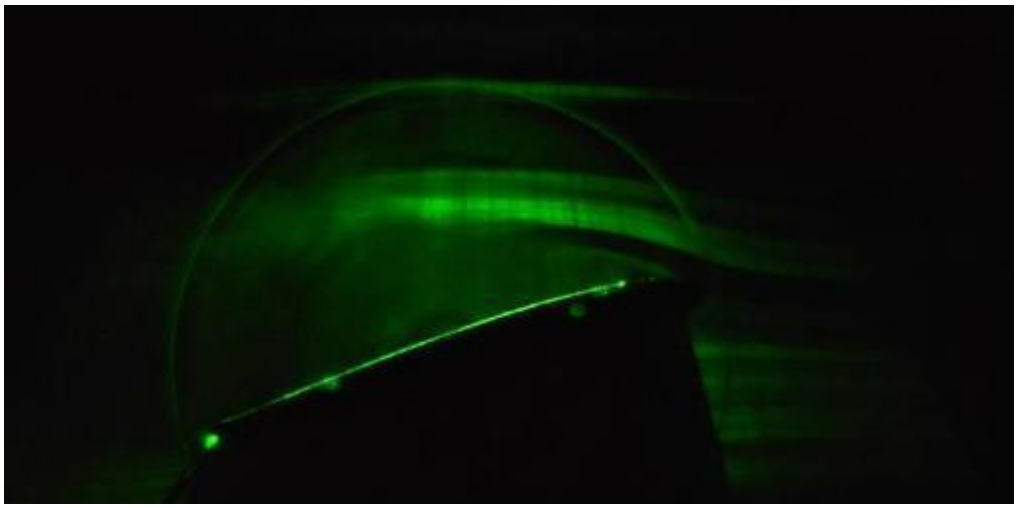

Figure 24: 9 Compiled images at Re = 75,000 α = 16° f = 0 Hz

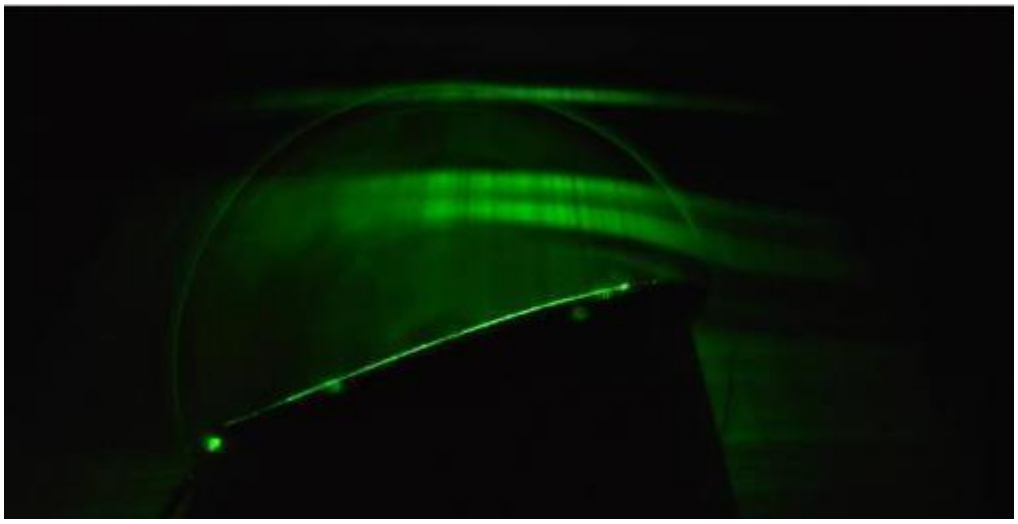

Figure 25: 43 Compiled images at Re = 75,000 α = 16° f = 0 Hz

Results

The results section will be broken up into three main sections. The first section will be results and discussion for the low power DBD testing. The second section will be the results and discussion of the high power DBD testing. The third section is a comparison of some of the results from the low power DBD at low Reynolds number with similar DR results. In the images in the results section, captured during testing there is a perceived discrepancy in the location of where the location of the leading edge of the model is located. The laser light sheet intersects the model at approximately half span, which is approximately 1.5 in. behind the end of the wing model in the images. This difference in the distance from the camera leads to the leading edge appearing to be in front of where it is located at the laser plane. This perceived location variation is known as parallax. Figure 26 shows the perceived discrepancy and the actual location of the leading edge at the laser plane in the images.

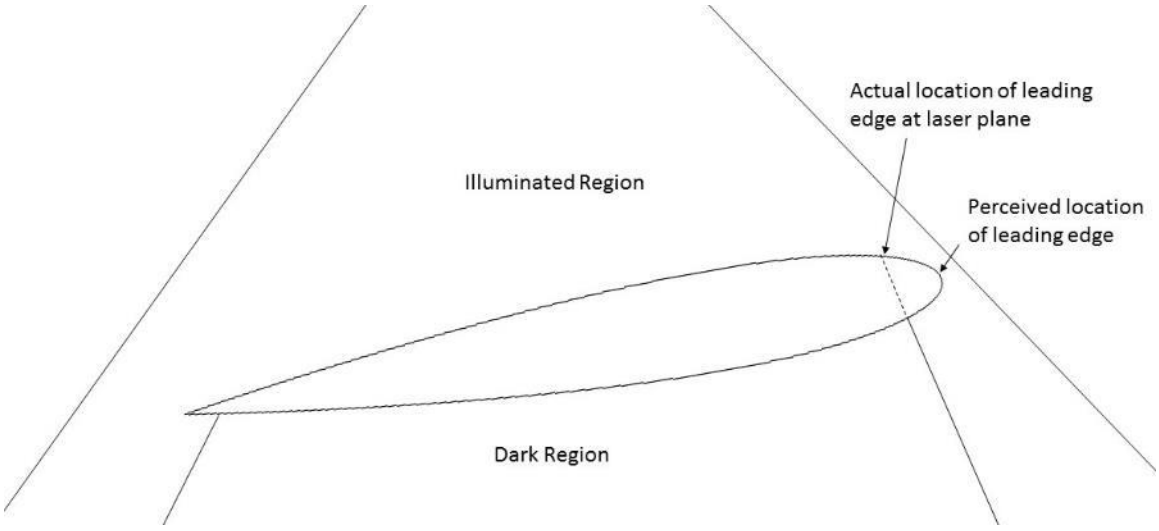

Figure 26: Picture layout and leading edge location

Low Power DBD results

In the DBD results section, each image will consist of a collage of five images displayed as depicted in Figure 27, with each collage being at one nominal angle of attack and at one nominal Reynolds number with all five frequencies. The discussion for each Reynolds number will have a description of any noticeable effects followed by supporting image collages and individual representative images if necessary. All results are discussed as nominal Reynolds numbers. The uncertainty in the Reynolds number can be found in Appendix E.

The low power testing was carried out with gapless actuator powered at 2.90 ± 0.106 W (≈57 W/m) with a voltage potential of approximately 7.7 kV between the electrodes.

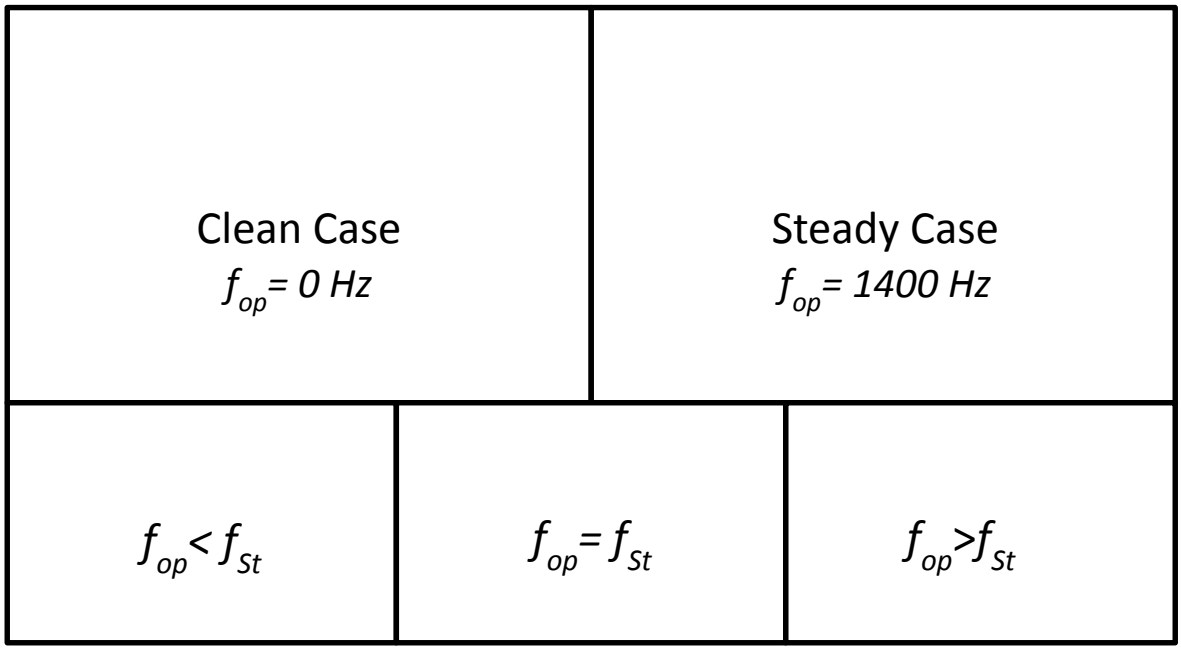

Figure 27: Compiled image layout

Reynolds Number 25,000

For angle of attack of 13°, there is no discernable difference between any of the cases in the compiled images as seen in Figure 28. However, by examining individual images for the clean case, and even the Strouhal frequency case, there is the existence of the laminar separation bubble as seen in Figure 29 and Figure 30. In the steady-on case, the laminar separation bubble appears to no longer exist, as seen in Figure 31. For angle of attack of 14°, it clearly can be seen from the compiled images in Figure 32 that there is some control effect taking place when comparing the clean case to the steady on case. The clean case exhibits separation near the leading edge followed by turbulent structures downstream where the steady case appears to be attached over the entire upper surface. This can more clearly be seen by comparing individual images of both cases in Figure 33 and Figure 34. Figure 33 shows the separation occurring on the clean case and Figure 34 shows the flow behavior in the steady on case. For angle of attack of 15°, the compiled images in Figure 35 appear to show a slight difference between the clean and steady on cases. Comparing individual images of the clean case in Figure 36 with the steady on case in Figure 37 it appears the DBD is having some controlling effect. For angle of attack of 16°, the compiled images in Figure 38 shows no discernable difference. Investigating individual images, it appears that only the steady on case has any influence over the flow. For the clean case, the flow is always separated as shown in Figure 39. For the steady on case the flow appears to oscillate between there being no observable control effect as shown in Figure 40 and a noticeable control effect as shown in Figure 41.

Reynolds Number 25,000

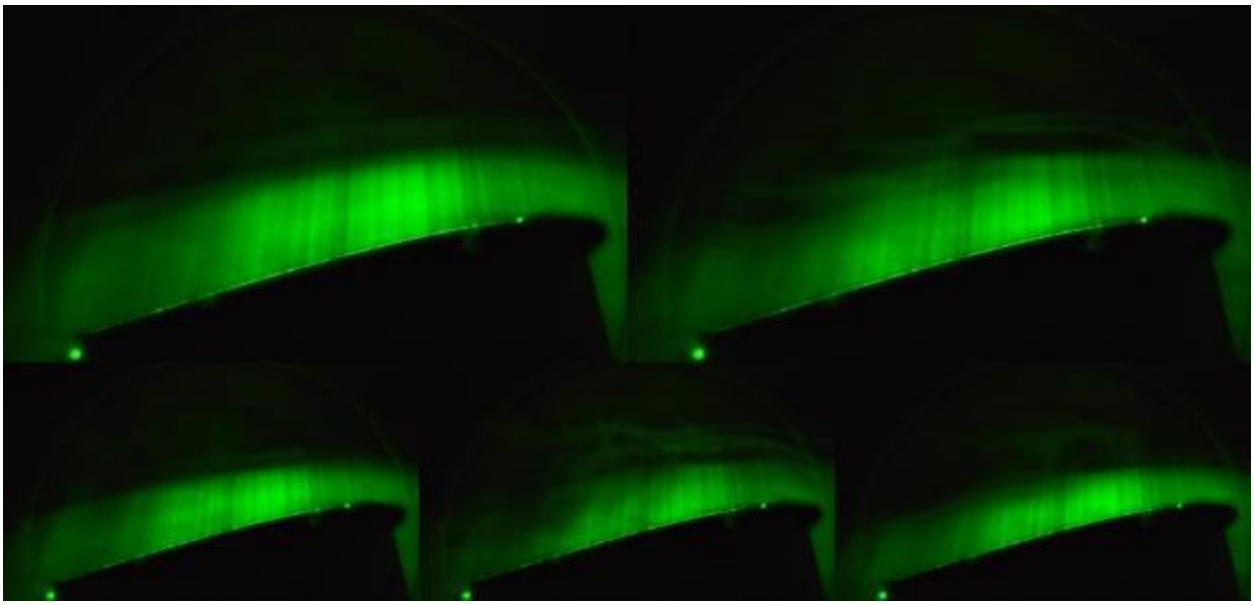

Figure 28: Re = 25,000 α = 13° compiled image comparison

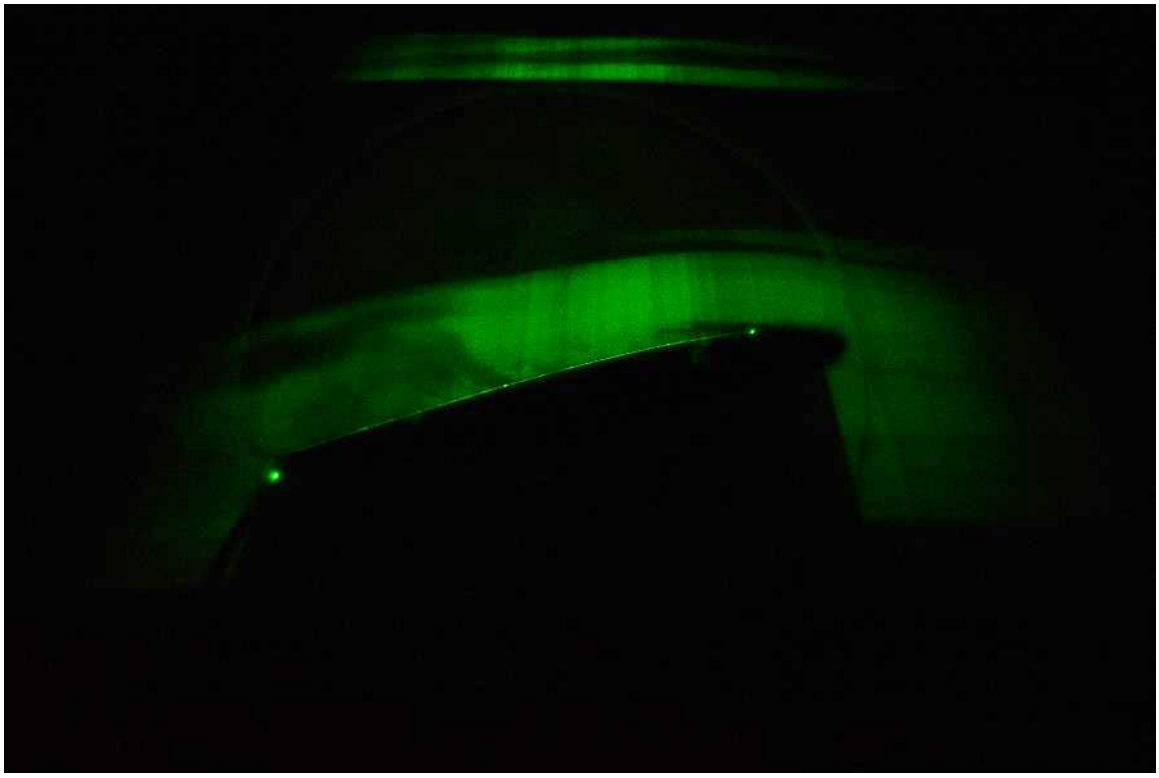

Figure 29: Re = 25,000 α = 13° f = 0 Hz (appears separated with laminar separation bubble near leading edge)

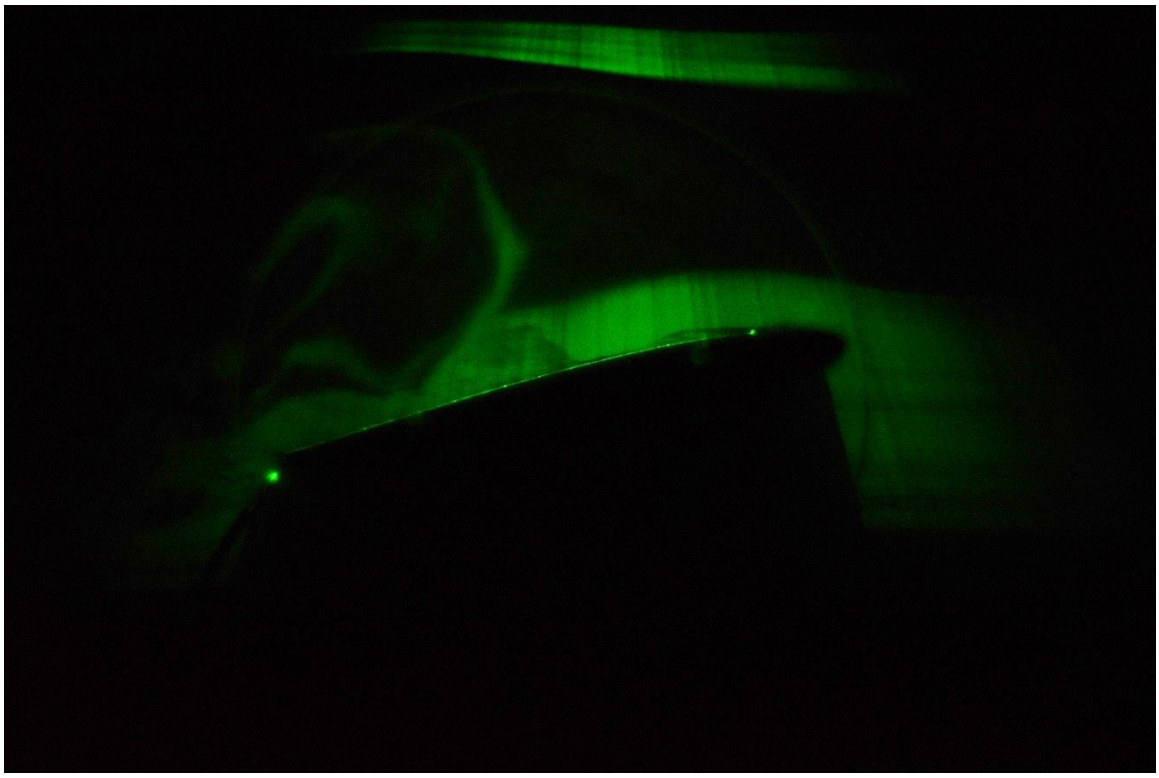

Figure 30: Re = 25,000 α = 13° f = 40 Hz (appears to still exhibit laminar separation bubble)

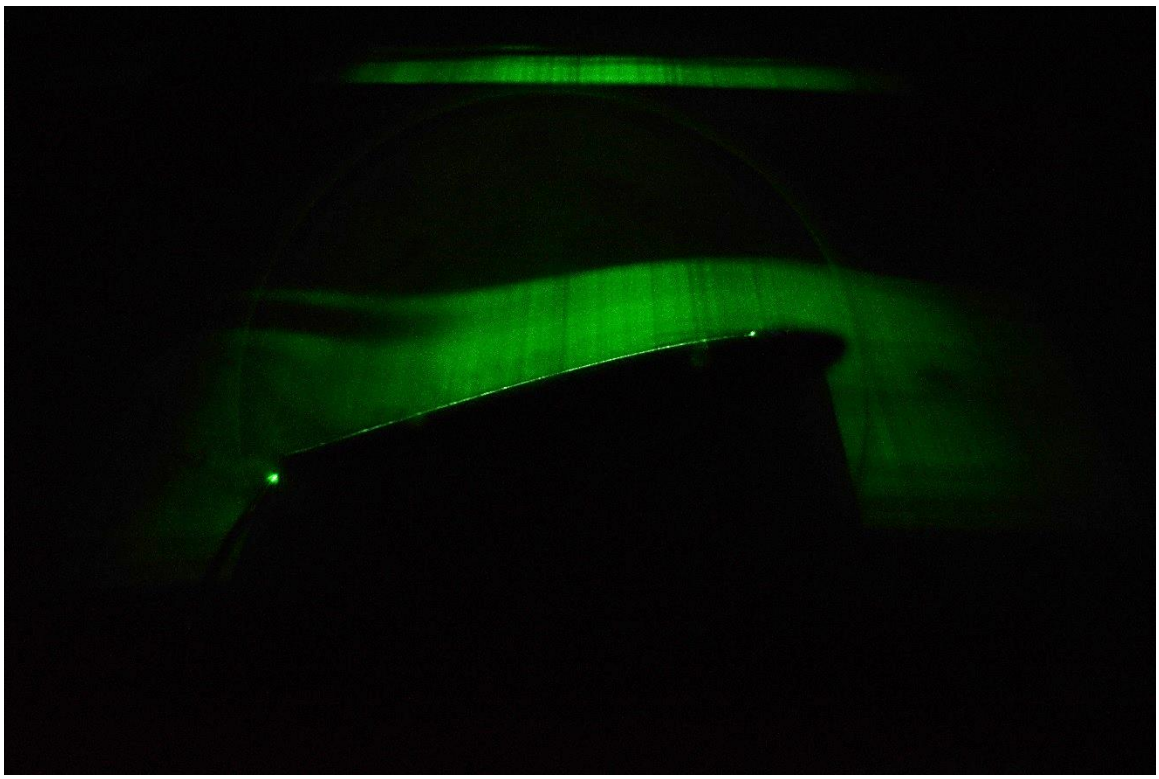

Figure 31: Re = 25,000 α = 13° f = 1400 Hz (appears laminar separation bubble has been eliminated)

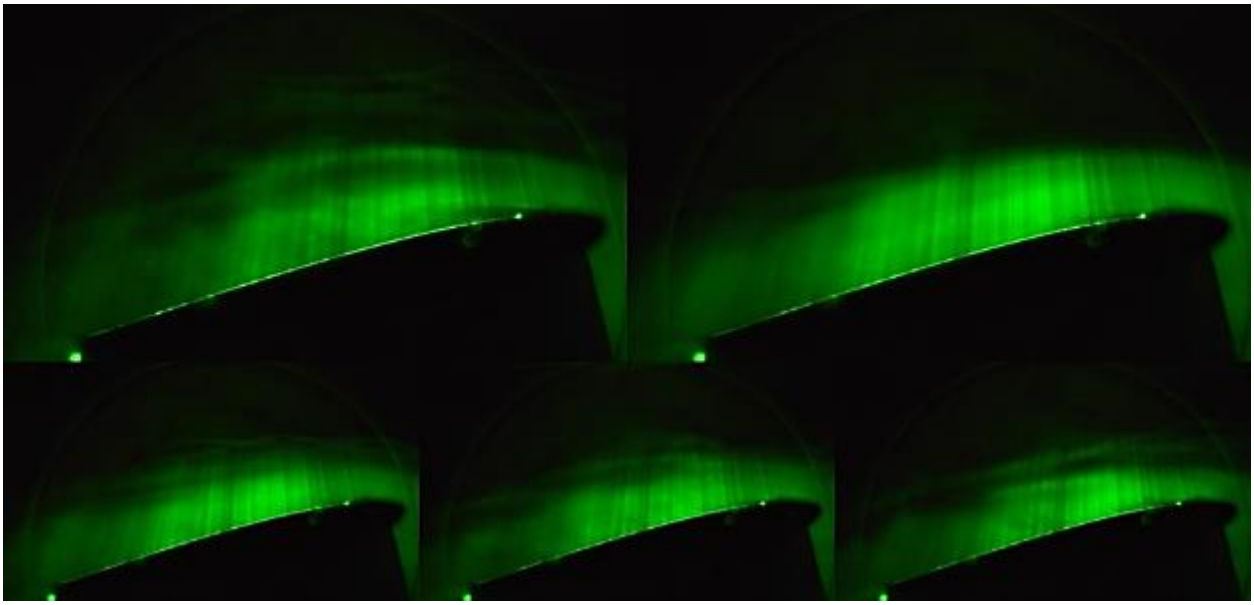

Figure 32: Re = 25,000 α = 14° compiled image comparison

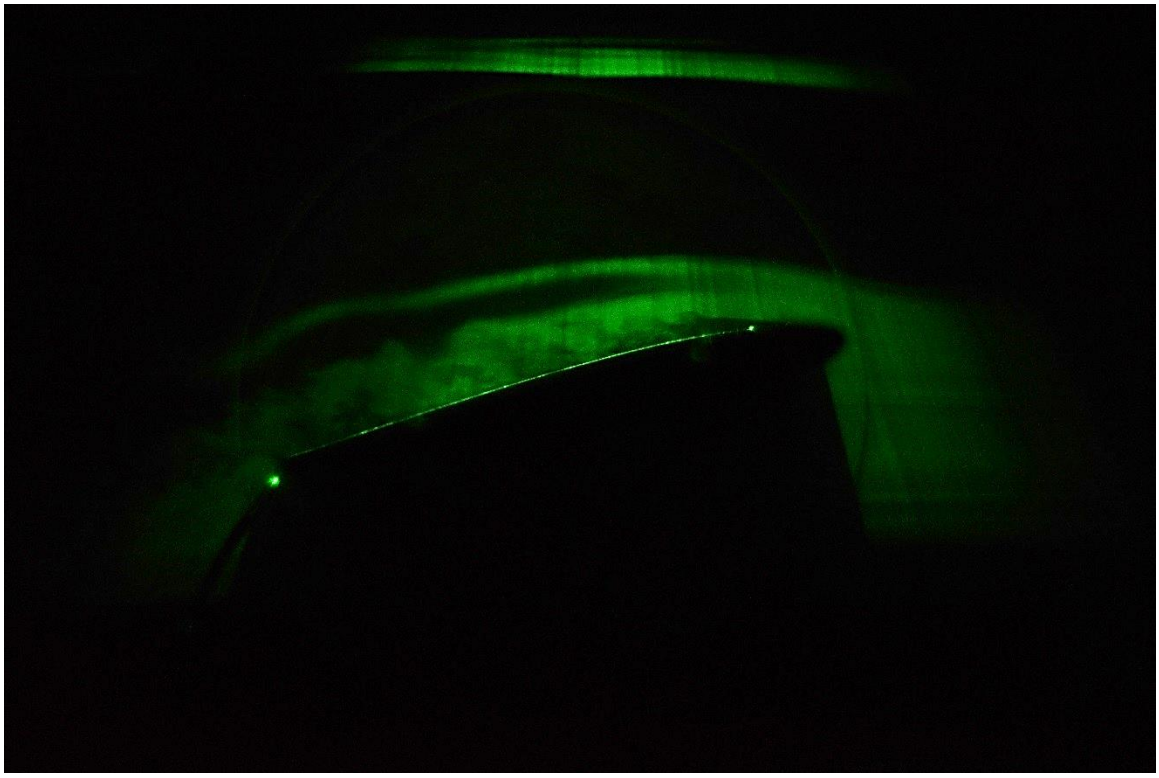

Figure 33: Re = 25,000 α = 14° f = 0 Hz (appears separated with turbulence)

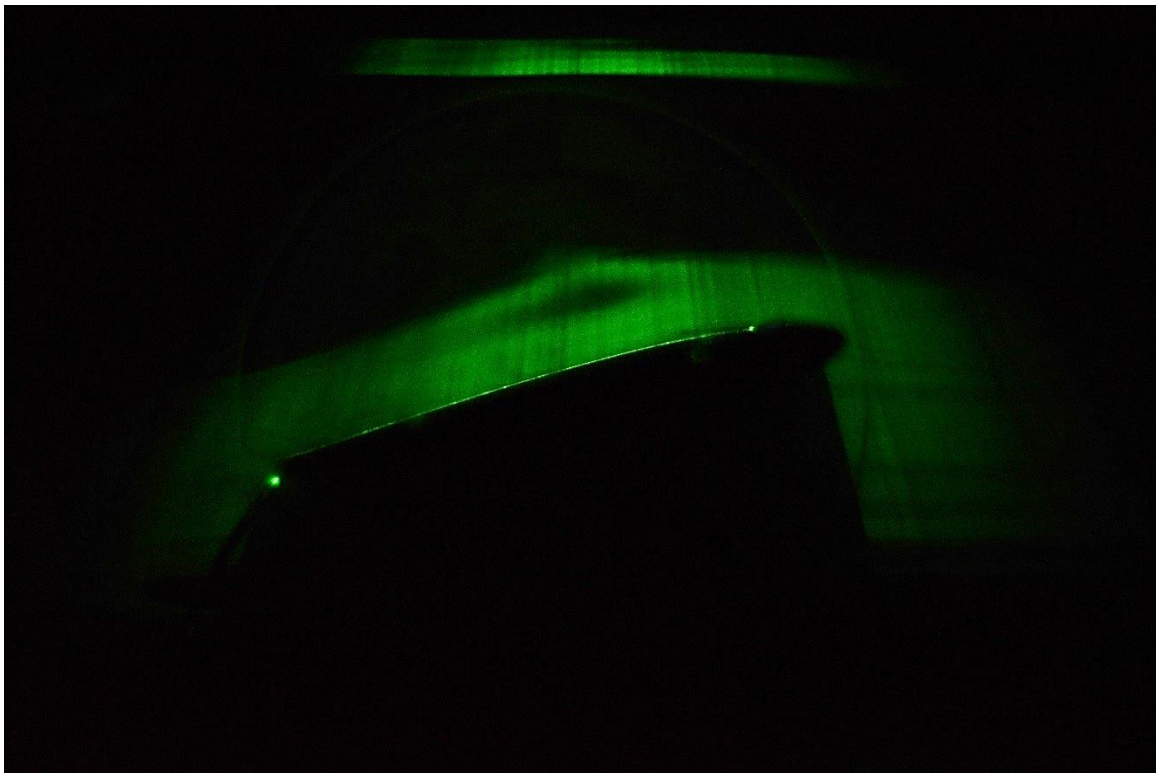

Figure 34: Re = 25,000 α = 14° f = 1400 Hz (appears attached over upper surface)

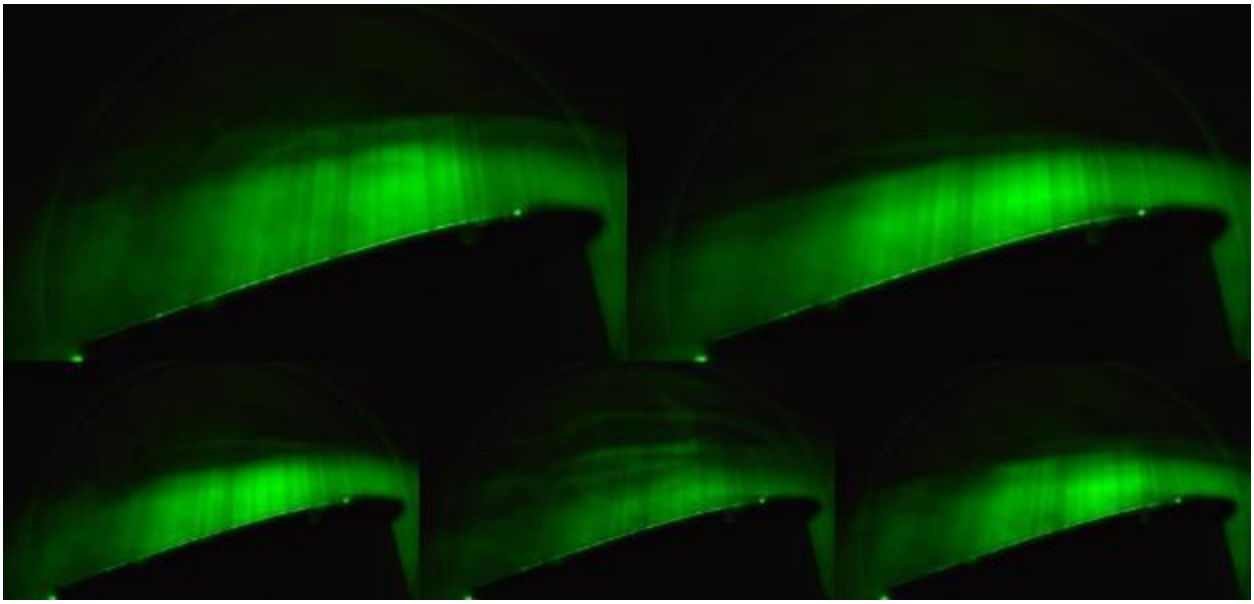

Figure 35: Re = 25,000 α = 15° compiled image comparison

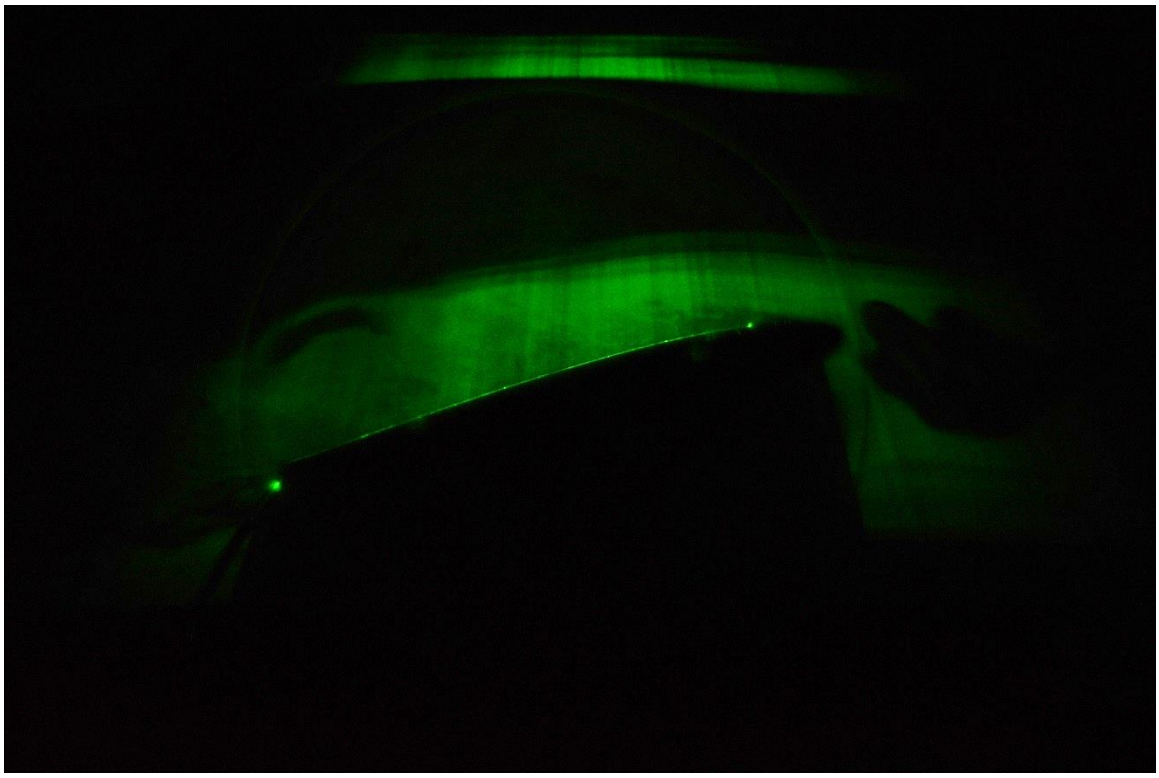

Figure 36: Re = 25,000 α = 15° f = 0 Hz

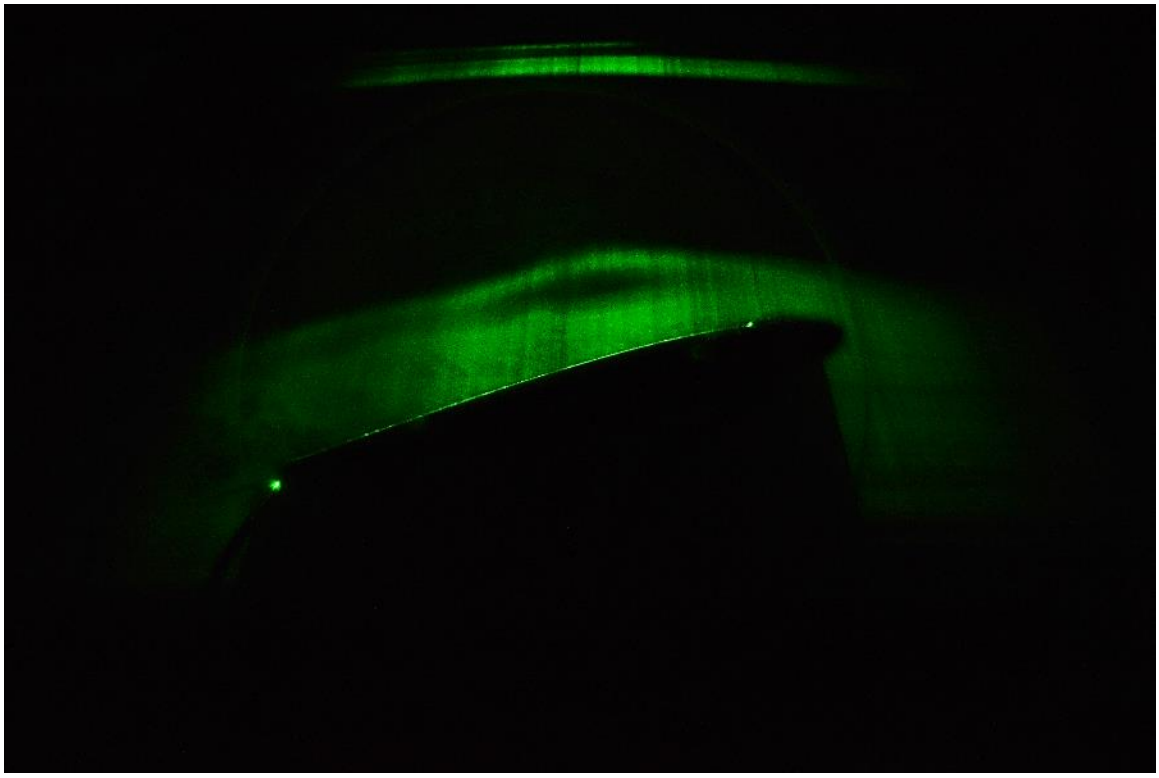

Figure 37: Re = 25,000 α = 15° f = 1400 Hz

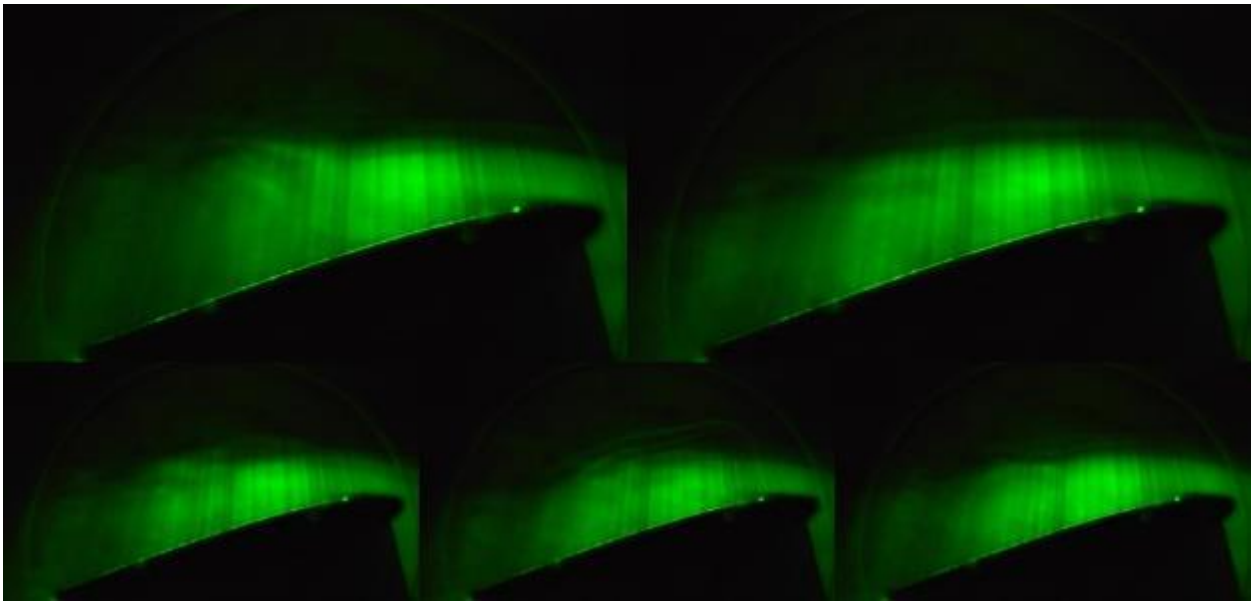

Figure 38: Re = 25,000 α =16° compiled image comparison

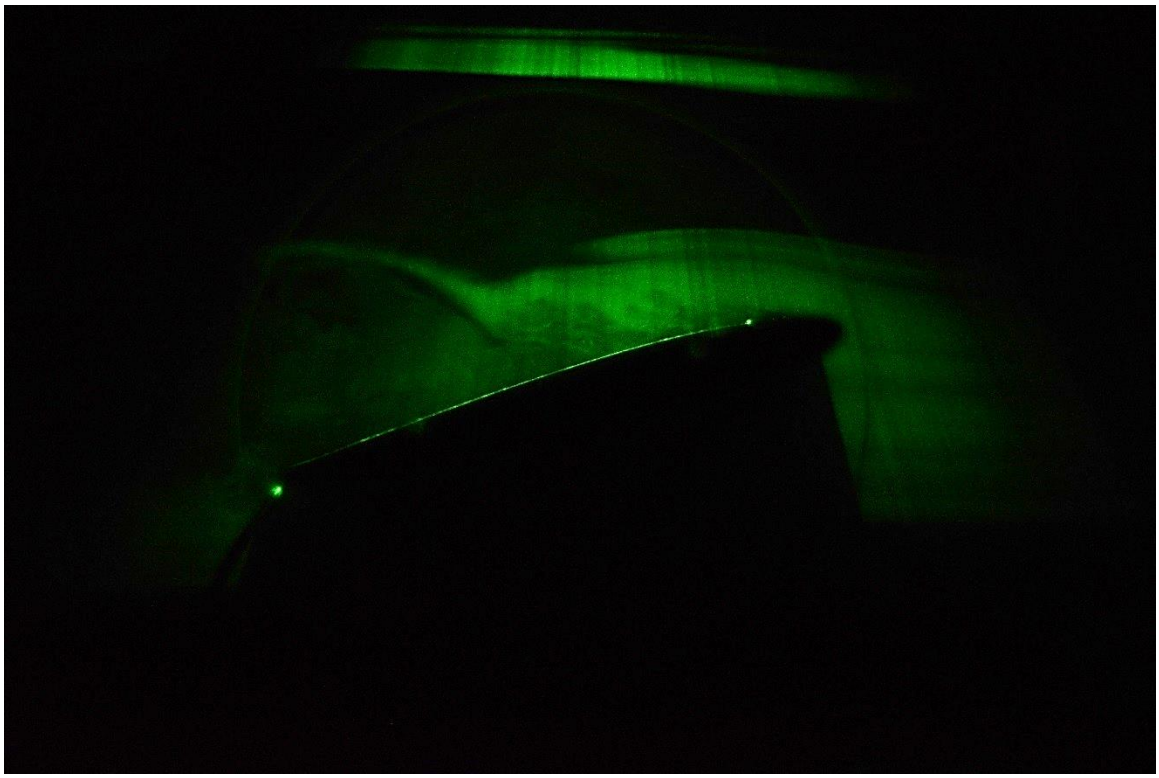

Figure 39: Re = 25,000 α = 16° f = 0 Hz (separated)

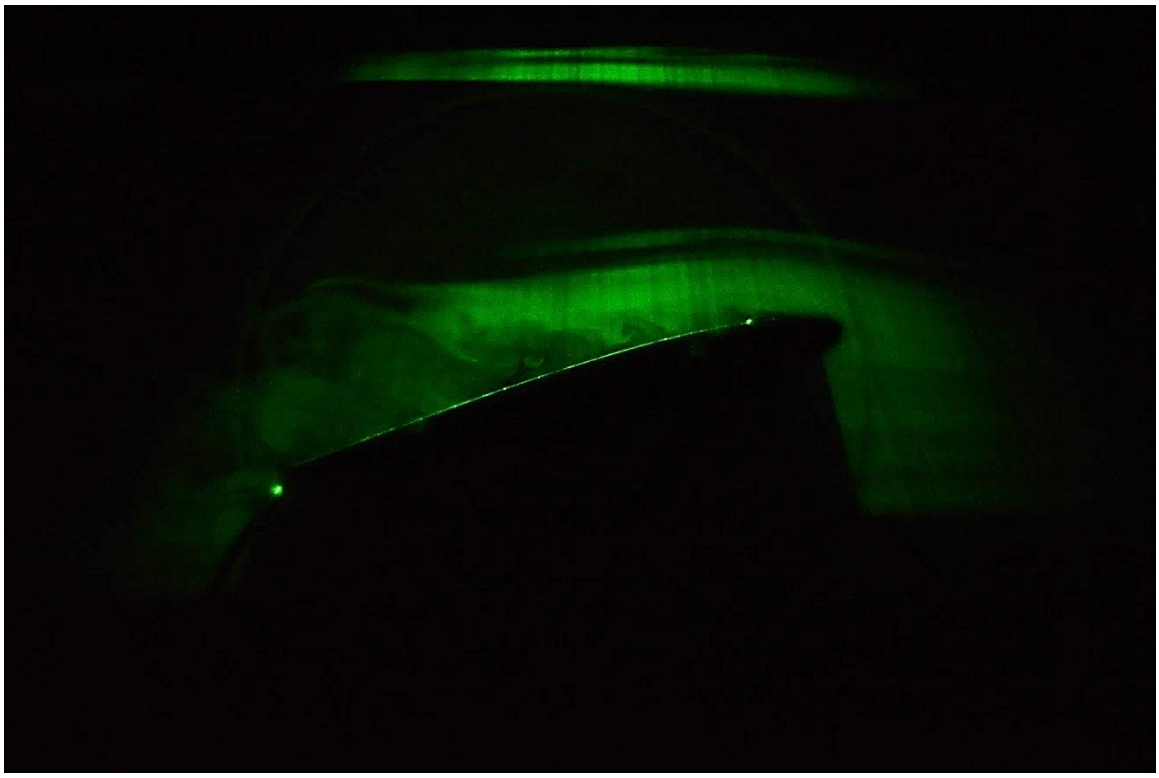

Figure 40: Re = 25,000 α = 16° f = 1400 Hz (oscillatory: no control effect)

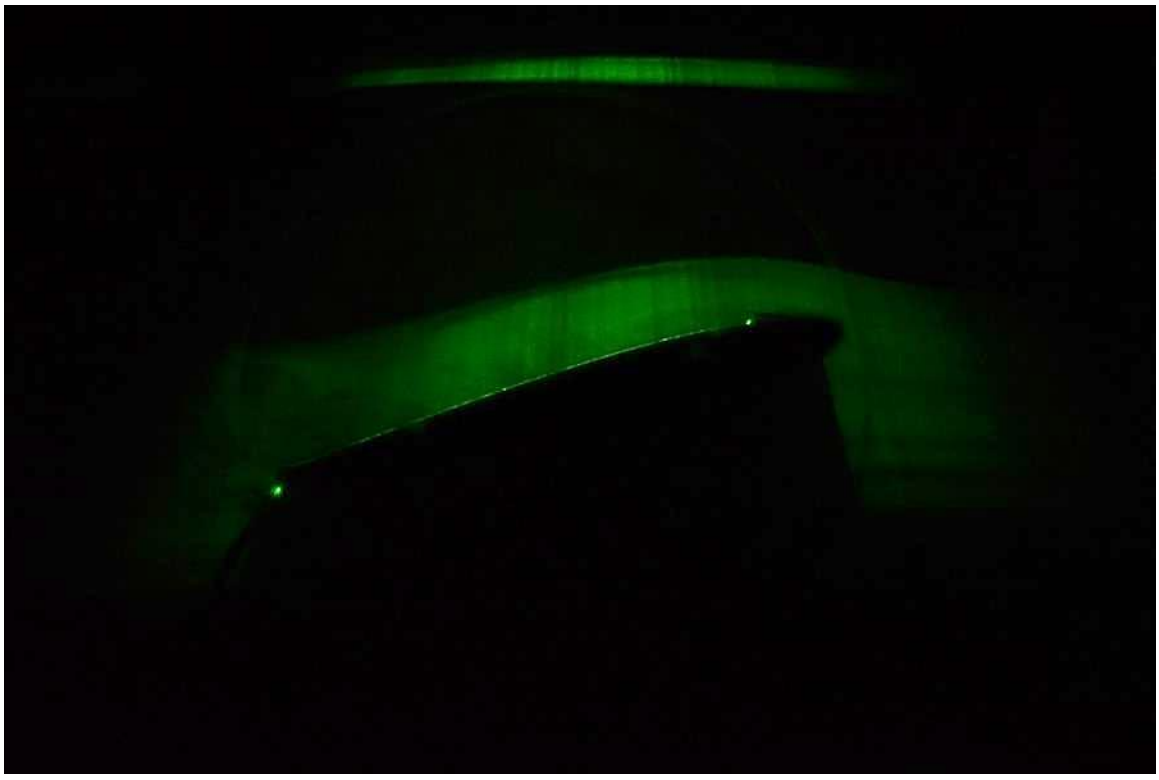

Figure 41: Re = 25,000 α = 16° f = 1400 Hz (oscillatory: control effect)

Reynolds Number 50,000

For Reynolds number of 50,000 there appears to be nothing of interest at angle of attack of 13°. Unlike Reynolds number of 25,000 it appears that, there is not even a laminar separation bubble at this angle of attack. Similar to Reynolds number of 25,000, angle of attack of 14° appears to have a significant difference between the clean and steady cases as seen in the compiled images in Figure 43. This can more clearly be seen by comparing individual images of the clean case Figure 44, with the steady on case in Figure 45. The Strouhal pulsing case also appears to have a controlling effect over the flow at this angle of attack as shown in Figure 46. For angle of attack of 15°, the compiled images show no discernable difference between the cases as shown in Figure 47. However, by inspecting individual images of the clean case the flow appears separated in every case as seen in Figure 48, whereas the Strouhal frequency pulsing case shows some effective control as shown in Figure 49. The Steady on case exhibits oscillatory behavior between a controlling effect as seen in Figure 50 and apparently no controlling effect as seen in Figure 51. This result tends to indicate that for this specific Reynolds number and angle of attack combination the Strouhal pulsing frequency offers the best flow control. For angle of attack of 16°, the compiled images show no discernable difference between the cases as shown in Figure 52. Inspecting individual images, it appears that the steady on case has a controlling effect on the flow. Figure 53, clearly shows the flow is separated for the clean case where as Figure 54 and Figure 55 show an oscillatory behavior of the flow between there being a controlling effect and no controlling effect. The other pulsing frequencies exhibit a similar oscillatory behavior as can be seen for the Strouhal pulsing case in Figure 56 and Figure 57.

Reynolds Number 50,000

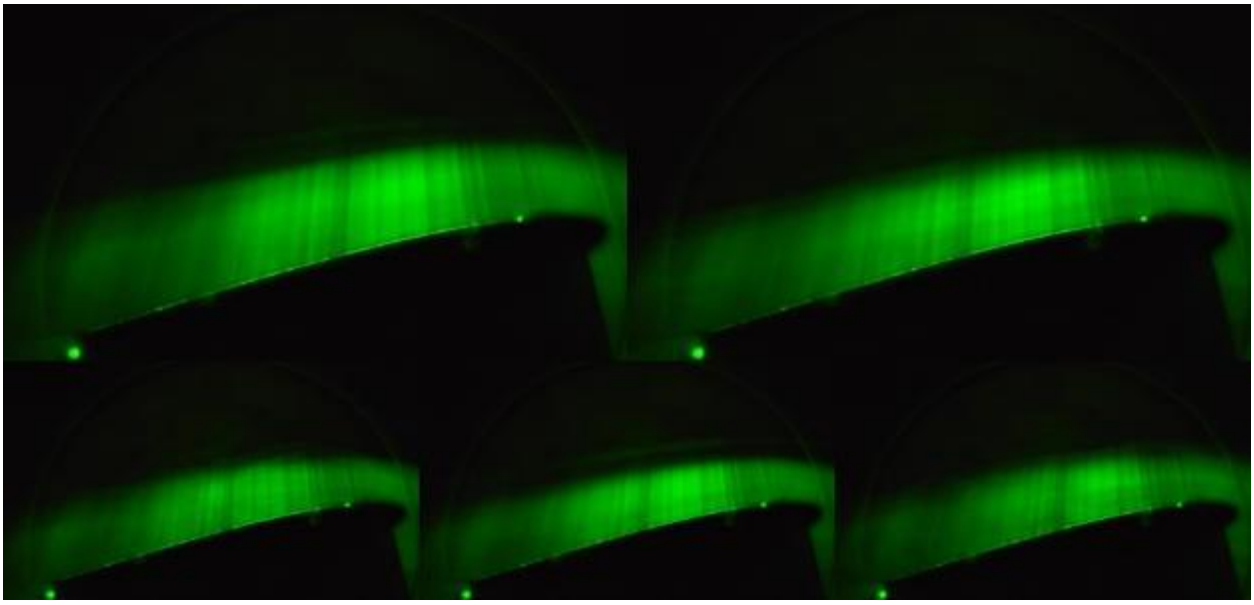

Figure 42: Re = 50,000 α = 13° compiled image comparison

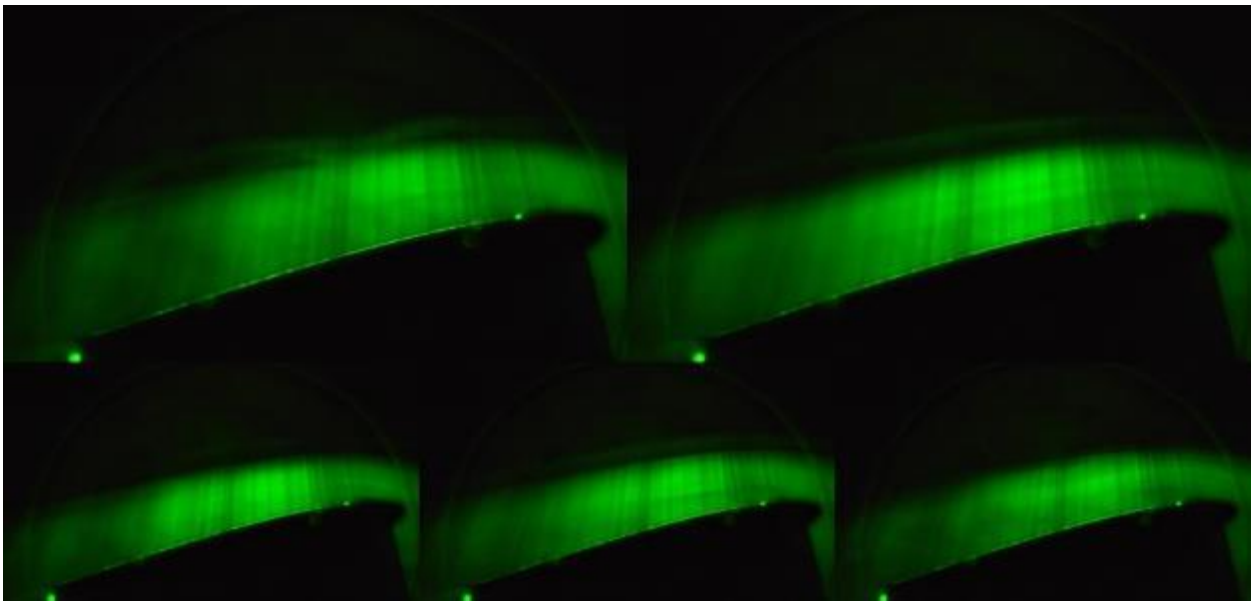

Figure 43: Re = 50,000 α = 14° compiled image comparison

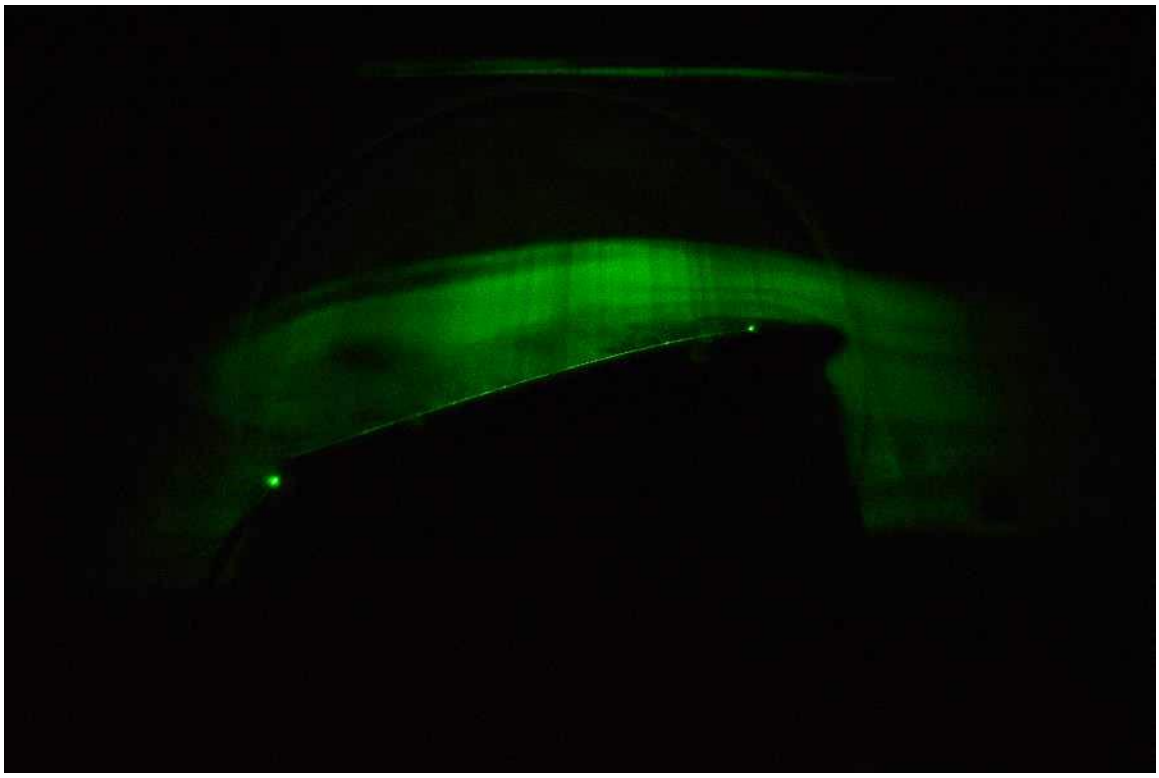

Figure 44: Re = 50,000 α = 14° f = 0 Hz

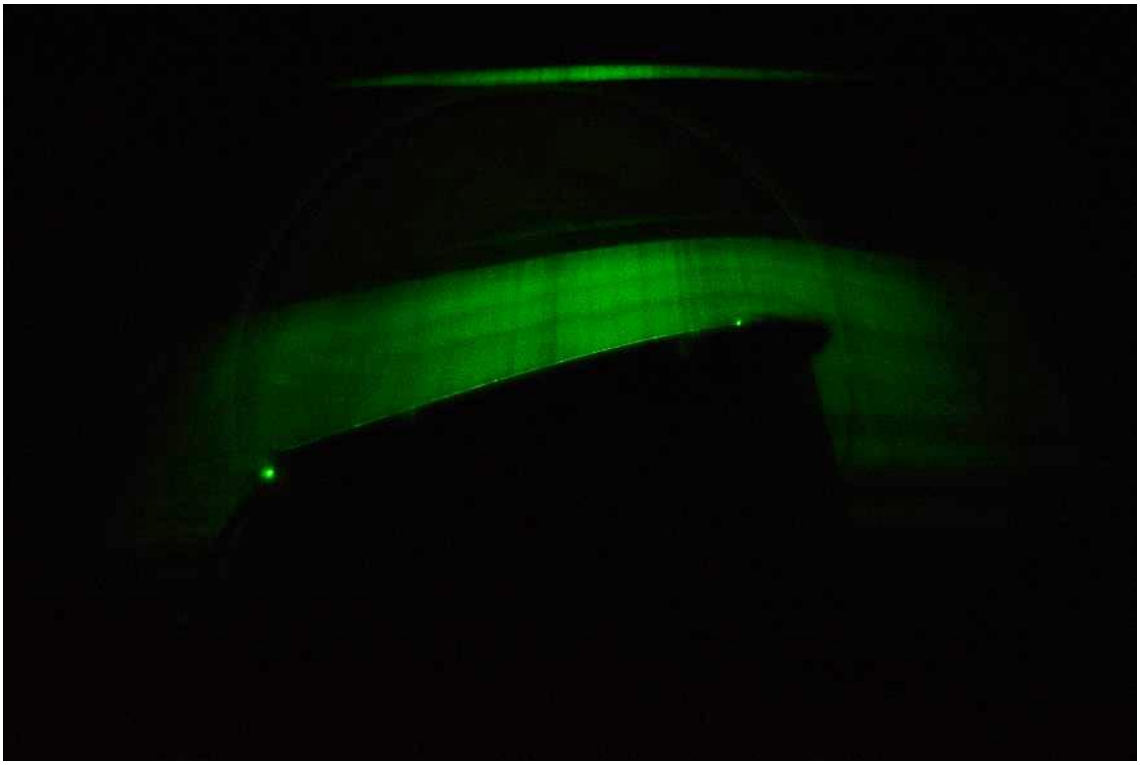

Figure 45: Re = 50,000 α = 14° f = 1400 Hz

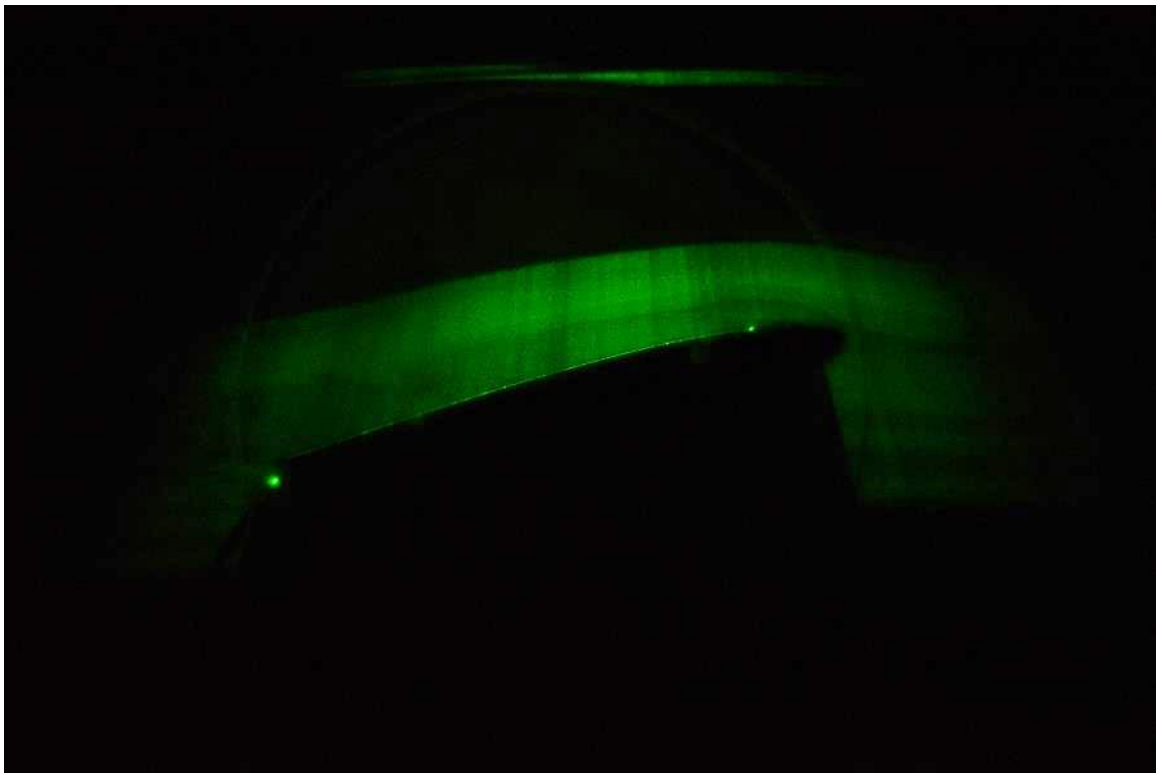

Figure 46: Re = 50,000 α = 14° f = 80 Hz (Strouhal)

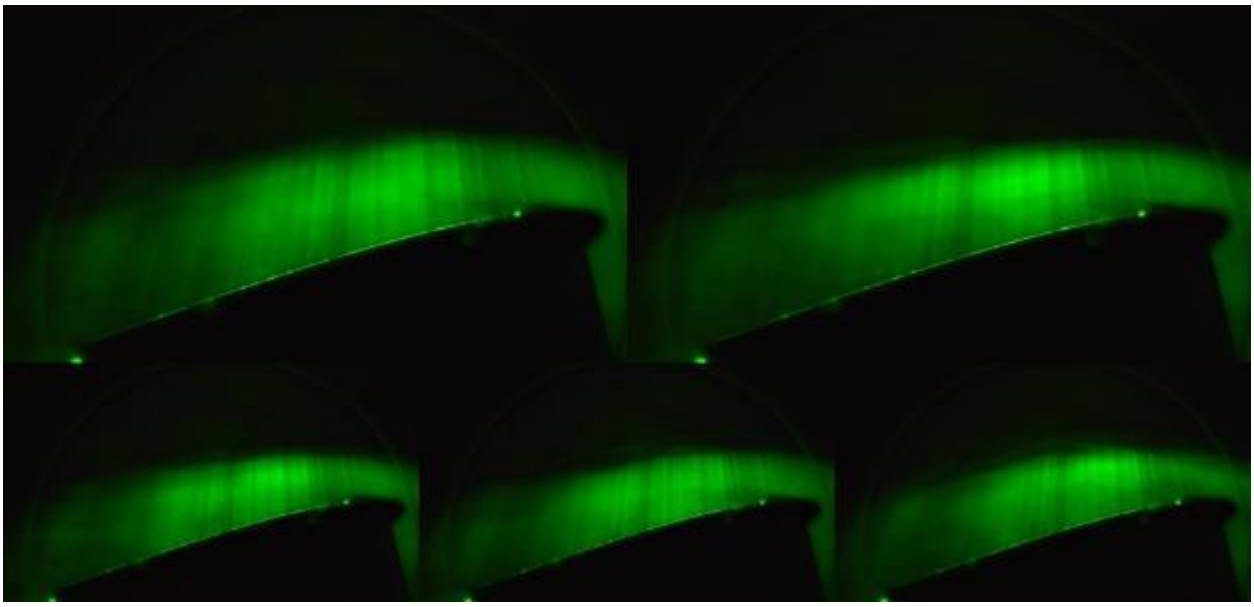

Figure 47: Re = 50,000 α = 15° compiled image comparison

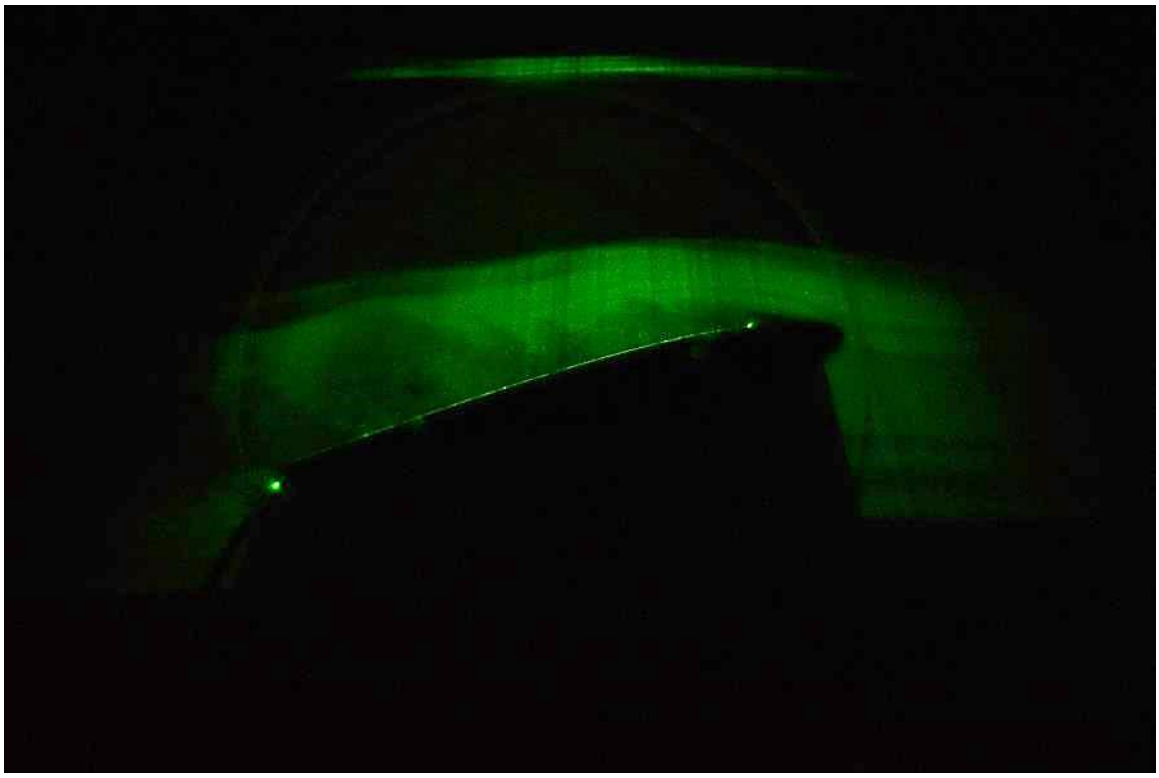

Figure 48: Re = 50,000 α = 15° f = 0 Hz

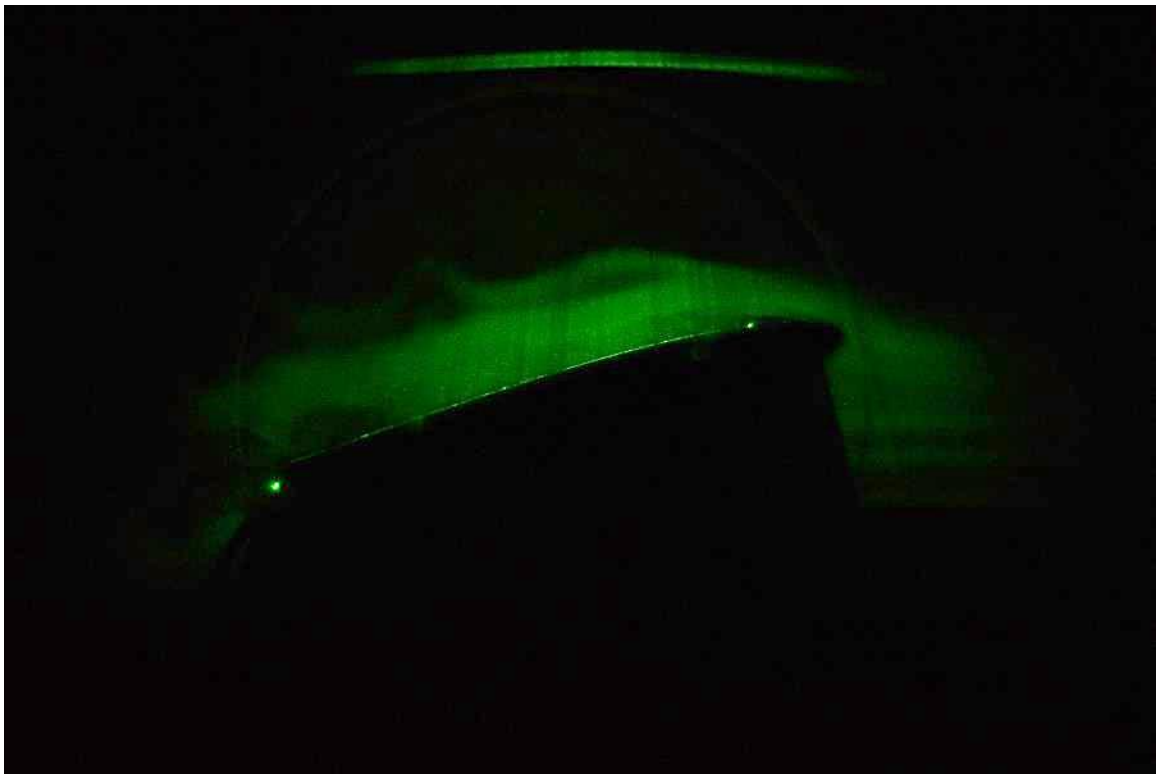

Figure 49: Re = 50,000 α = 15° f = 80 Hz (Strouhal)

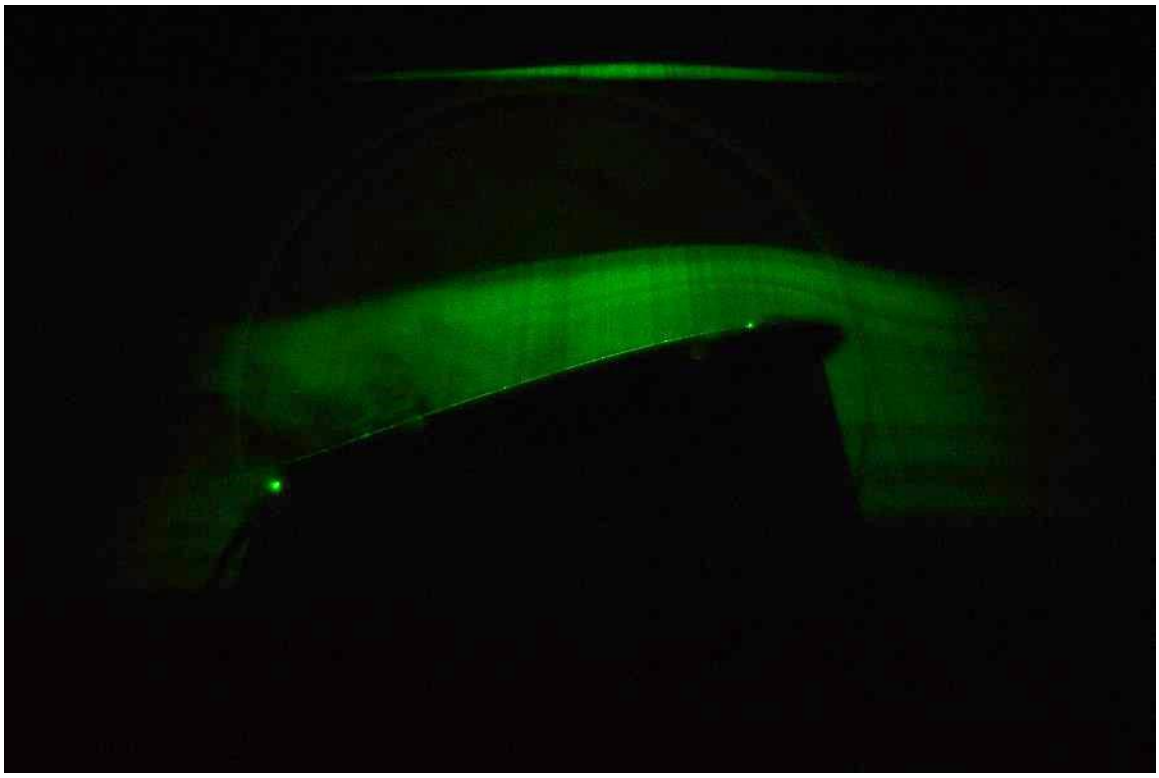

Figure 50: Re = 50,000 α = 15° f = 1400 Hz (oscillatory: control effect)

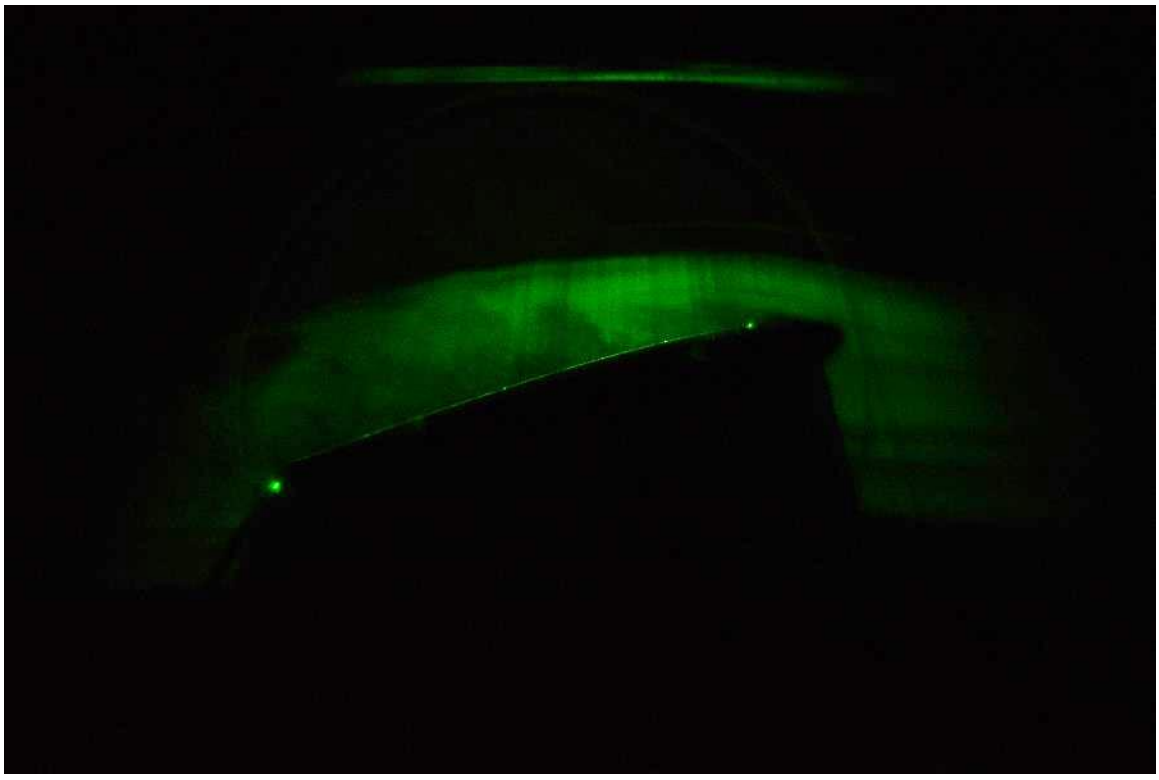

Figure 51: Re = 50,000 α = 15° f = 1400 Hz (oscillatory: no control effect)

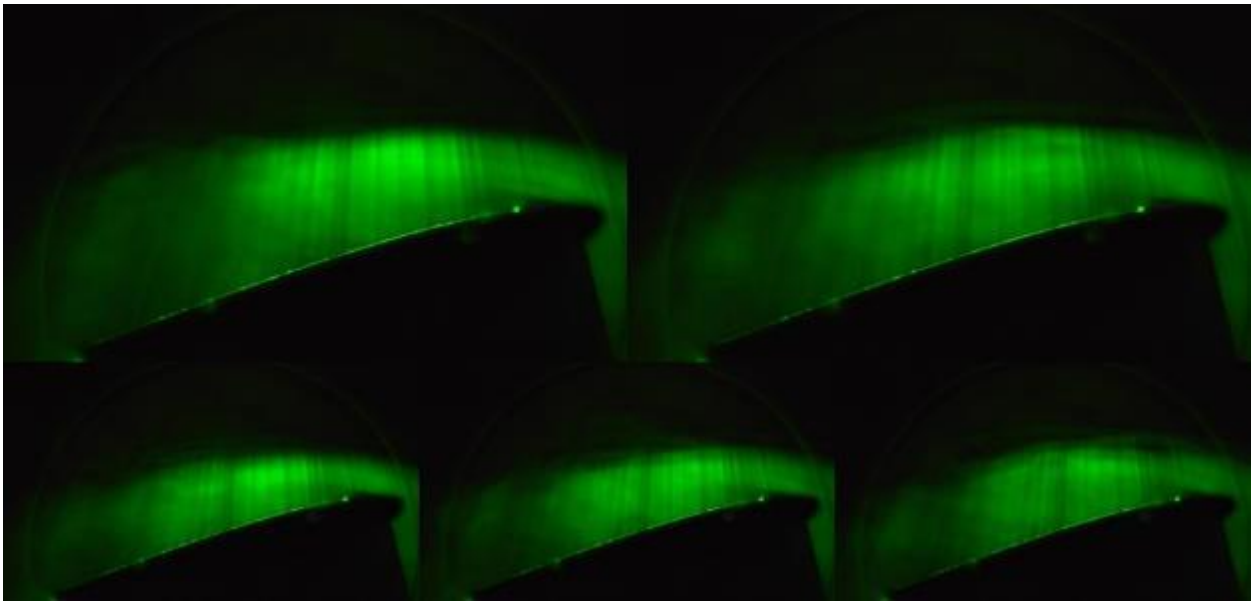

Figure 52: Re = 50,000 α = 16° compiled image comparison

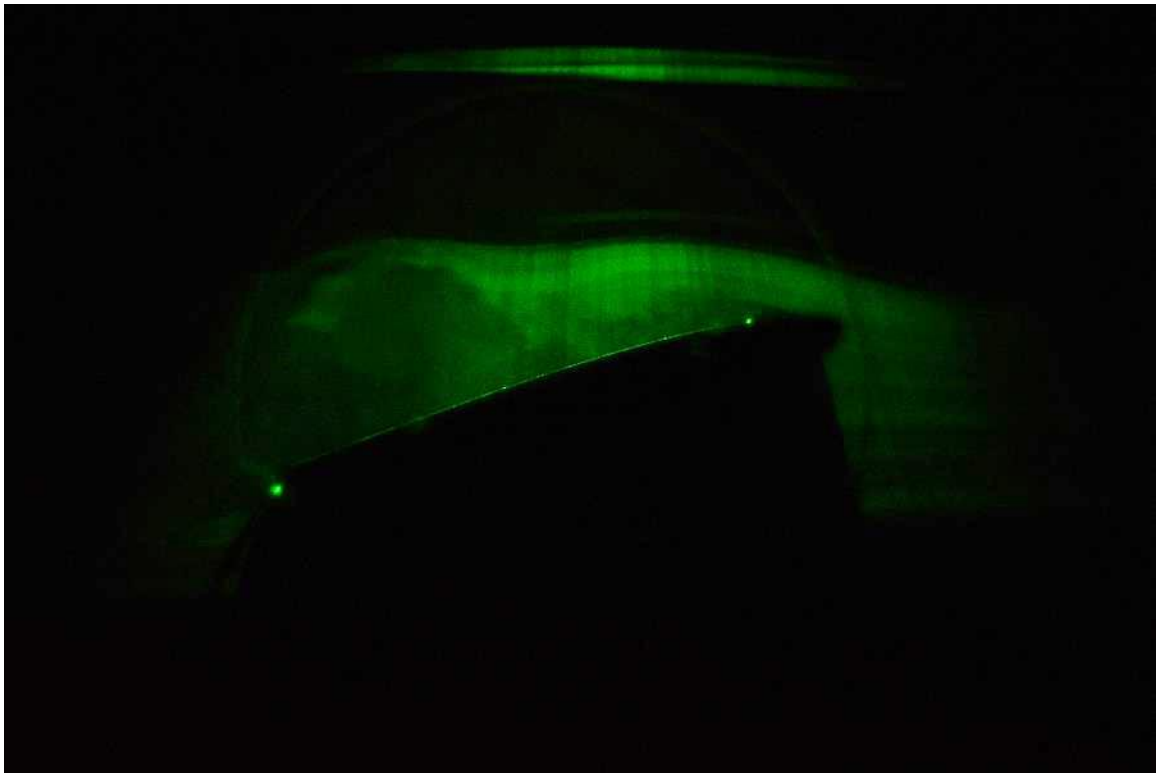

Figure 53: Re = 50,000 α = 16° f = 0 Hz

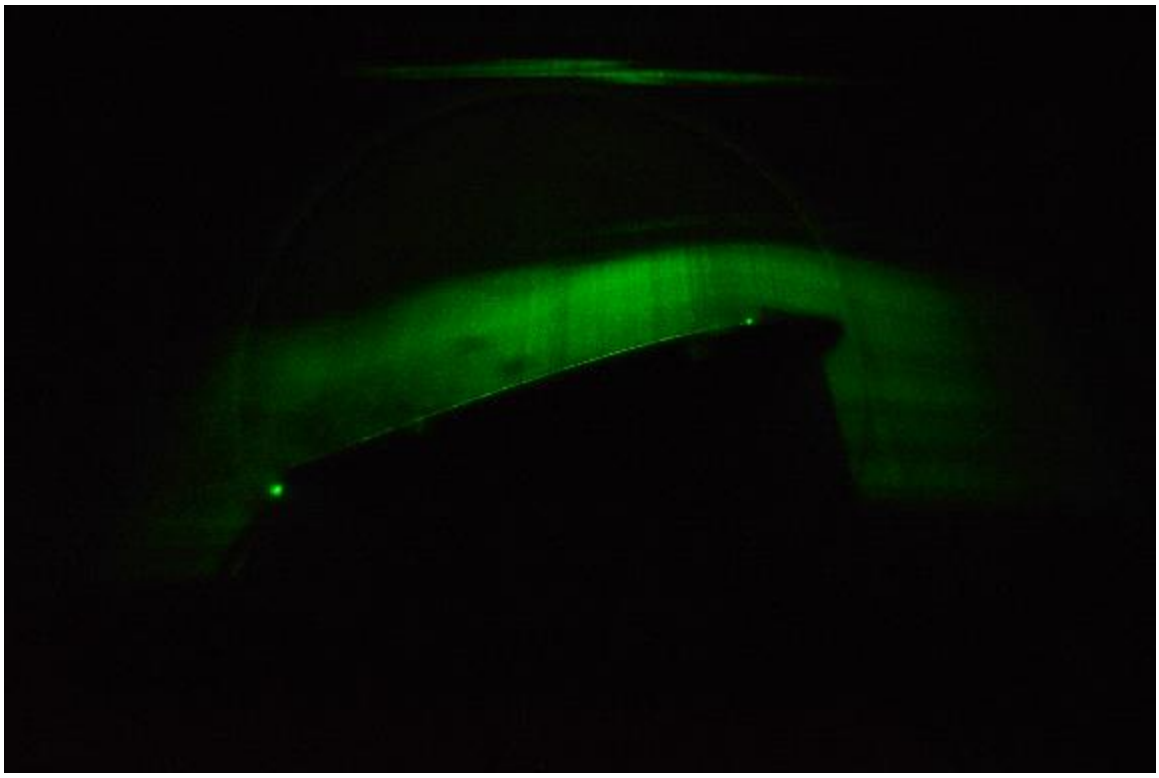

Figure 54: Re = 50,000 α = 16° f = 1400 Hz (oscillatory: control effect)

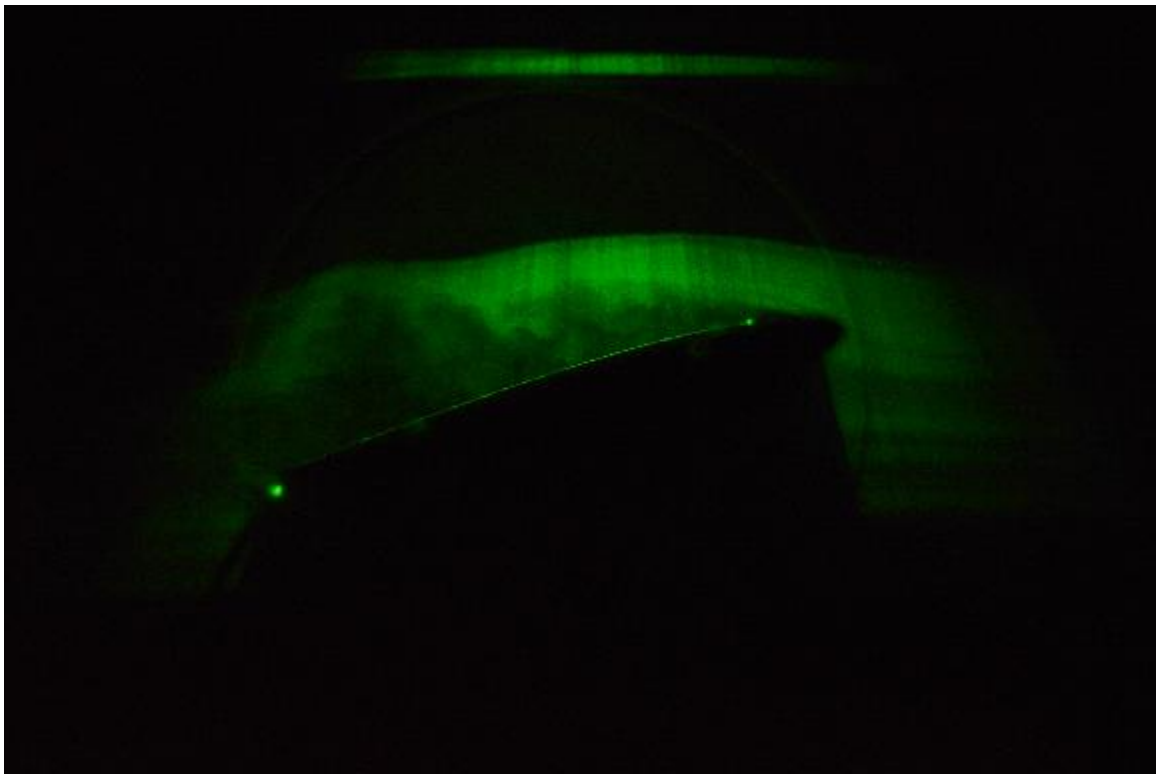

Figure 55: Re = 50,000 α = 16° f = 1400 Hz (oscillatory: no control effect)

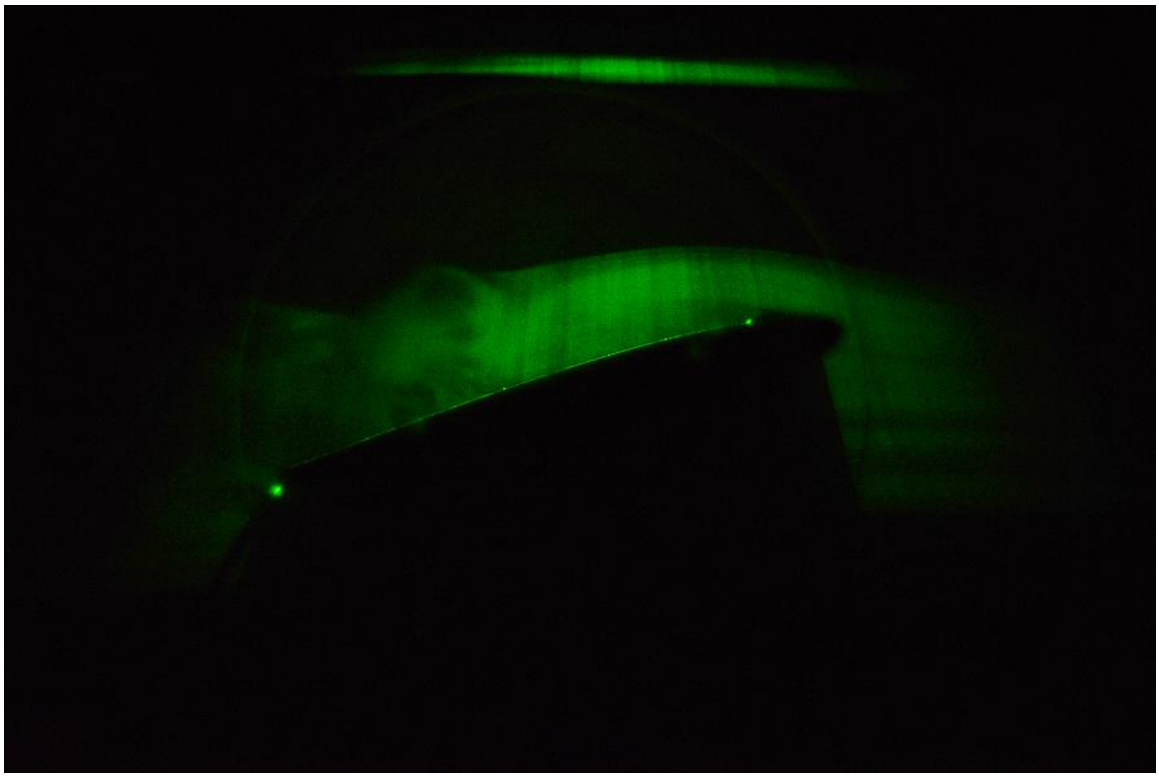

Figure 56: Re = 50,000 α = 16° f = 80 Hz (Strouhal) (oscillatory: control effect)

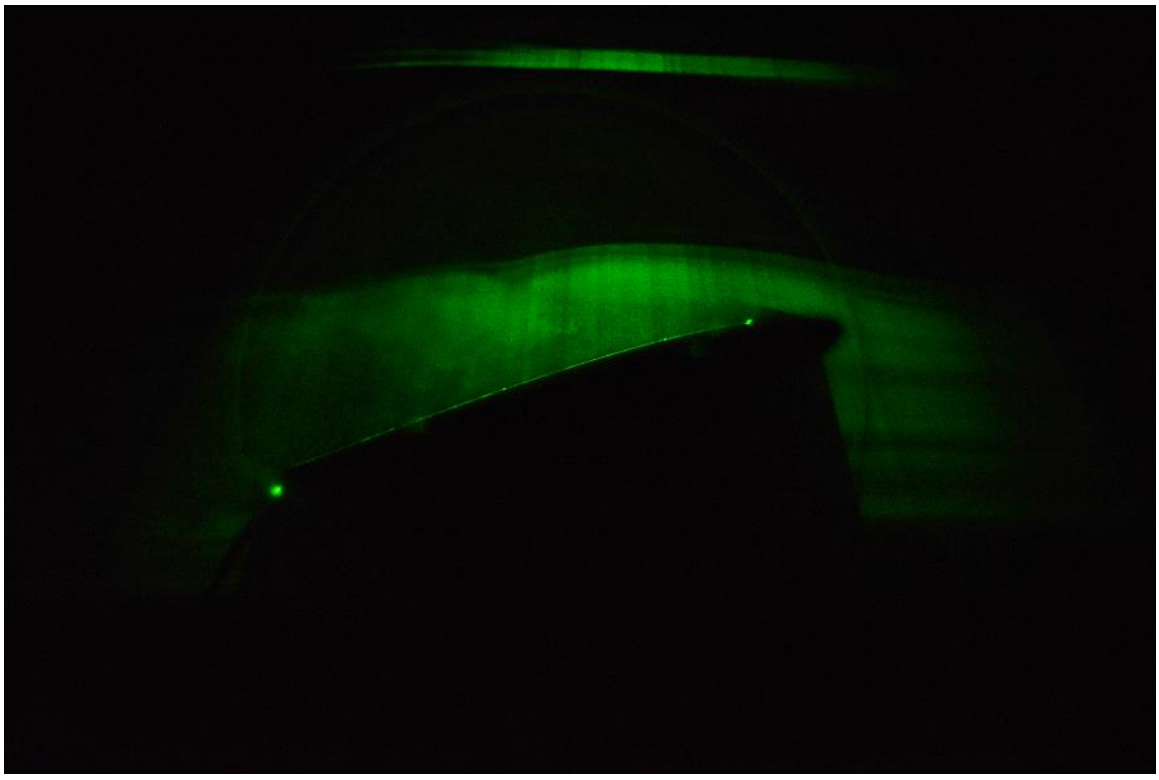

Figure 57: Re = 50,000 α = 16° f = 80 Hz (Strouhal) (oscillatory: no control effect)

Reynolds Number 75,000

As with Reynolds number of 50,000, angle of attack of 13° shows no interesting results. Angle of attack of 14° also shows no interesting results with the flow appearing to stay attached in all cases. For angle of attack of 15°, the compiled images in Figure 60 show a slight difference between the clean and steady-on case, flow behavior. By comparing individual images of the clean case in Figure 61 and the steady-on case in Figure 62, it can be seen there is some controlling effect that the actuator has. The Strouhal pulsing case also appears to exhibit and oscillatory behavior between a controlling effect as seen in Figure 63, and no controlling effect as seen in Figure 64. For angle of attack of 16° there appears to be no control at any of the cases.

Reynolds Number 75,000

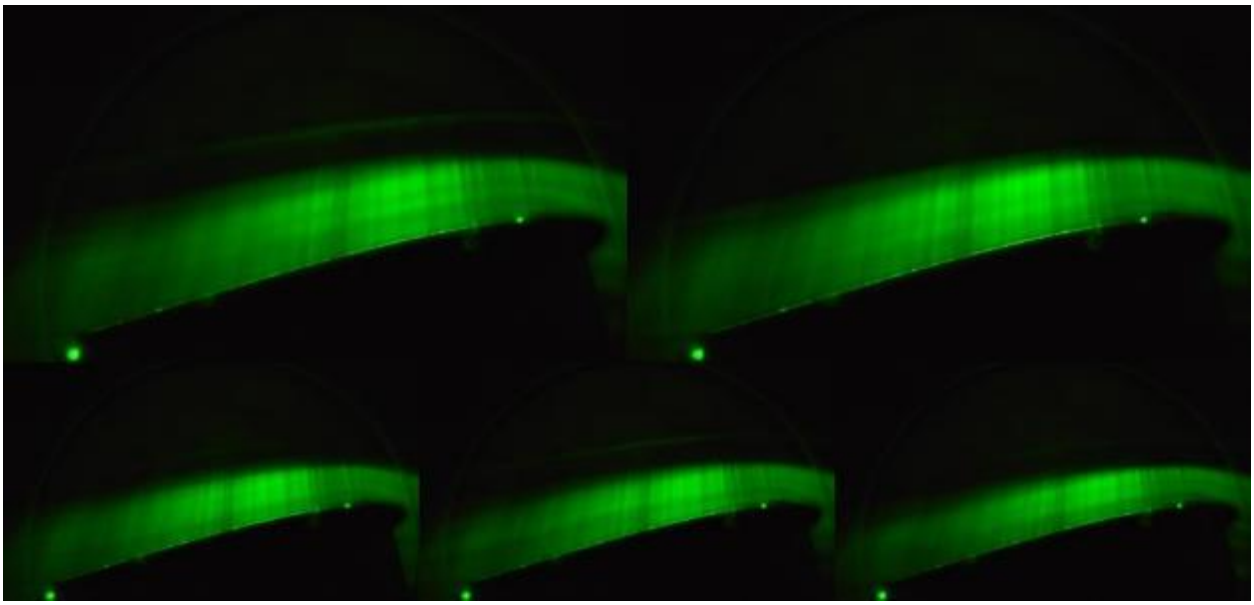

Figure 58: Re = 75,000 α = 13° compiled image comparison

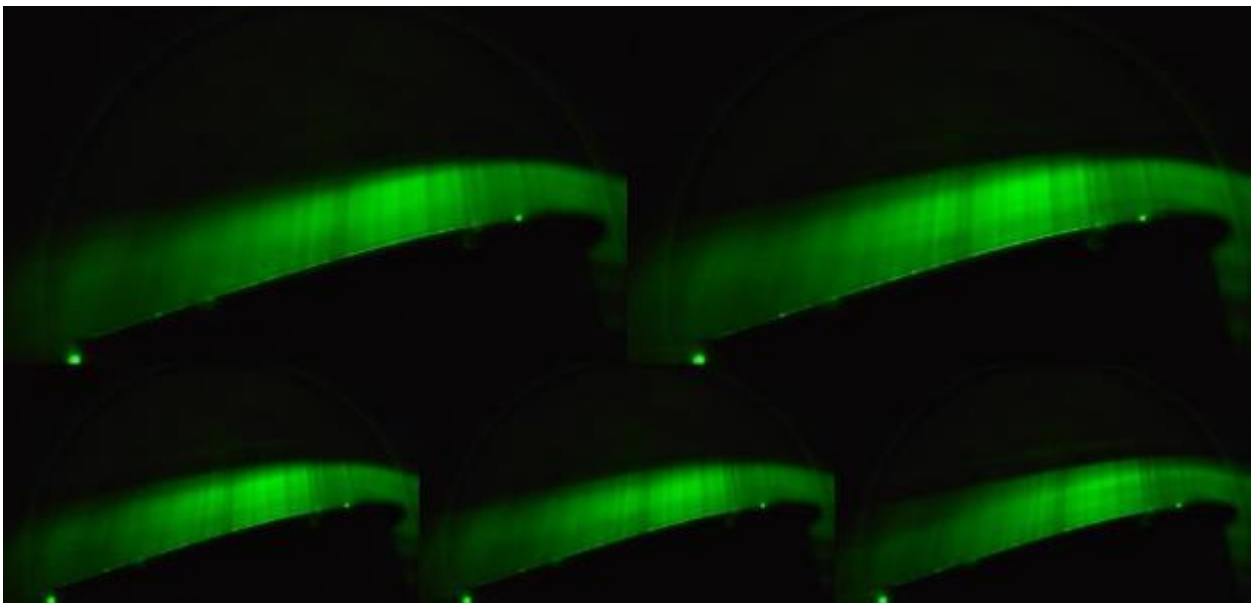

Figure 59; Re = 75,000 α = 14° compiled image comparison

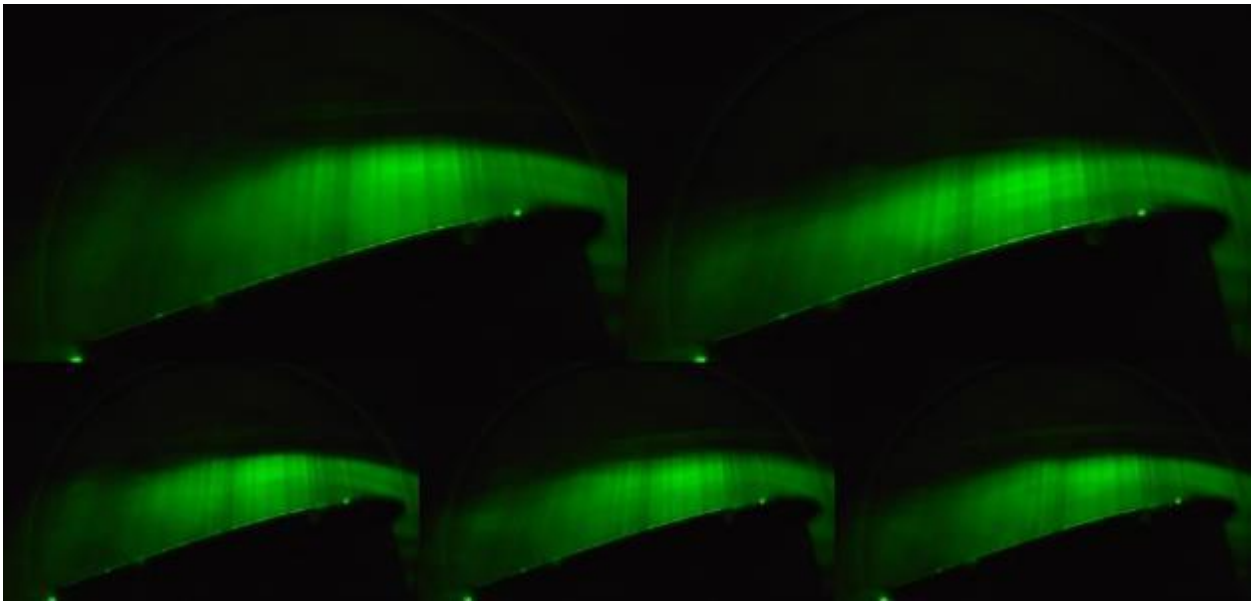

Figure 60: Re = 75,000 α = 15° compiled image comparison

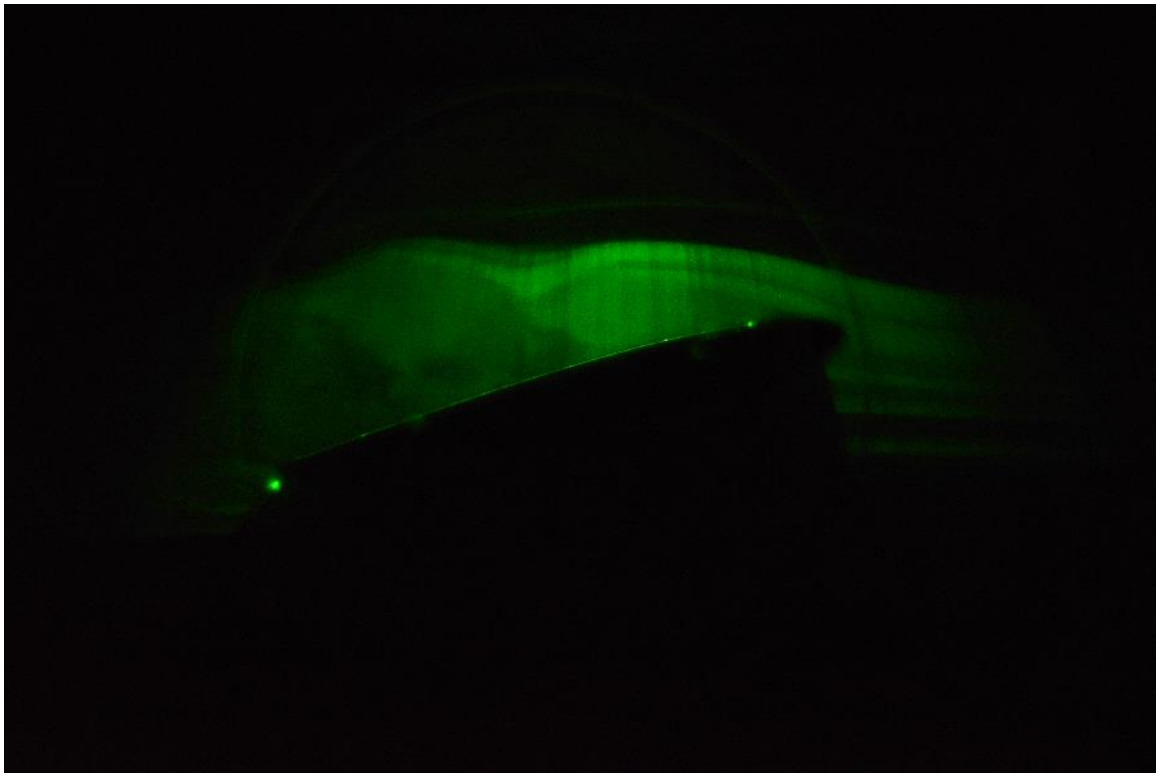

Figure 61: Re = 75,000 α = 15° f = 0 Hz

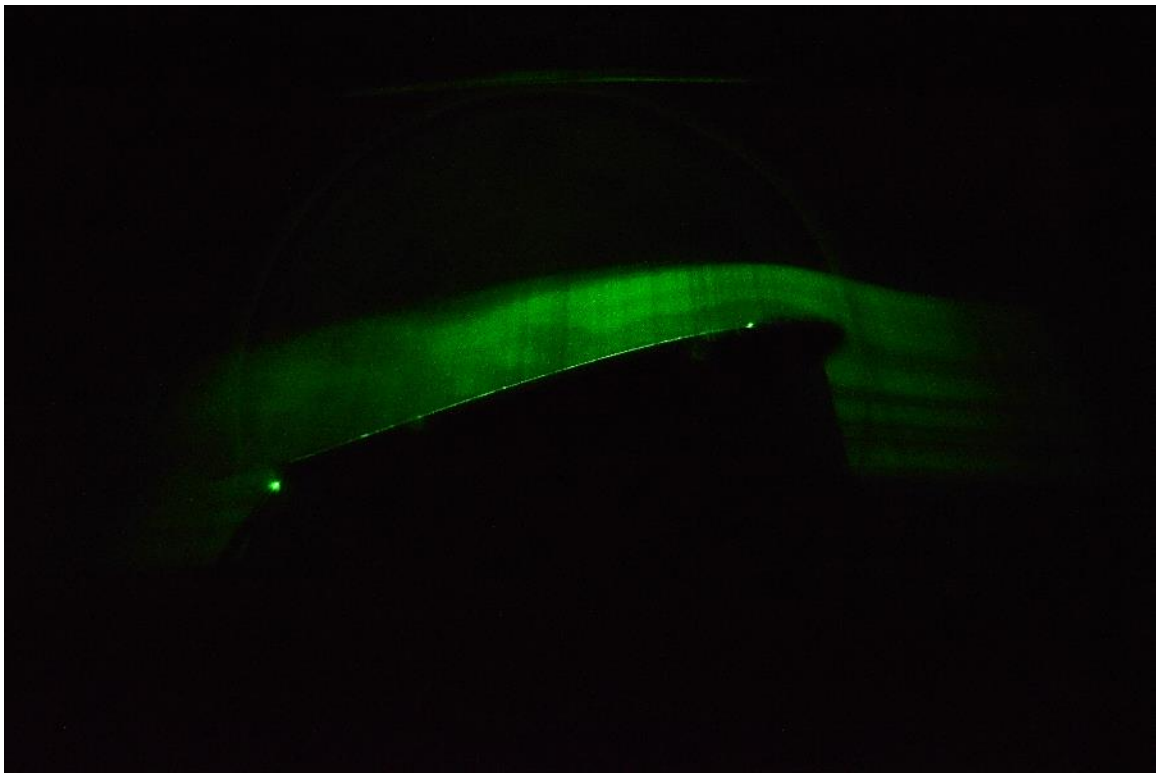

Figure 62: Re = 75,000 α = 15° f = 1400 Hz

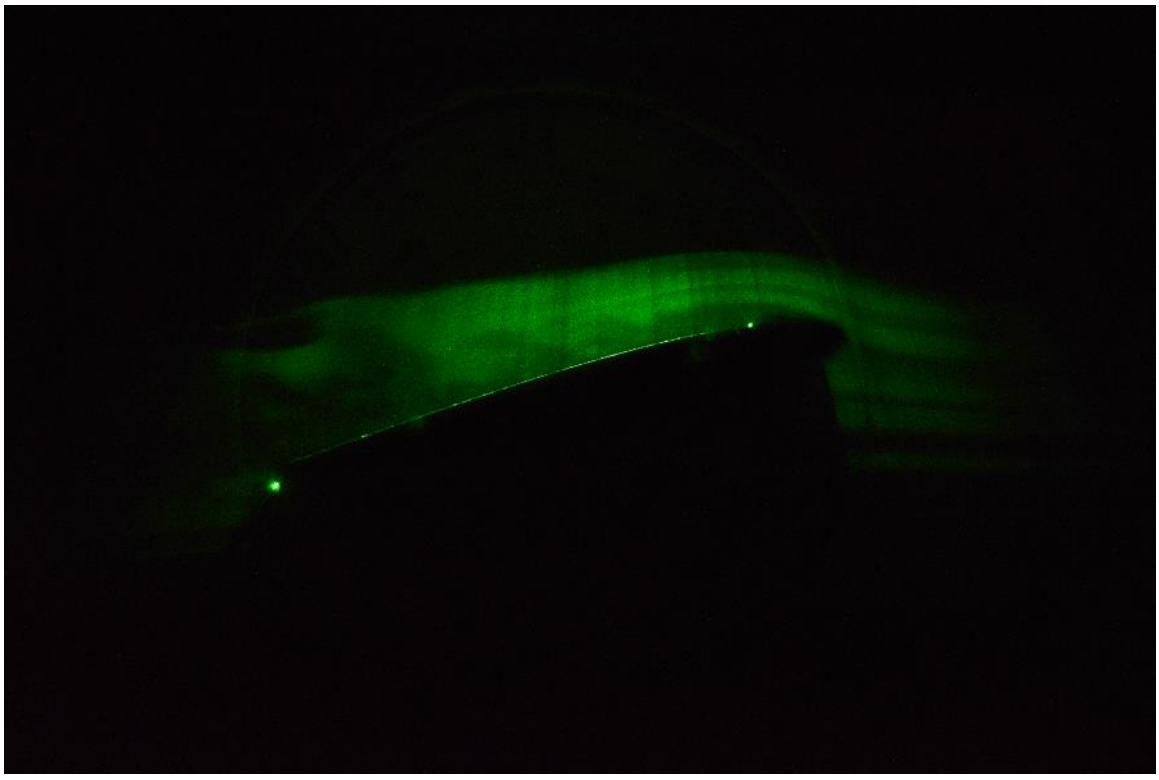

Figure 63: Re = 75,000 α = 15° f = 120 Hz (Strouhal) (oscillatory: control effect)

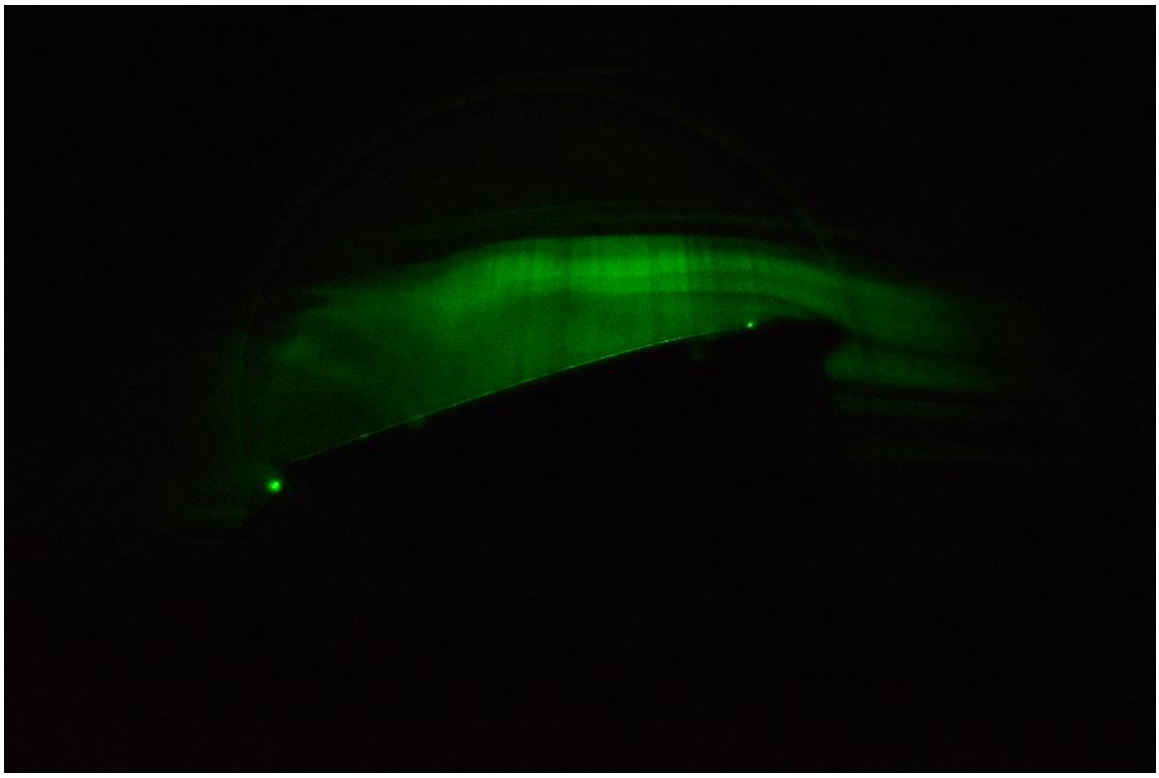

Figure 64: Re = 75,000 α = 15° f = 120 Hz (Strouhal) (oscillatory: no control effect)

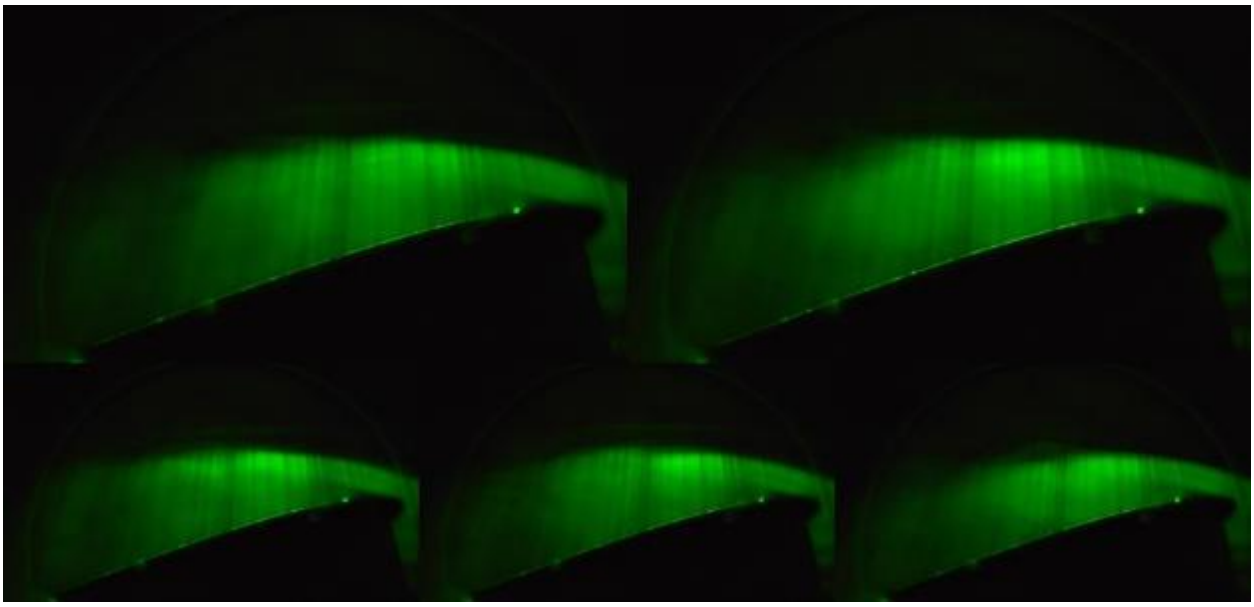

Figure 65: Re = 75,000 α = 16° compiled image comparison

Reynolds Number 100,000

For Reynolds number of 100,000 there were no significant findings at angles of attack of 13° or 14°. For angle of attack at 15°, the flow appears to be attached in the compiled images in Figure 68 however by inspecting individual images it can be seen that separation is occurring as seen in Figure 69. Inspecting individual images of all the plasma on cases there appears to be no controlling effect. For angle of attack of 16° the also appears to be no effect for any case.

Reynolds Number 100,000

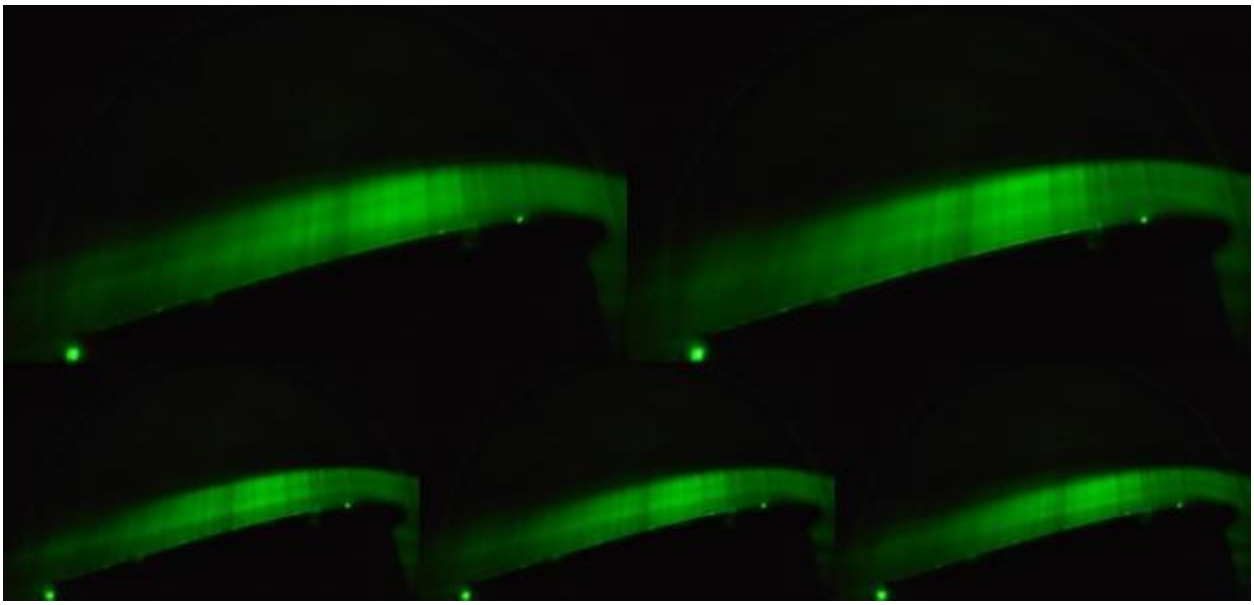

Figure 66: Re = 100,000 α = 13° compiled image comparison

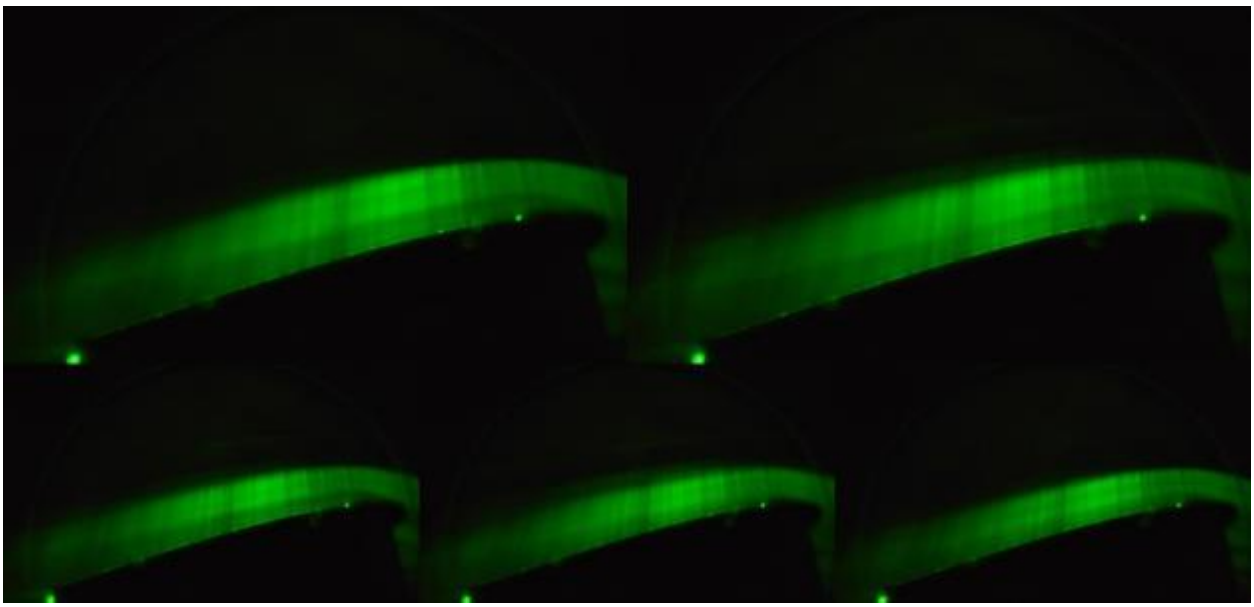

Figure 67: Re = 100,000 α = 14° compiled image comparison

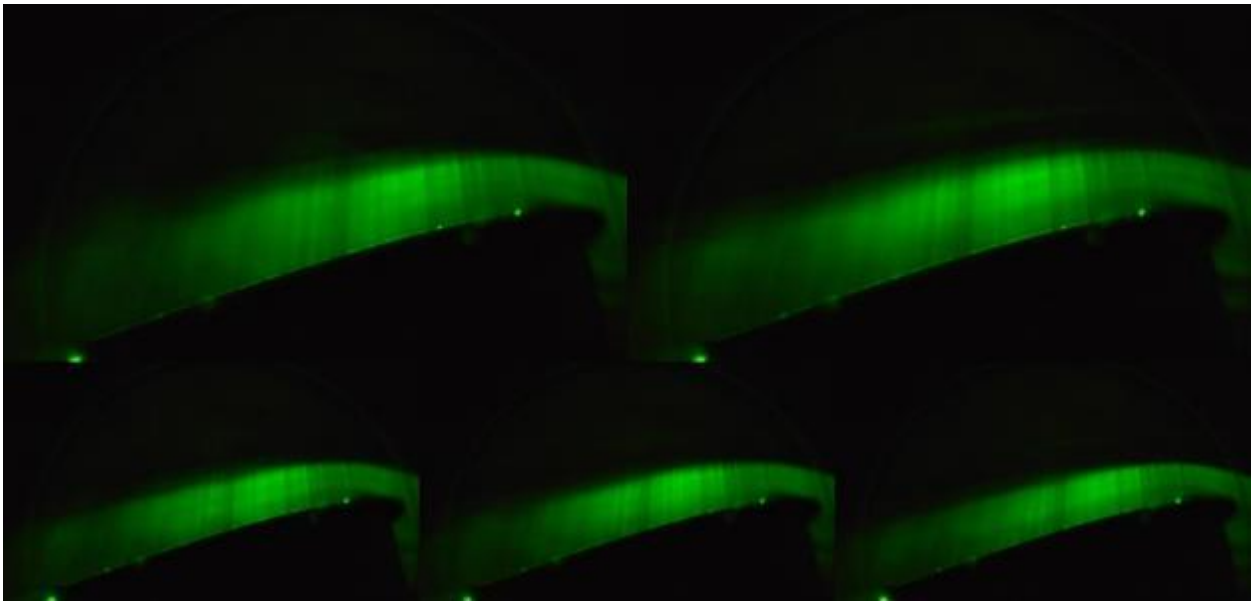

Figure 68: Re = 100,000 α = 15° compiled image comparison

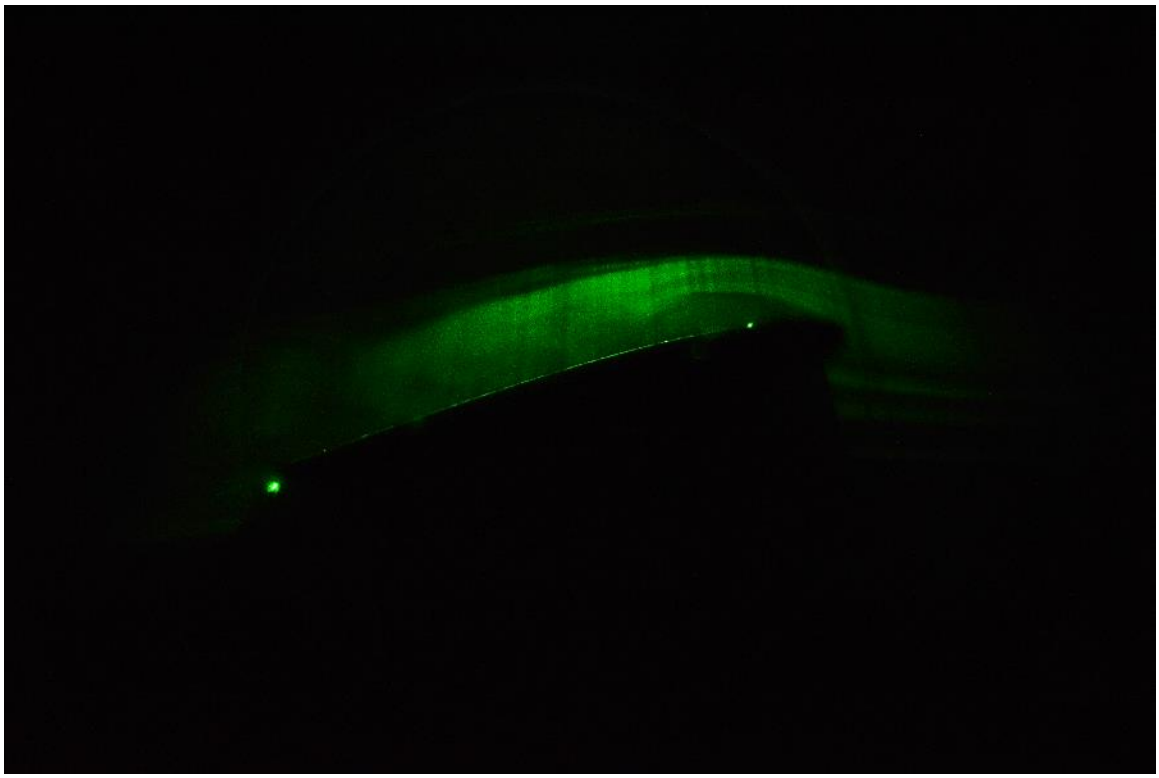

Figure 69: Re = 100,000 α = 15° f = 0 Hz

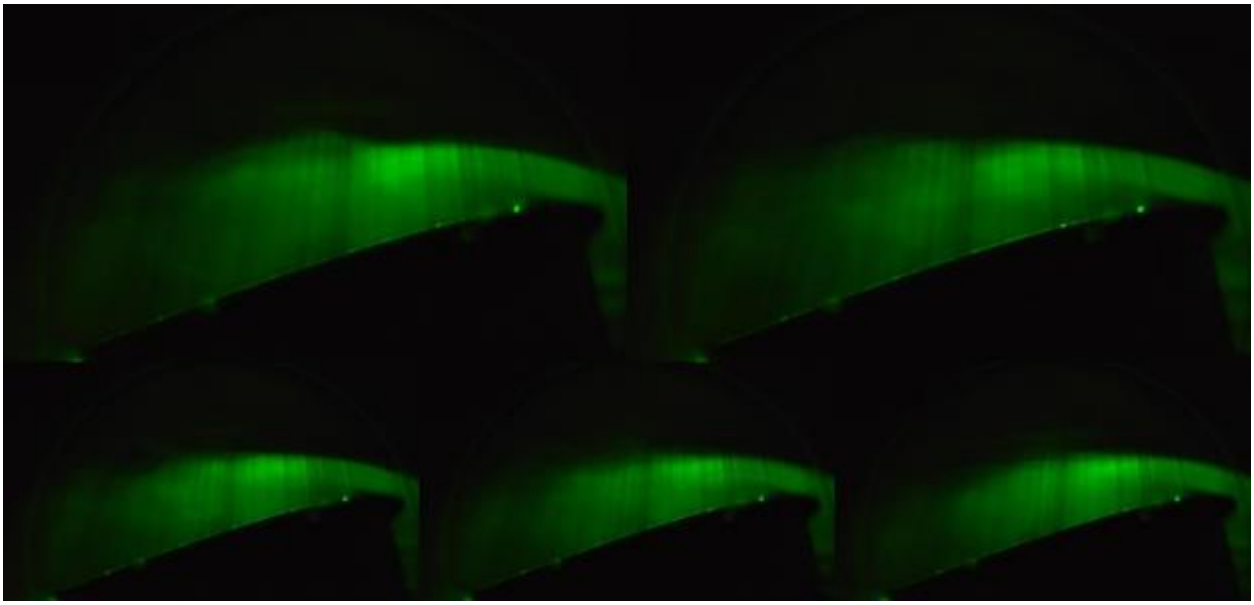

Figure 70: Re = 100,000 α = 16° compiled image comparison

Reynolds Number 125,000

For Reynolds number of 125,000 none of the cases seem to show any controlling effect with the low power plasma actuator on.

Reynolds Number 125,000

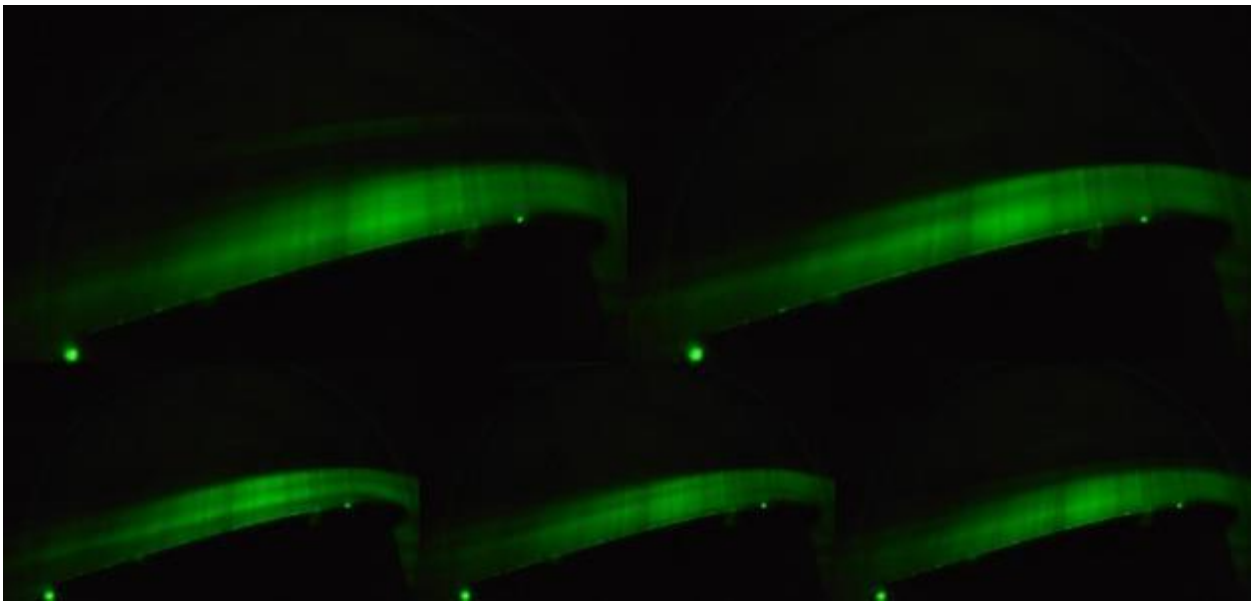

Figure 71: Re = 125,000 α = 13° compiled image comparison

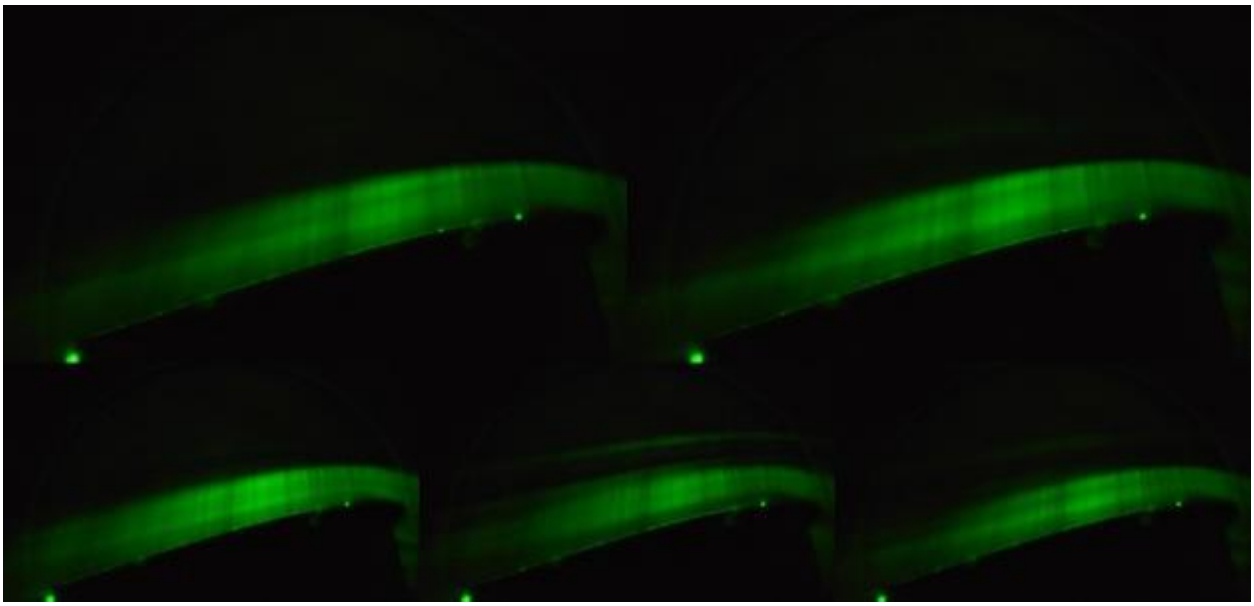

Figure 72: Re = 125,000 α = 14° compiled image comparison

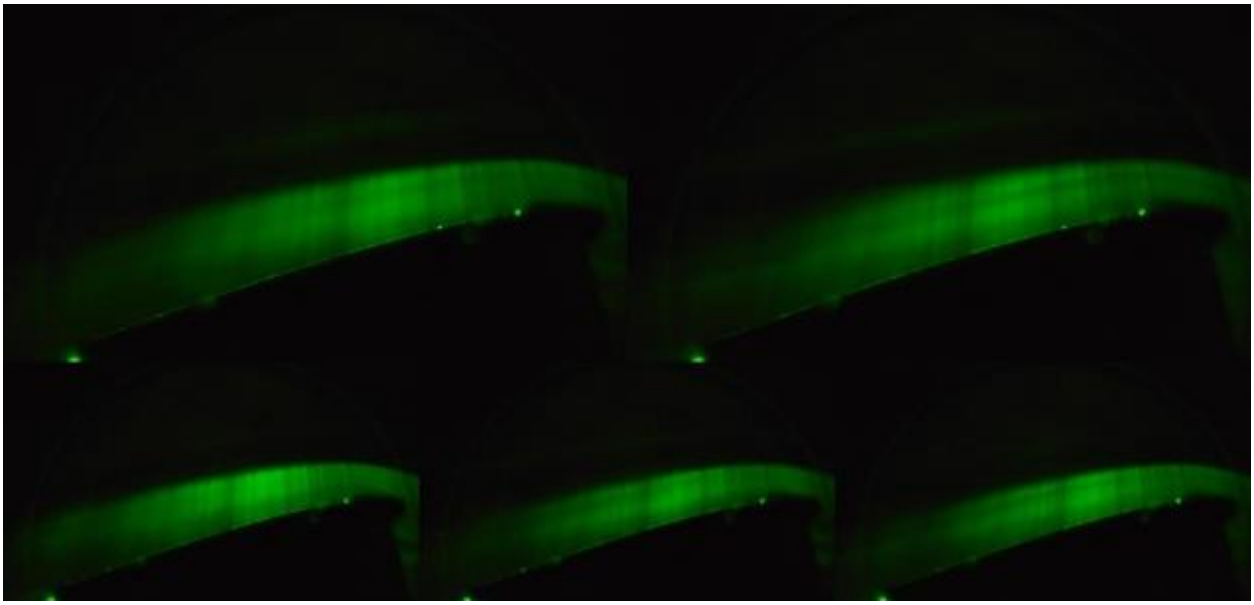

Figure 73: Re = 125,000 α = 15° compiled image comparison

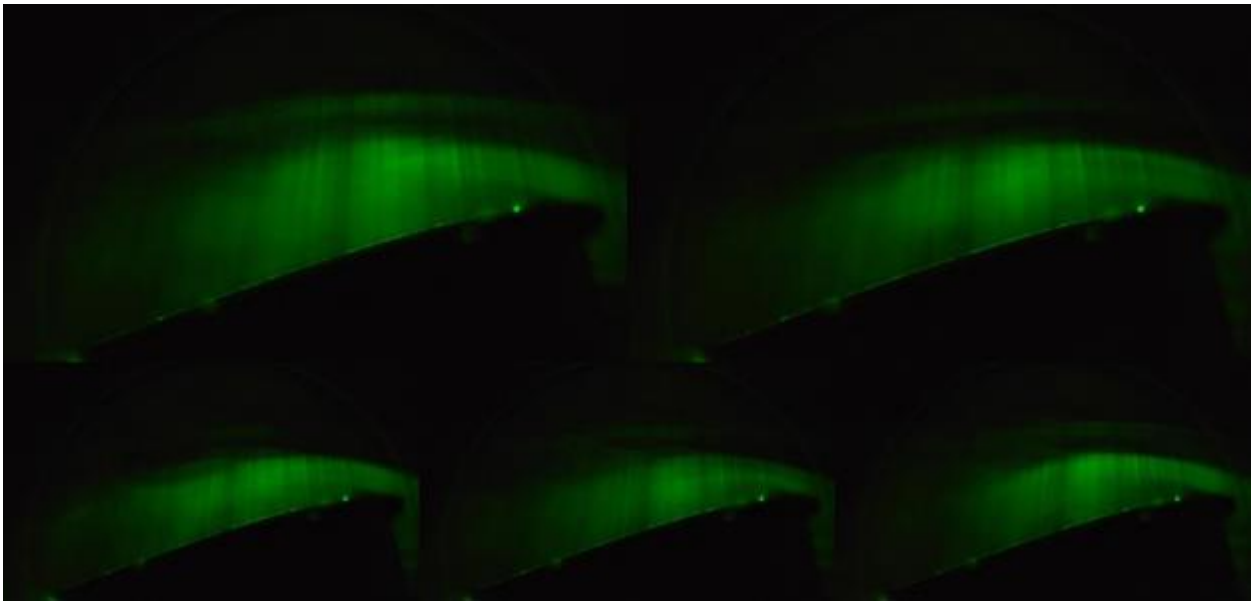

Figure 74: Re = 125,000 α = 16° compiled image comparison

High Power DBD Results

The high power testing was carried out with a DBD with a 1/8 in. gap that starts at approximately 6% chord. The wider gap requires a higher voltage to reach plasma formation and thus runs at a higher power requirement. At the resonant frequency of 1700 Hz for the high power, actuator circuit the power was 9.57 ± 0.174 W (≈188 W/m) with a voltage potential of approximately 15.4 kV between the electrodes. Data was collected for the high power DBD at all five Reynolds numbers that the low power testing was conducted at, but only at nominal angles of attack of 15° and 16° and for plasma off (clean) and plasma on but not pulsing (steady). It can be seen from Figure 75 and Figure 76 that the actuator had some controlling effect for both angles of attack at Reynolds number 25,000. For Reynolds number of 50,000 it can be seen from Figure 77 that there appears to be a controlling effect for angle of attack 15°. Figure 78 shows that there appears to be no effect at 16° for Reynolds number of 50,000. For Reynolds number of 75,000 Figure 79 shows there appears to be some effect at angle of attack of 15° and Figure 80 appears to show no effect. For Reynolds number of 100,000 Figure 81 appears to show a small effect at angle of attack of 15° with the flow being turned slightly downwards near the leading edge for the steady case in comparison to the clean case. The clean flow behavior for 15° at Reynolds number of 100,000 appears significantly different from the observed behavior at the same conditions for low power testing. This could be attributed to either a combination of uncertainty in the actual angle of attack and/or the physical geometric differences between the actuators, which alter the wing surface at their location due to their physical thickness of a few thousandths of an inch. Figure 82 appears to show no effect at angle of attack of 16° for Reynolds number 100,000. For Reynolds number of 125,000 both Figure 83 and Figure 84, appear to show no effect at both angles of attack.

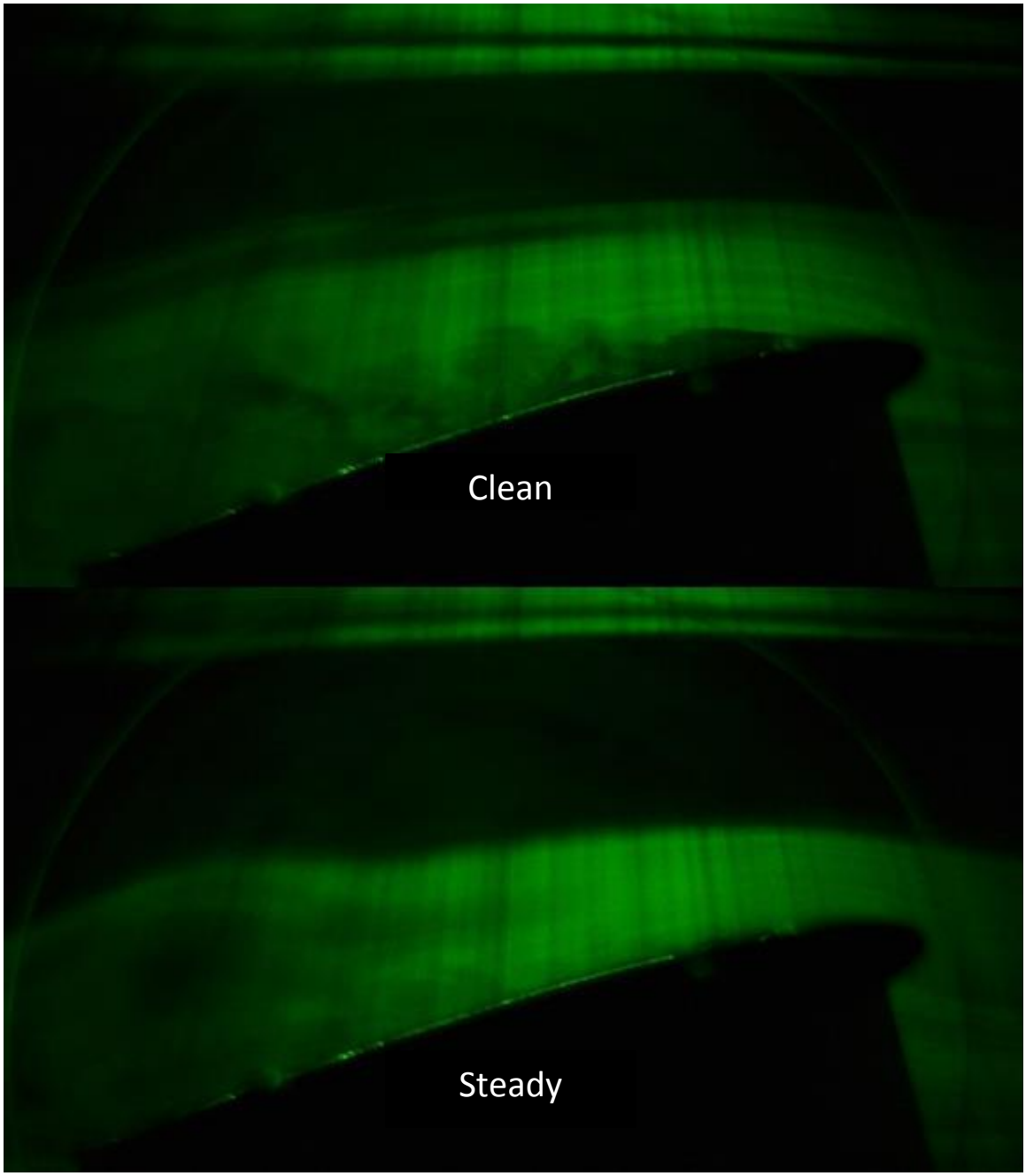

Figure 75: Re = 25,000 α = 15° Clean vs Steady

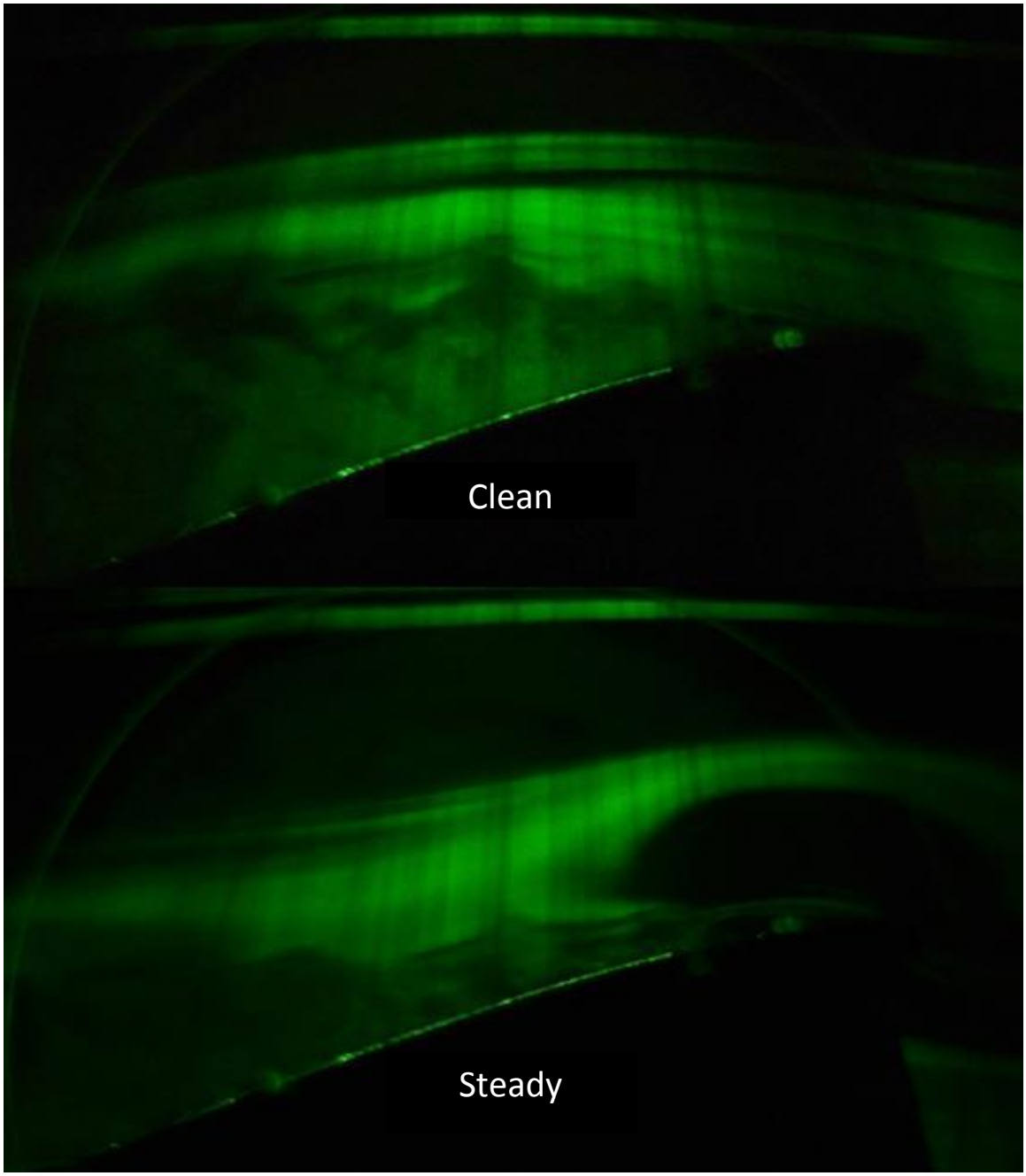

Figure 76: Re = 25,000 α = 16° Clean vs Steady

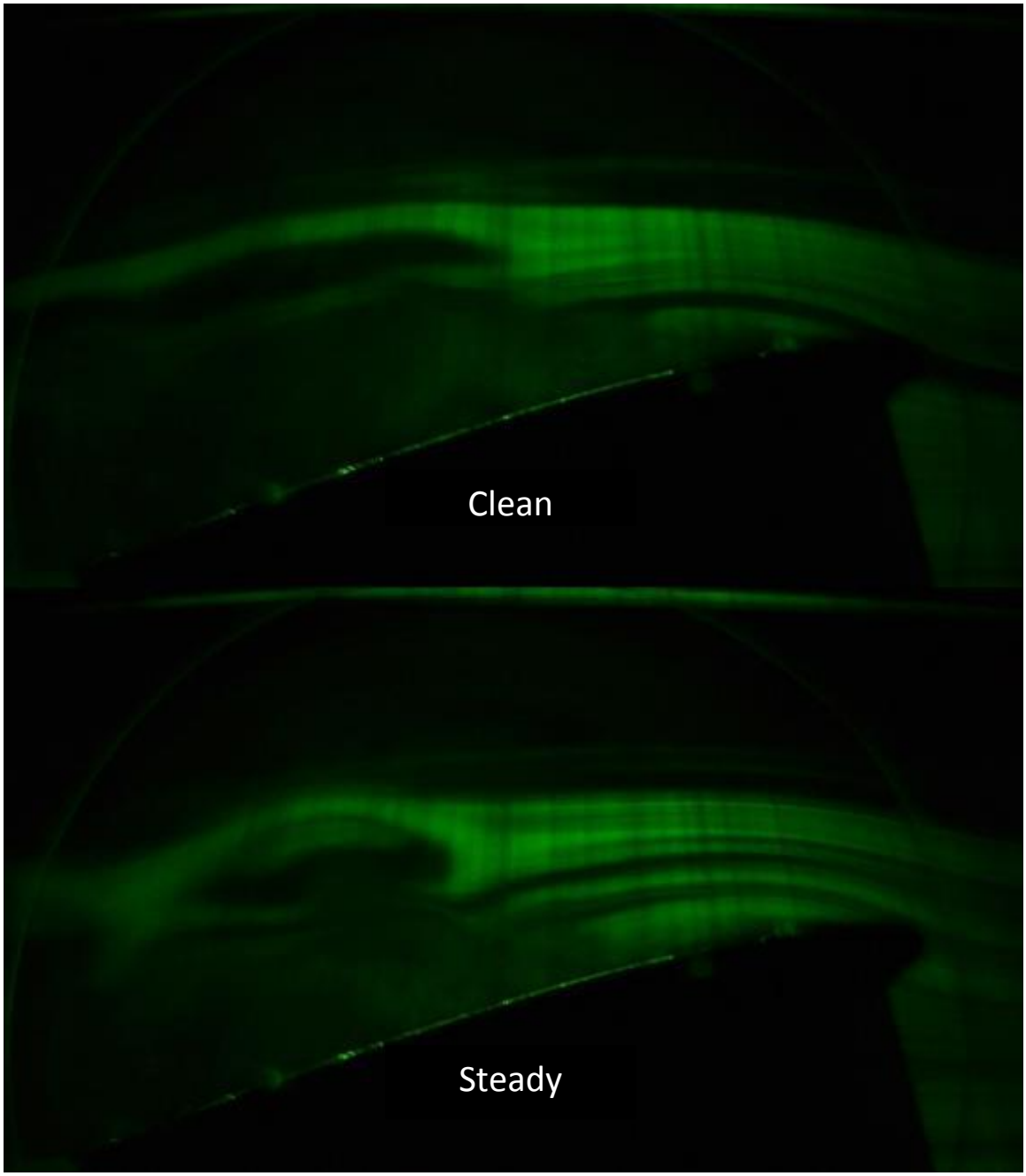

Figure 77: Re = 50,000 α = 15° Clean vs Steady

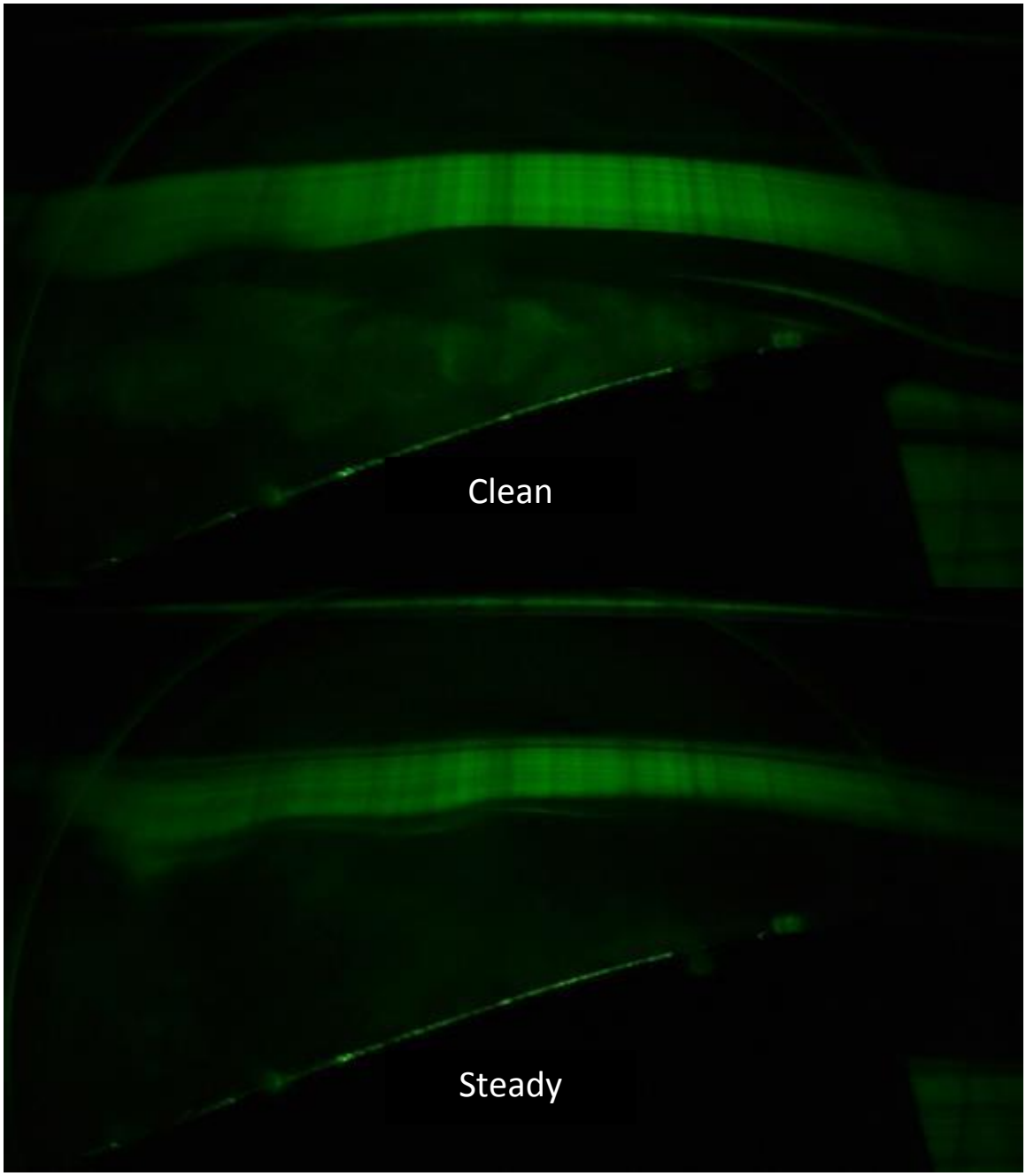

Figure 78: Re = 50,000 α = 16° Clean vs Steady

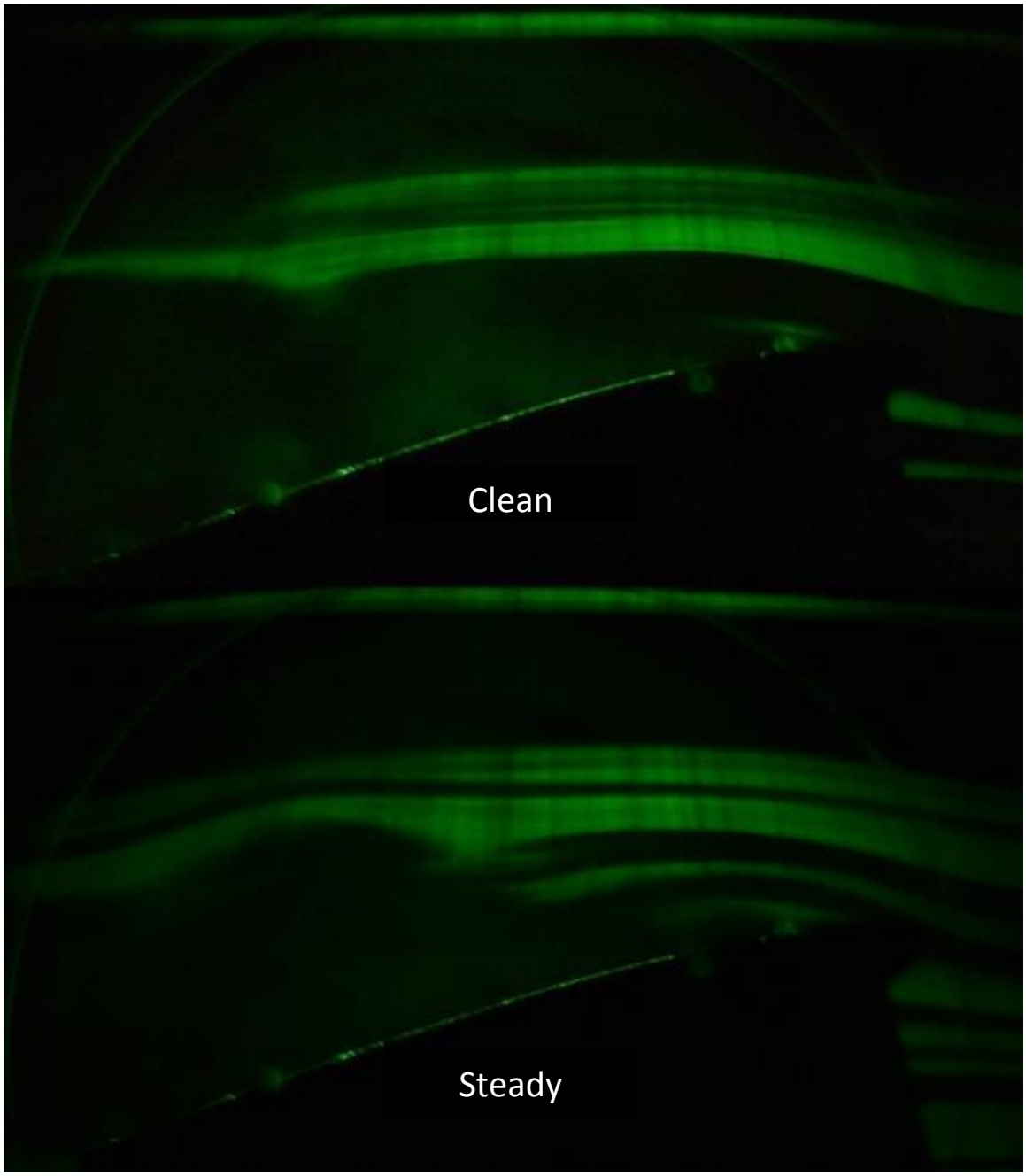

Figure 79: Re = 75,000 α = 15° Clean vs Steady

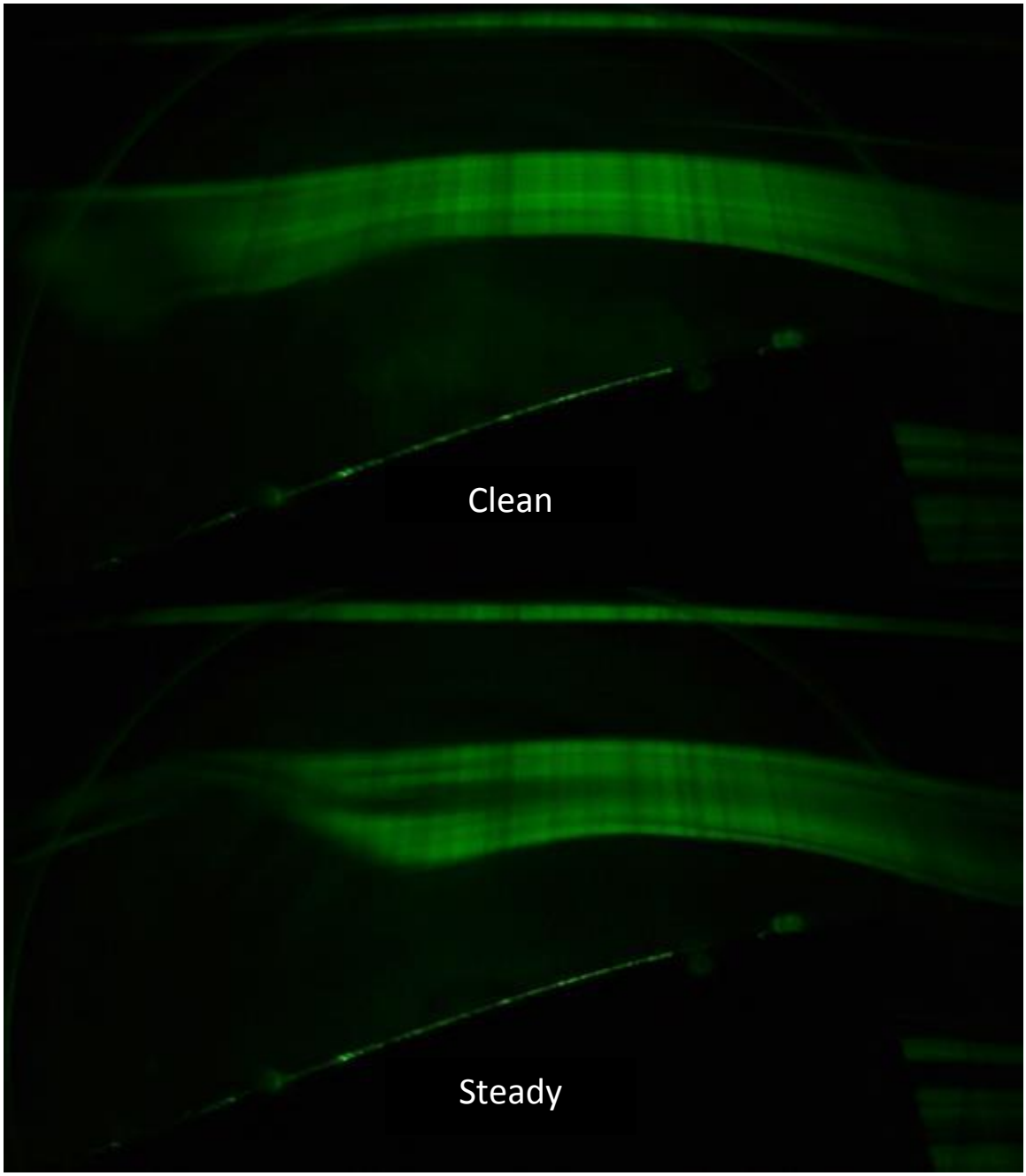

Figure 80: Re = 75,000 α = 16° Clean vs Steady

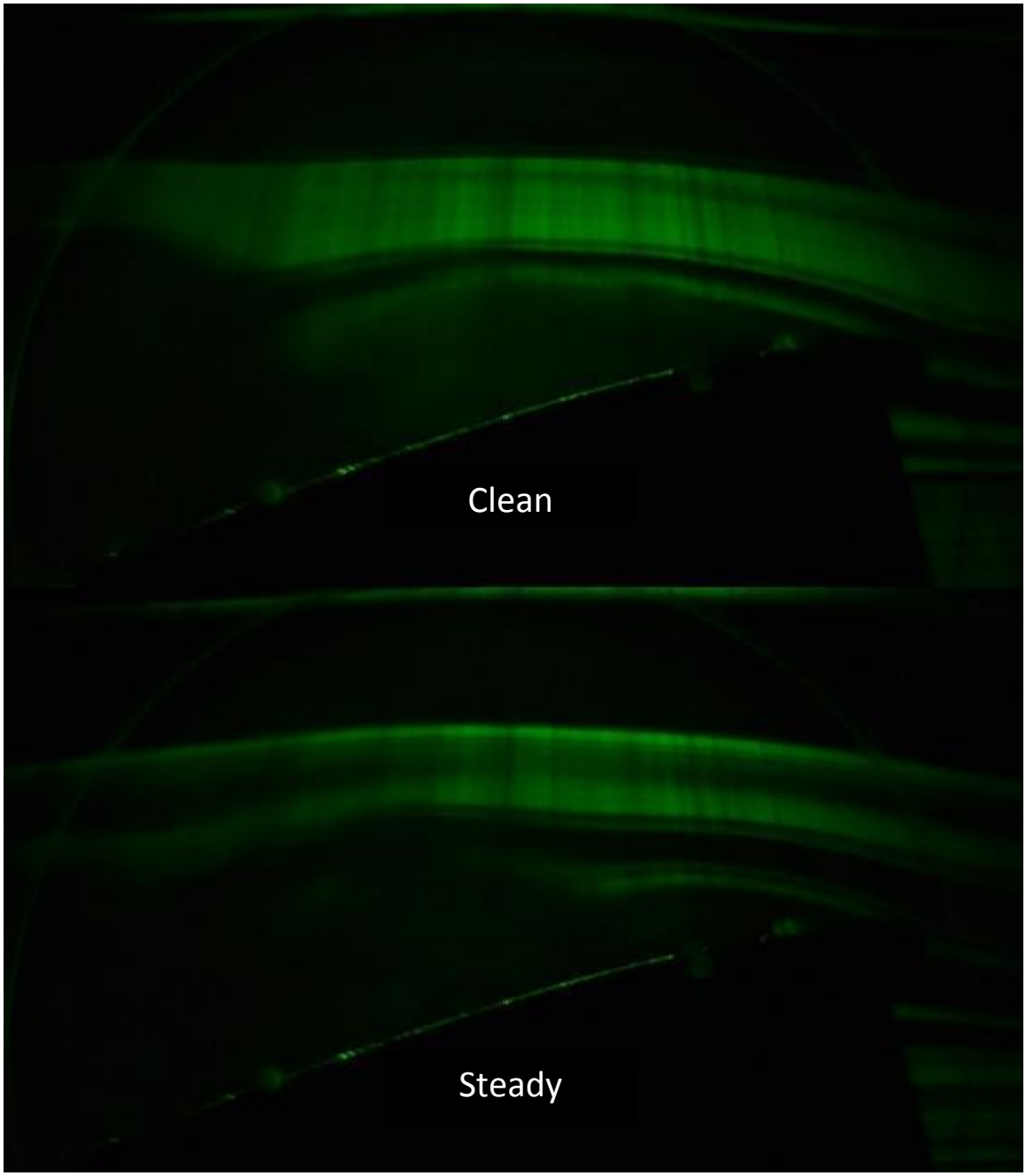

Figure 81: Re = 100,000 α = 15° Clean vs Steady

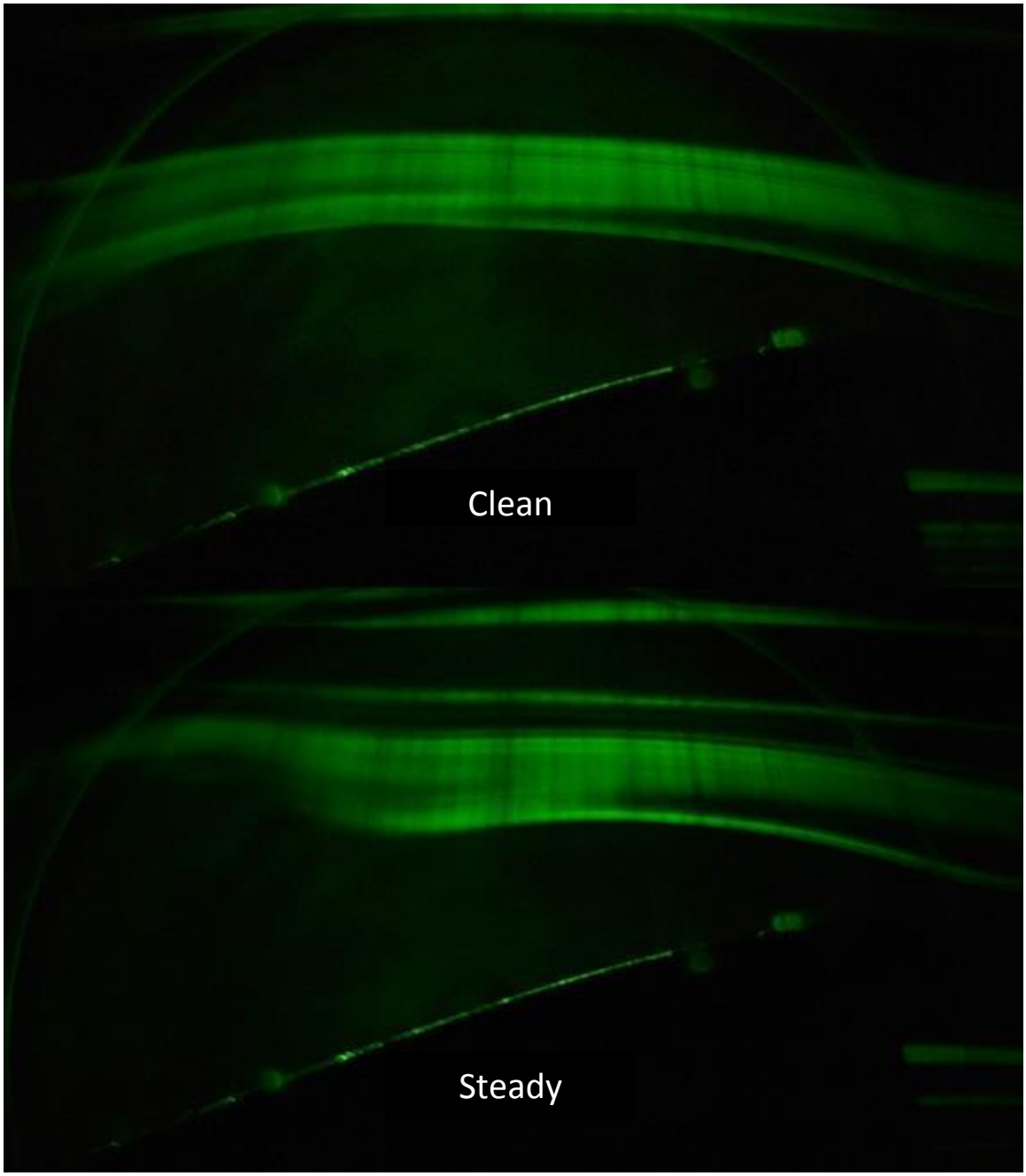

Figure 82: Re = 100,000 α = 16° Clean vs Steady

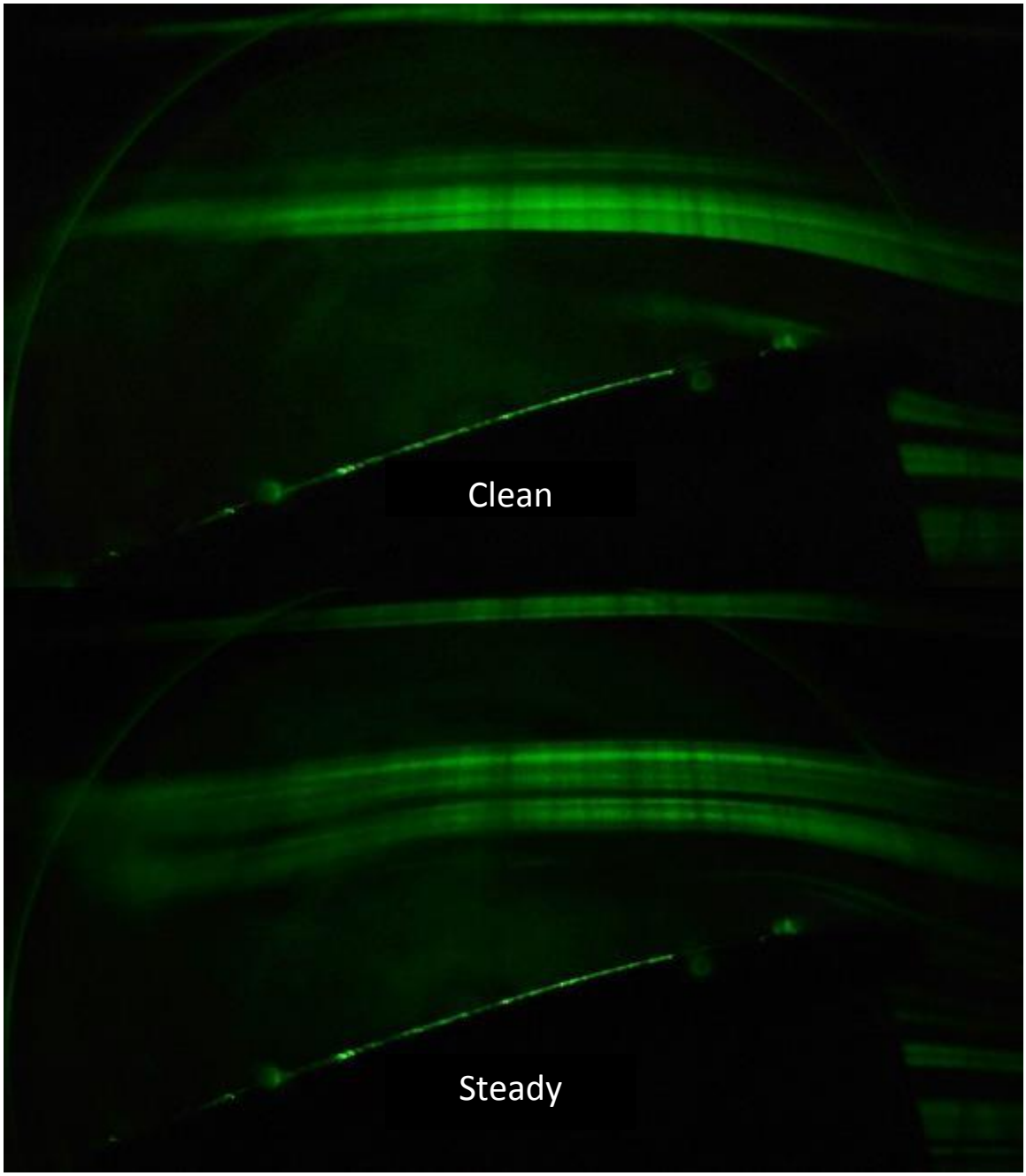

Figure 83; Re = 125,000 α = 15° Clean vs Steady

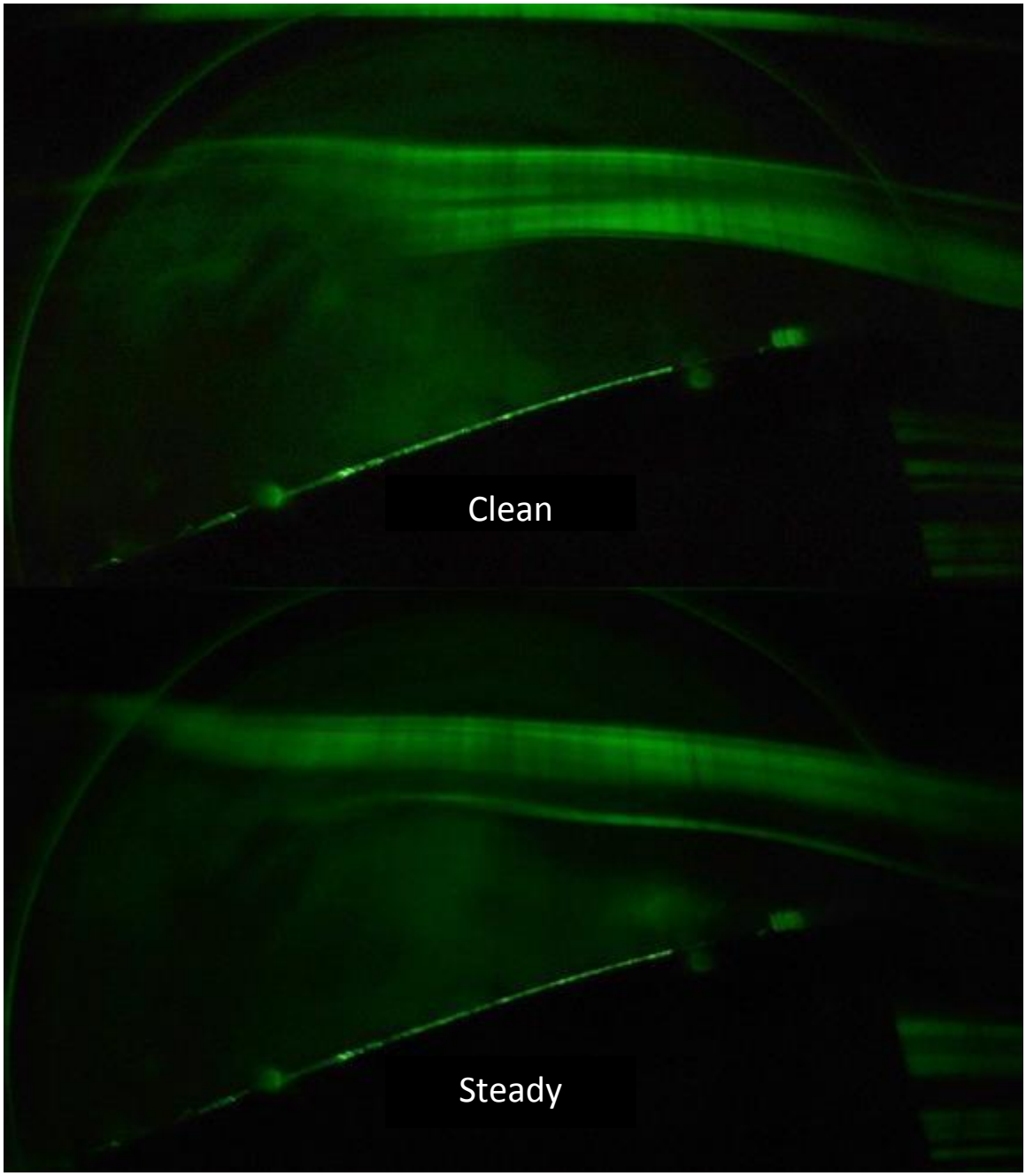

Figure 84: Re = 125,000 α = 16° Clean vs Steady

DBD & DR Comparison

The following is a comparison of some of the results from DBD testing and DR testing performed by Vinay Jakkali [51]. Figure 85 shows a comparison between the instantaneous representative images for both DBD and DR flow control methods at Reynolds number of 25,000 and angle of attack of 16°. It can readily be seen that for both the DBD and DR the flow detaches at or near the leading edge for the clean case. However, the pulsing frequencies for both DBD and DR methods appear to show some flow control. This tends to indicate that for these specific cases the flow control authority of both systems is comparable. Figure 86 shows a comparison of the instantaneous representative images for both DBD and DR methods for Reynolds number of 50,000 at angle of attack of 16°. In Figure 86 the last image for DR is operating at 87 Hz, which is the higher operating frequency for the DR system as currently constructed, whereas the operating frequency for the DBD is 90 Hz. As Discussed in the DBD results section the flow is separated for the clean case and exhibits an oscillatory behavior of attached and separated for various operating frequencies of the plasma. From the DR images, it appears that the DR keeps the flow attached longer with flow separating near half-chord. This could be indicative of the DR case also exhibiting oscillatory behavior or possibly due to DR having a longer actuation surface in the chord wise direction but it is inconclusive; it is however, apparent that both systems have an effect on the flow at this operating regime.

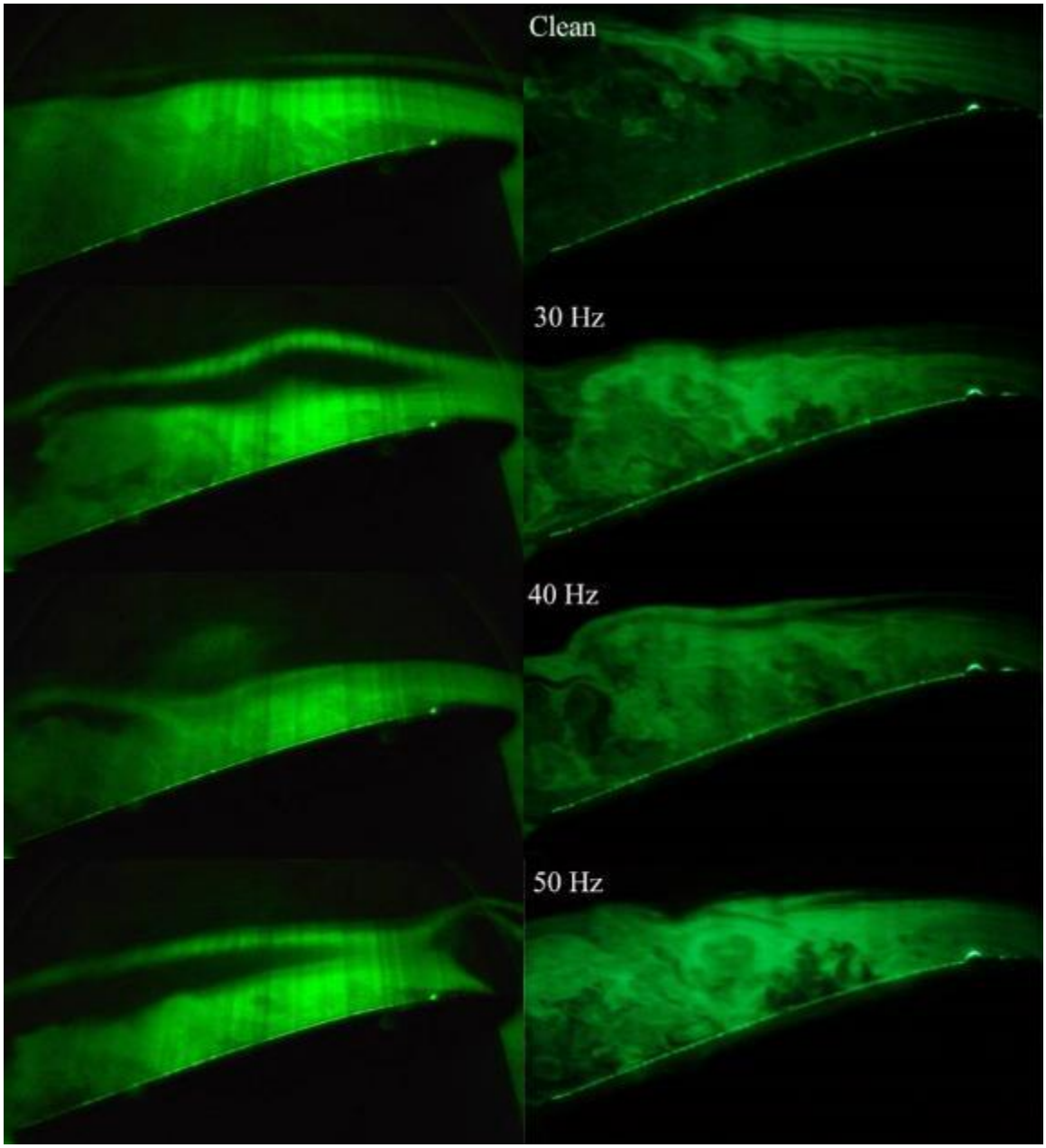

Figure 85: Re = 25,000 α = 16° low power DBD (left) vs DR (right) [51]

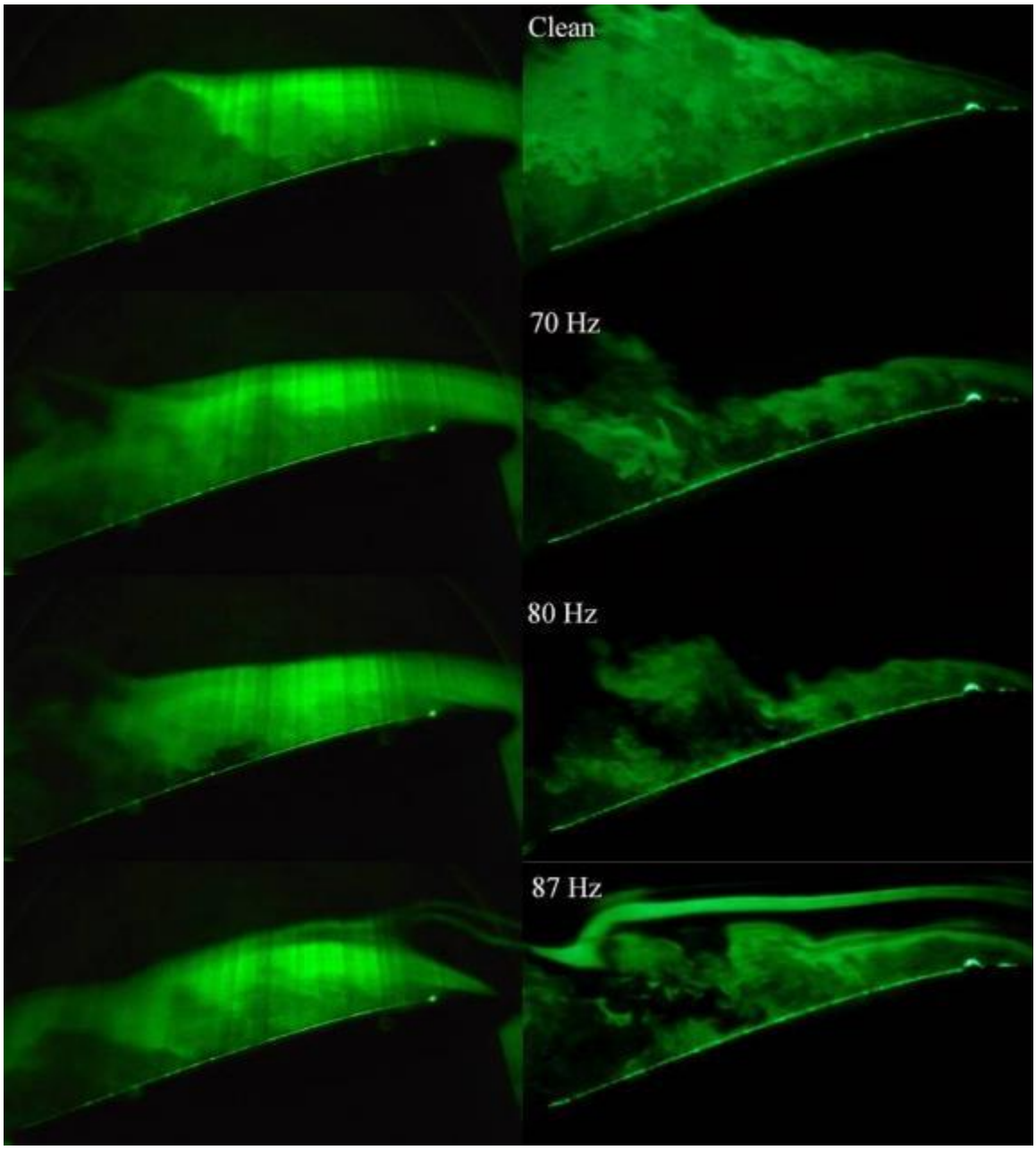

Figure 86: Re = 50,000 α = 16° low power DBD (left) vs DR (right) [51]

Conclusions and Recommendations

In the present work, it is clear that DBD tends to have a greater effect on the flow for the lower studied Reynolds numbers of 25,000 and 50,000 than at higher Reynolds numbers of 75,000 through 125,000. For combinations of angles of attack and Reynolds numbers that exhibit oscillatory behavior (oscillating between attached and separated somewhere along the upper surface), the compiled and individual images tend to show that DBD can either attach the flow or bias the oscillatory mode towards being attached more often than it is separated in comparison to the clean case. At angles of attack for which the flow is fully separated, the DBD is often able to induce an oscillatory behavior. When DBD is compared to dynamic roughness it appears to have the same region of effectiveness for low Reynolds number $\mathcal{O}(10^4)$ flow. DBD exhibits relatively low power operation, with the operating power for this testing being about 2.9 W (≈57 W/m) for the low power testing and about 9.6 W (≈188 W/m) for the high power testing. Depending upon the method of construction, geometry, and applied voltage potential, DBD actuators can exhibit extremely short lifecycles.

DBD systems compare well in many ways to other active flow control strategies such as DR. Both DR and DBD have advantages and disadvantages for their applications to UAV's and other aircraft. Some of the of benefits utilizing DBD actuators other than their aerodynamic performance qualities include potential uses for the prevention of wing icing, sonic-boom suppression in transonic regimes through local heating, radar cross section mitigation, and electromagnetic pulse protection. Other attractive qualities of DBD include their ease of application to existing aircraft platforms and their wide flexible range of operations concerning electrical characteristics such as voltage, frequency, and dielectric material and geometrical characteristics such as span wise width, gap width, dielectric thickness, etc. The relatively low power consumption of the DBD actuator is another feature that makes it a favorable active flow control method. Where the operating power of the actuators in this study being run in steady mode were approximately

2.9 W for low power or 9.6 W for high power. This is in comparison to approximately 85 W for the motored piston-cylinder engine that ran DR at its lowest setting, where the control knob was set at one on a scale of one through 10. Additionally, while the DBD is operating in the 50% duty cycle pulsing mode, the power requirement is approximately half its constant-operation power draw. It has also been demonstrated by other researchers that it is possible to implement DBDs for use a UAVs through the utilization of battery packs and lightweight HV frequency generators.

One of the most significant problems with DBD actuators for flow control is their tendency to degrade during operation to the point of failure. This degradation and arcing of the actuators was a source of many problems during the current experimental testing that was eventually combated by using an actuator with a negligible gap for the majority of the testing. This selection in turn allowed for operation at lower voltages and extended the lifetime of the actuator. Decreasing gap width, however, reduced the induced velocity of the plasma and decreased the total momentum injection into the flow, which is likely the reason the DBD showed results of no effect at the higher Reynolds numbers tested, even though other researchers at higher gaps and voltages have reported positive results in these flow regimes. Some researchers have combated the degradation of the dielectric barrier by using glass-based dielectrics that appear not to degrade even after extended operations [52]. However, these glass-based dielectrics reduce the ease of application to wing surfaces in comparison to tape based dielectrics such as Kapton tape used in this study.

Aside from its aerodynamic characteristic modification capabilities, the benefits of application of DR include its ability to de-ice a wing and prevent the formation of ice during operation. Some limitations that can be encountered with DR include its limited frequency range, which prevents it from operating at significantly higher frequencies/Reynolds numbers, moving parts that tend to degrade, and the requirement of significant modifications to existing internal wing structures.

Dielectric barrier discharge is a form of active flow control that offers a low power requirement form of flow control with a wide range of applications and operating characteristics. However, DBD systems need to be studied more to improve their overall robustness and applicability for the use on UAVs and manned aircraft. The primary conclusions of this research indicate that for the tested DBD flow control system,

- Low power (57 W/m) gapless DBD actuators work for low Reynolds number $\dot{O}(10^4)$ flow separation control at angles of attack near separation for a wing with no form of flow control.
- DBDs are comparable in flow control authority to other periodic forcing methods of flow separation control, specifically DR.
- low power gapless DBD's ability to control separation at moderate Reynolds numbers $\dot{O}(10^5)$ can be intermittent or unsuccessful depending on angle of attack.
- DBD actuators with a significant gap that require higher power to operate show potential to control flow at higher Reynolds numbers than gapless DBDs.
- Geometry, operating power, and materials used for construction of DBDs can greatly influence their lifecycle, which can vary from fractions of a second to running indefinitely.
- With the utilization of more robust dielectric barriers that prevent arcing, allow for operation at higher voltage and do not degrade, the applicability of DBD's to existing aircraft with minor modifications seems promising for the future.

Due to these experimental observations and literature findings, it is recommended that future tests should be carried out over higher Reynolds numbers and higher angles of attack with actuators that use different dielectric materials that allow for operation with a wider gap and higher voltage for prolonged periods of time to provide greater flow control authority. It is recommended to use a faster shutter speed to obtain clearer, more, "instantaneous" images for image compiling. It is also recommended to use high speed, high definition video during testing to better document the flow behavior. Video could also be

used to investigate the frequency of the oscillatory behavior of the flow that was witnessed during this experimental work.

References

[1] P. B. S. Lissaman, "Low-Reynolds Number Airfoils," vol. 15, 1983.

[2] I. Tani, "Low-speed Flows Involving Bubble Separations," vol. 5, 1964.

[3] L. Nisiparu and R. Cramariuc, "Contribution About the Electrohydrodynamic Spraying," vol. 71, no. 3, 2009.

[4] T. C. Corke, M. L. Post and D. M. Orlov, "SDBD Plasma Enhanced Aerodynamics: Concepts, Optimization and Applications," 2007.

[5] M. Forte, J. Jolibois, J. Pons, E. Moreau, T. G. and M. Cazalens, "Optimization of a Dielectric Barrier Discharge Actuator by Stationary and Non-Stationary Measurements of the Induced Flow Velocity: Application to Airflow Control," 2007.

[6] F. O. Thomas, T. C. Corke, M. Iqbal, A. Kozlov and D. Schatzman, "Optimization of Dielectric Barrier Discharge Plasma Actuators for Active Aerodynamic Flow Control," vol. 47, no. 9, 2009.

[7] J. R. Roth and X. Dai, "Optimization of the Aerodynamic Plasma Actuator as an Electrohydrodynamic (EHD) Electrical Device," Reno, 2006.

[8] J. Jolibois, M. Forte and E. Moreau, "Application of an AC barrier discharge actuator to control airflow separation above a NACA 0015 airfoil: Optimization of the actuation location along the chord," 2008.

[9] R. Sosa, H. Kelly, D. Grondona, A. Marquez, V. Lago and G. Artana, "Journal of Physics D: Applied Physics: Electrical and Plasma Characteristics of a Quasi-Steady Sliding Discharge," vol. 41, 2008.

[10] N. Bernard, A. Mizuno and E. Moreau, "A large-scale multiple dielectric barrier discharge actuator based on an innovative three-electrode design," 2009.

[11] N. Bernard, J. Jolibois and E. Moreau, "Lift and drag performances of an axisymmetric airfoil controlled by plasma actuator," 2009.

[12] J. Little, K. Takashima, M. Nishihara, I. Adamovich and M. Sammy, "Separation Control with Nanosecond Pulse Driven Dielectric Barrier Discharge Plasma Actuators," 2011.

[13] D. Roupassav, A. Nikipelov, M. Nudnova and A. Y. Starikovskii, "Flow separation control by plasma actuator with nanosecond pulse periodic discharge," 2008.

[14] D. Andreoli, M. Cassaro, M. Battipede, G. Ahmadi and P. Marzocca, "Experimental Investigation on a 3D Wing Section Hosting Multiple SJAs for Stall Control Purpose," 2015.

[15] T. Grager, "Experimental study of low reynolds number flow control devices: Dynamic burst control plate and dynamic roughness," ProQuest Dissertations and Theses, 2011.

[16] V. Jakkali, W. Huebsch, A. Robert, S. Hamburg and P. Browning, "Investigation of Dynamic Roughness Flow Control On NACA 0012 Airfoil at Low Reynolds Number," 2013.

[17] M. N. Hirsh and H. Oskam, Gaseous Electronics: Electrical Discharges, vol. 1, New York: Academic Press, 1978.

[18] P. Bellan, "Fundamentals of Plasma Physics," 2008.

[19] T. Boyd and J. Sanderson, "The Physics of Plasmas," 2003.

[20] U. Kogelschatz, "Fundamentals and applications of Dielectric-Barrier Discharges," ABB Corporate Research, Switzerland, 2000.

[21] E. Husain and R. S. Nema, "IEEE Transactios on Electrical Insulation: Analysis of Paschen Curves of Air, N2 and SF6 Useing the Townsend Breakdown Equation," Vols. EI-17, 1982.

[22] P. B. Sankar, "Measurement of Air Breakdown Voltage and Electric Field Using Standard Sphere Gap Method," National Insititute of Technology, Rourkela, India, 2011.

[23] D. F. Opaits, "Dielectric Barrier Discharge Actuator for Flow Control," National Aeronautics and Space Administration, Ohio, 2012.

[24] J. W. Ferry, "Thrust Measurement of Dielectric Barrier Discharge Plasma Actuators and Power Requirements for Aerodynamic Control," Missouri University of Science and Technology, 2010.

[25] M. Laroussi, I. Alexeff, P. Richardson and F. F. Dyer, "IEEE Transactions on Plasma Science: The Resisitive Barrier Discharge," vol. 30, 2002.

[26] J. H. Choi, I. Han, H. K. Baik, M. H. Lee, D.-W. Han, J.-C. Park, I.-S. Lee, K. M. Song and Y. S. Lim, "Analysis of Sterilization Effect by Pulsed Dielectric Barrier Discharge," 2005.

[27] C. Wilson, T. Giddings and P. Smith, "The Use of Barrier Discharge for Pollution Control," 1997.

[28] E. P. A. United States, "Using Non-thermal Plasma to Control Air Pollutants," U.S EPA, 2005.

[29] A. Y. Starikovskii, N. B. Anikin, I. N. Kosarev, E. I. Mintoussov, S. M. Starikovskaia and V. P. Zhukov, "Plasma-assisted combustion," vol. 78, 2006.

[30] A. Vincent-Randonnier, S. Larigaldie, P. Magre and V. Sabel'nikov, "Plasma assisted combustion: effect of a coaxial DBD on a methane diffusion flame," 2007.

[31] G. Borcia, C. A. Anderson and N. M. D. Brown, "Dielectric Barrier Discharge for Surface Treatment: Application to Selected Polymers in Film and Fibre Form," 2003.

[32] J. R. Roth, "Method and Apparatus for Covering Bodies With a Uniform Glow Discharge Plasma and Applications Thereof". United States of America Patent 5,669,583, 23 September 1997.

[33] J. R. Roth, P. P. Tsai and C. Liu, "Steady State, Glow Discharge Plasma". United States of America Patent 5,387,842, 7 February 1995.

[34] J. R. Roth, P. P. Tsai, C. Liu, M. Laroussi and P. D. Spence, "One Atmosphere, Uniform Glow Discharge Plasma". United States of America Patent 5,414,324, 9 May 1995.

[35] S. Leonov, D. Yaranstev, V. Gromov and A. Kuriachy, "Mechanisms of Flow Control by Near-Surface Electrical Discharge Generation," 2005.

[36] C. He, "Dissertation: Plasma Slats and Flaps: an Application of Plasma Actuators for Hingeless Aerodynamic Control," University of Notre Dame, 2008.

[37] W. Yun, L. Yinghong, J. Min, S. Huimin, S. Changbing and P. Yikang, "Experimnental investigation into Characteristics of Plasma Aerodynamic Actuation Generated by Dielectric Barrier Discahrge," 2010.

[38] B. A. Gibson, M. Arjomandi and R. M. Kelso, "The Response of a Flat Plate Boundary Layer to an Orthogonally Arranged Dielectric Barrier Discharge Actuator," 2011.

[39] M. Denison and M. L., "Compressibility Effects on Dielectric Barrier Discharge Actuation and Boundary-Layer Receptivity," vol. 53, 2015.

[40] S. Im, H. Do and M. A. Cappelli, "Dielectric barrier discharge control of a turbulent boundary layer in a supersonic flow," American Institute of Physics, 2010.

[41] F. O. Thomas, A. Kozlov and T. C. Corke, "Plasma Actuators for Landing Gear Noise Reduction," 2005.

[42] F. O. Thomas, A. Kozlov and T. C. Corke, "Plasma Actuators for Cylinder Flow Control and Noise Reduction," 2008.

[43] W. Friedrichs, "Dissertation: Unmanned Aerial Vehicle for Flow Control Experiments with Dielectric Barrier Discharge Plasma Actuators," 2014.

[44] V. Chirayath and J. J. Alonso, "Plasma Actuated Unmanned Aerial Vehicle - The First Plasma Controlled Flight in History," 2011.

[45] A. V. Likhanski, M. N. Shnieder, D. F. Opaits, R. B. Miles and S. O. Macheret, "Limitations of the DBD effects on the external flow," 2010.

[46] S. Coumar, R. Jousett, J.-D. Parisse and V. Lago, "Effect of surface heating on shock wave modification by a plasma actuator in a rarefied supersonic flow over a flat plate," 2015.

[47] B. Chaudhury and S. Chaturvedi, "Study and Optimization of Plasma-Based Radar Cross Section Reduction Using Three-Dimensional Computations," 2009.

[48] Y. ZhongCai and S. JiaMing, "Research on EM pulse protection property of plasma-microwaveabsorptive material-plasma sandwich structure," 2010.

[49] K. Rinoie and N. Takemura, "Oscillating Behavior of Laminar Separation Bubbles Formed on an Aerofoil Near Stall," vol. 108, 2004.

[50] "Nikon Digital SLR Camera D5300 Specifications," Nikon Corporation, 2014. [Online]. Available: http://imaging.nikon.com/lineup/dslr/d5300/spec.htm. [Accessed December 2015].

[51] V. Jakkalli, "Parametric Flow Visualization Study of Dynamic Roughness Effects," 2015.

[52] R. E. Hanson, N. M. Houser and P. Lavoie, "Dielectric Material Degradation Monitoring of Dielectric Barrier Discharge Plasma Actuators," 2014.

[53] I. H. Abbott and A. E. Von Doenhoff, "Theory of Wing Sections Including a Summary of Airfoil Data," 1959.

[54] T. Shao, K. Long, C. Zhang, J. Wang, D. Zhang, P. Yan and S. Zhang, "Electrical Characterization of Dielectric Barrier Discharge Driven by Nanosecond Pulses in Atmospheric Air," 2009.

Appendix A: Wind Tunnel Test Section Qualification

Data Point	Probe Position (y)	$U_{profile}$	$U_{variation}$	TI
[]	[in]	[ft/s]	[%]	[%]
1	0.00	0.00	N/A	0.00
2	0.25	65.37	2.53	1.30
3	0.38	66.34	1.09	1.08
4	0.50	66.72	0.51	1.15
5	0.63	67.31	0.37	1.03
6	0.75	66.07	1.48	0.69
7	0.88	67.80	1.10	0.88
8	1.00	65.48	2.36	0.77
9	1.13	69.43	3.53	0.68
10	1.25	65.12	2.89	0.63
11	1.38	65.14	2.87	1.19
12	1.50	66.42	0.96	0.67
13	1.63	67.75	1.03	0.56
14	1.75	64.62	3.65	0.54
15	1.88	69.53	3.68	0.56
16	2.00	68.36	1.94	0.65
17	2.13	65.70	2.04	1.30
18	2.25	67.29	0.34	0.43
19	2.38	67.25	0.28	0.77
20	2.50	66.60	0.70	0.50
21	2.63	68.64	2.35	1.80
22	2.75	69.27	3.28	0.82
23	2.88	68.11	1.56	0.58
24	3.00	66.71	0.52	0.60
25	3.13	68.11	1.56	0.58
26	3.25	69.27	3.28	0.82
27	3.38	68.64	2.35	1.80
28	3.50	66.60	0.70	0.50
29	3.63	67.25	0.28	0.77
30	3.75	67.29	0.34	0.43
31	3.88	65.70	2.04	1.30
32	4.00	68.36	1.94	0.65
33	4.13	69.53	3.68	0.56
34	4.25	64.62	3.65	0.54
35	4.38	67.75	1.03	0.56
36	4.50	66.42	0.96	0.67
37	4.63	65.14	2.87	1.19
38	4.75	65.12	2.89	0.63
39	4.88	69.43	3.53	0.68
40	5.00	65.48	2.36	0.77
41	5.13	67.80	1.10	0.88
42	5.25	66.07	1.48	0.69
43	5.38	67.31	0.37	1.03
44	5.50	66.72	0.51	1.15
45	5.63	66.34	1.09	1.08
46	5.75	65.37	2.53	1.30
47	6.00	0.00	N/A	0.00
		Mean	Max Variation	Max TI
		67.06	3.68	1.80

Figure 87: Turbulence intensity and velocity profile data

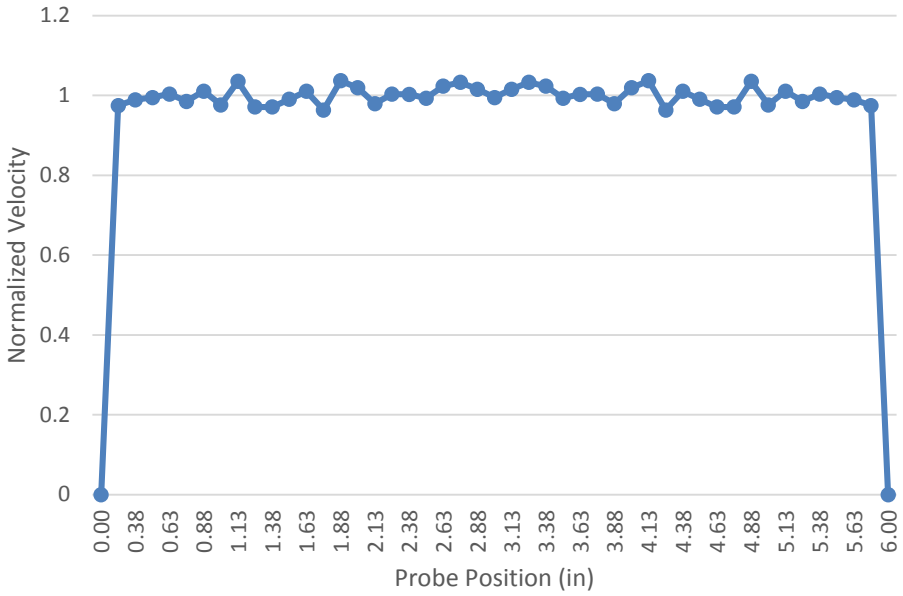

Figure 88: Velocity profile (normalized with respect to the mean)

Appendix B: Matlab Code Used in Post Processing

Image Compiling Code

```
clc
clear all
re=input('Please input reynolds number');
freq=input('Please input frequency');

for i=1:4

im=[1,10,19,28];
first_im=im(i);


% picks out first image and converts to a matrix in 32bit and sets equal to a
variable
if first_im>9

sum=uint32(imread(['C:\Users\Joseph\Pictures\re',num2str(re),'\',num2str(freq
),'hz\DSC_00',num2str(first_im),'.jpg']));

else

sum=uint32(imread(['C:\Users\Joseph\Pictures\re',num2str(re),'\',num2str(freq
),'hz\DSC_000',num2str(first_im),'.jpg']));
end

%goes to the next 8 images after the first (total of 9 images) and averages
 for n=first_im+1:first_im+8;

if n>9

sum=imadd(sum,uint32(imread(['C:\Users\Joseph\Pictures\re',num2str(re),'\',nu
m2str(freq),'hz\DSC_00',num2str(n),'.jpg'])));
 else

sum=imadd(sum,uint32(imread(['C:\Users\Joseph\Pictures\re',num2str(re),'\',nu
m2str(freq),'hz\DSC_000',num2str(n),'.jpg'])));
 end
 end

 %converts back to 8bit
 new = uint8((imdivide(sum,(9))));


 %saves compiled(averaged) image into new folder

imwrite(new,['C:\Users\Joseph\Pictures\re',num2str(re),'\',num2str(freq),'hzC
\DSC_00',num2str(aoa),'.jpg'],'jpg')

end
imshow(new)
```

Image Cropping Code

```
% inputs to find correct folder location for image
clc
clear all
r=input('Please input reynolds number');
f=input('Please input frequency');

for i=1:4
% vectors used for cycling through each picture in the folder
a=[13,14,15,16];
aoa=a(i);

% turns the picture into a matrix

im=imread(['C:\Users\Joseph\Pictures\re',num2str(r),'\',num2str(f),'hzC\DSC_0
0',num2str(aoa),'.jpg']);

% picks out the outlying matrix points for which outside of will be cropped
left=1000;
right=4500;
bottom=2500;
top=500;

% creates a new matrix from the selected points
new=im(top:bottom,left:right,:);

% turns the matrix back into a picture and saves it in the correct folder
imwrite(new,['C:\Users\Joseph\Pictures\re',num2str(r),'\',num2str(f),'hzCC\DS
C_00',num2str(aoa),'.jpg'],'jpg')

end
% shows the new cropped image
imshow(new)
```

Appendix C: Resonance Testing

Table 2: Power uncertainty data

Frequency (kHz)	I(amperes)	δI	u(I)=(δI/I)	V (volts)	δV	u(V)=(δV/V)	Power (w)	δp
1.20	0.0776	0.0001	0.0013	56	2	0.0357	4.3456	0.1553
1.25	0.0683	0.0001	0.0015	56	2	0.0357	3.8248	0.1367
1.30	0.061	0.0001	0.0016	55	2	0.0364	3.355	0.1221
1.35	0.0557	0.0001	0.0018	55	2	0.0364	3.0635	0.1115
1.40	0.0528	0.0001	0.0019	55	2	0.0364	2.904	0.1057
1.45	0.0533	0.0001	0.0019	55	2	0.0364	2.9315	0.1067
1.50	0.0571	0.0001	0.0018	55	2	0.0364	3.1405	0.1143
1.55	0.0611	0.0001	0.0016	55	2	0.0364	3.3605	0.1223
1.60	0.065	0.0001	0.0015	57	2	0.0351	3.705	0.1301

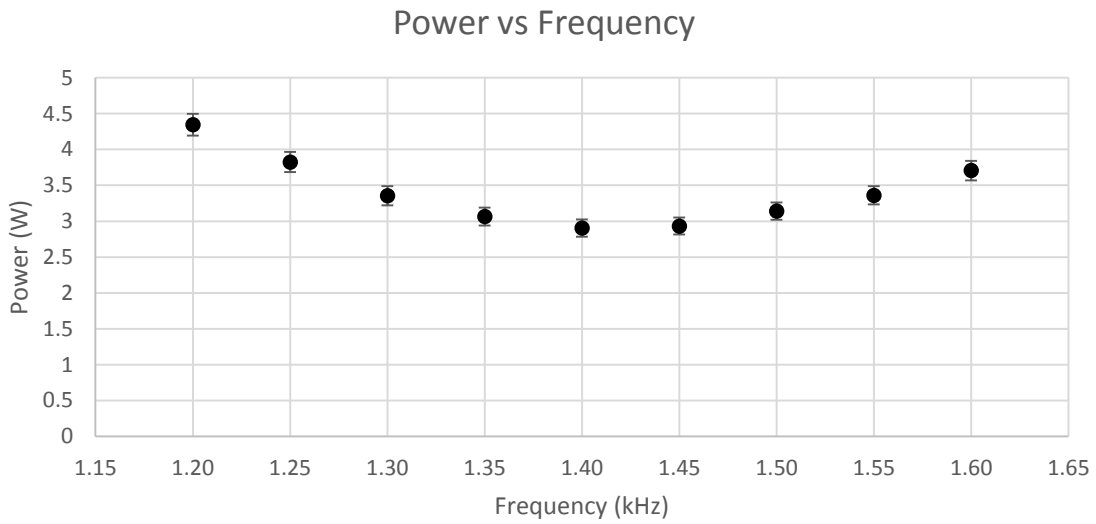

Figure 89: Resonance testing and error analysis data

Appendix D: Blockage Derivation

The blockage was calculated using Eq. (7)

$$\%BL = (100)\frac{A_{frontal}}{A_{ts}} \quad \textbf{Eq. (7)}$$

where the area of the test section is 36 in^2 and the entire cross sectional area of the model, $A_{frontal}$, is the sum of the frontal area of the wing model (variable with angle of attack) and the frontal area of the end plate (fixed value of 0.42 in^2). The frontal area of the wing model was calculated through a multistep process. Based on the chord length of 3-15/16 in. (3.9375 in.) the max thickness of the NACA 0012 can be calculated as 12% of the chord, which is 0.4725 in. in this case. Unmodified NACA four-digit series wings have maximum thickness located at 30% chord, which is 1.18125 in. from the leading edge for this model. The 30% of the chord, .3c, on the leading edge side of the location of max thickness as shown in Figure 90 and half the thickness, .06c, on the upper side of the wing at the location of half thickness as shown in Figure 90 are important for calculating blockage.

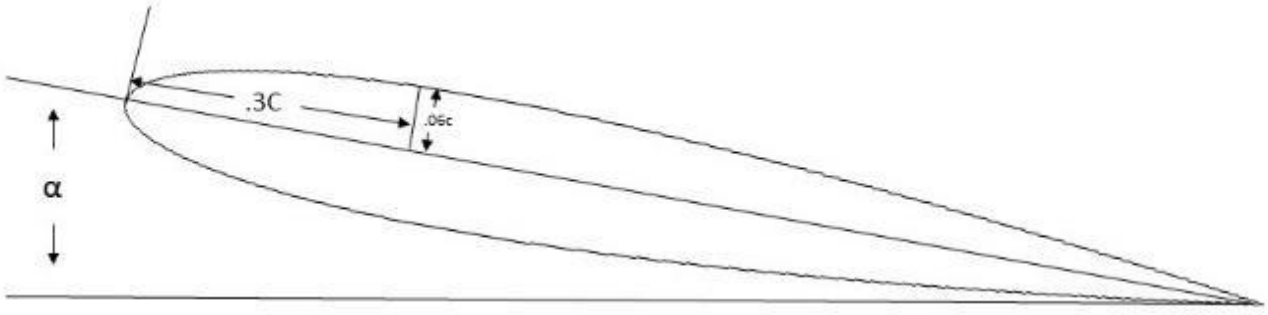

Figure 90: Wing at random angle of attack

At some angle of attack, a component of the half thickness (used because half the thickness lies above the chord line) in the positive y-direction shown as a red dotted line in Figure 91 is equal to the y-component of the 30% chord shown as a blue dotted line in Figure 91.

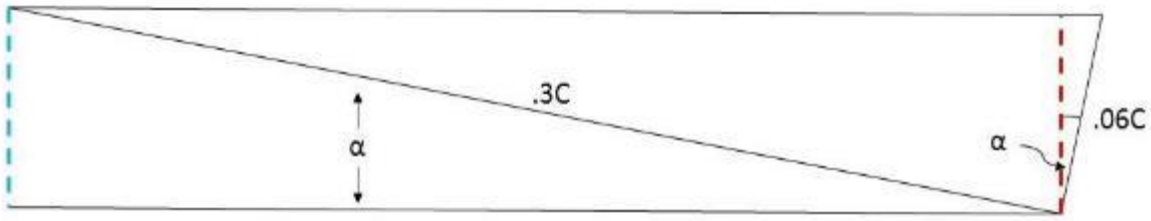

Figure 91: Zoomed in leading edge

At some angle of attack both these y-components are equal to each other and have the same frontal area. This angle can be calculated using Eq. (8)

$$\alpha = \tan^{-1}\left(\frac{.06c}{.3c}\right) \qquad \textbf{Eq. (8)}$$

For this model the angle of attack of 11.3° they are equal in their components in the positive y-direction. This means above 11.3° the leading edge is above the thickest part of the wing model. This means the frontal area can be calculated as the y component of the chord plus the y-component of leading edge radius above the tip of the leading edge of the chord (e.g. The portion of the red dotted line above the blue dotted line in Figure 92) multiplied by the model span.

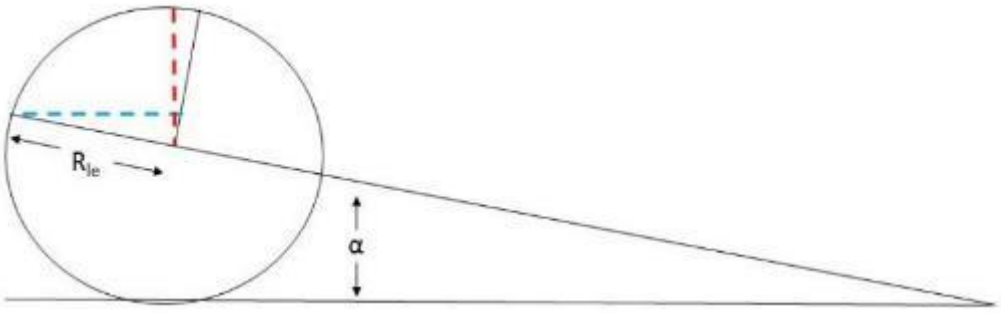

Figure 92: Leading edge radius

The leading edge radius can be calculated using Eq. (9) [53].

$$R_{le} = .0158c \quad \textbf{Eq. (9)}$$

The portion of the y-component of the radius of the leading edge above the tip of the chord tip can be calculated by using Eq. (10)

$$R_{ley} = .0158c - .0158c(\tan(\alpha)) \quad \textbf{Eq. (10)}$$

Which for this model with a chord length of 3-(15/16) in. at an angle of attack of 16° (max angle of attack) the R_{ley} comes out to be .044 in. The y-component of the chord can be calculated using Eq. (11)

$$c_y = csin(\alpha) \quad \textbf{Eq. (11)}$$

which for this model at 16° comes out to be 1.085 in. With this number added together with the portion of the leading edge radius above the tip of the chord and multiplying by the 3 in. span the frontal area of the wing at angle of attack of 16° can be calculated to be 3.387 in^2. Adding this to the frontal area of the end disk, the total $A_{frontal}$ from Eq. (7) can be calculated to be 3.807 in^2. Using Eq. (7) with the test section area, A_{ts}, equal to 36 in^2 the blockage can be calculated to be 10.57±.41% for an angle of attack of 16°. The uncertainty in the blockage is calculated in Appendix E.

Appendix E: Uncertainty Analysis

Uncertainty for Power Calculations

The uncertainty in the power consumption was calculated using the method commonly used, known as addition in quadrature, for variables in equations that are multiplied or divided. This can be seen in Eq. (12) where the u() of a variable represents the relative uncertainty which is defined, for any measured quantity a with an uncertainty of δa, by Eq.(13)

$$u(p)^2 = u(I)^2 + u(V)^2 \quad \textbf{Eq. (12)}$$

$$u(a) = \delta a/a \quad \textbf{Eq. (13)}$$

Combining Eq. (12) and Eq. (13), Eq. (14) can be derived for the uncertainty in power consumption, δp.

$$\frac{\delta p}{p} = \sqrt{(\frac{\delta I}{I})^2 + (\frac{\delta V}{V})^2} \quad \textbf{Eq. (14)}$$

An example of the use of this equation can be seen in Eq. (15) which is the data used from frequency of 1400Hz (the resonant frequency for this circuit). All the uncertainty data in appendix C was calculated using this method.

$$\delta p = 2.904\sqrt{(\frac{.0001}{.0528})^2 + (\frac{2}{55})^2} \cong .106 \quad \textbf{Eq. (15)}$$

Uncertainty for Reynolds Number

This section presents the measured or calculated value for the variables used in calculating uncertainty in the Reynolds number. The tabulated data for uncertainty in the free stream velocity and resulting Reynolds number uncertainty are shown in Table 3 and Table 4. This section will show the process and equations used for calculating uncertainty in the Reynolds number.

Table 3: Measured and calculated constants for experimental testing and uncertainty analysis

	$P_{ambiant}$ (millibar)	T (K)	ρ(kg/m^3)	A_2(in^2)	A_1(in^2)	(A_2/A_1)	C (in)
measured/calculated value	989	293	1.176	36	342.25	0.10519	3.9375
δ measured/calculated value	0.5	0.5	0.002	0.26517	0.81759	0.00081	0.0313

Table 4: Uncertainty in free stream velocity and Reynolds number

ΔP(in H_2O)	δΔP	$U_{nominal}$(m/s)	$U_{measured}$(m/s)	$\delta U_{measured}$	Re	δRe
0.04	0.01	3.93	4.14	0.518	25,000	3138
0.14	0.01	7.85	7.74	0.283	50,000	1872
0.32	0.01	11.78	11.70	0.204	75,000	1445
0.57	0.01	15.7	15.62	0.183	100,000	1428
0.9	0.01	19.63	19.62	0.188	125,000	1570

The nominal velocity in Table 4 was the velocity calculated to reach the required nominal Reynolds number from Eq. (16).

Starting with Eq. (16), the equation for Reynolds number and plugging in Eq. (17) the equation of state, Eq. (18) can be derived.

$$Re = \frac{\rho UC}{\mu} \quad \textbf{Eq. (16)}$$

$$\rho = \frac{P_a}{RT} \quad \textbf{Eq. (17)}$$

$$Re = \frac{P_a UC}{\mu RT} \quad \textbf{Eq. (18)}$$

Every variable in Eq. (18) was directly measured except for the free stream velocity *U*, so in order to calculate the uncertainty in the Reynolds number the uncertainty in *U* must first be calculated. The free stream velocity was calculated by utilizing the equation for mass conservation, Eq. (19), the Bernoulli equation, Eq. (20), and the identity Eq. (21) to derive Eq. (22). Eq. (23) shows an example of using Eq. (22) to calculate the free stream velocity for a nominal Reynolds number of 25,000.

$$\rho A_1 U_1 = \rho A_2 U_2 \qquad \textbf{Eq. (19)}$$

$$P_1 + \frac{1}{2}\rho U_1^2 + \rho g h_1 = P_2 + \frac{1}{2}\rho U_2^2 + \rho g h_2 \qquad \textbf{Eq. (20)}$$

$$\Delta P = P_1 - P_2 \qquad \textbf{Eq. (21)}$$

$$U = \sqrt{\frac{2\Delta P}{\rho(1-(\frac{A_1}{A_2})^2)}} \qquad \textbf{Eq. (22)}$$

$$U = \sqrt{\frac{2(248.48).04}{1.176(1-(\frac{36}{342.25})^2)}} \cong 4.14 \qquad \textbf{Eq. (23)}$$

In Eq. (23) ΔP term is multiplied by 248.84 to convert from in. of water to Pascals, which does not affect the uncertainty. Since the equation for the free stream velocity involves square roots and powers, calculating the uncertainty cannot be done with just addition in quadrature. For any calculated quantity $a$that is in the form of Eq. (24), its uncertainty can be calculated using Eq. (25).

$$a = X^n \qquad \textbf{Eq. (24)}$$

$$\frac{\delta a}{|a|} = |n|\frac{\delta X}{|X|} \qquad \textbf{Eq. (25)}$$

starting with the area ratio in the denominator of Eq. (22) the uncertainty of the area ratio can be calculated using Eq. (26). Eq. (27) shows how the actual uncertainty was calculated as an example.

$$\delta A_r = A_r \sqrt{(\frac{\delta A_1}{A_1})^2 + (\frac{\delta A_2}{A_2})^2} \quad \textbf{Eq. (26)}$$

$$\delta A_r = .105 \sqrt{(\frac{.265}{36})^2 + (\frac{.818}{342.25})^2} \cong .0008 \quad \textbf{Eq. (27)}$$

With the uncertainty of the area ratio calculated and using Eq. (25), Eq. (28) can be derived to calculate the uncertainty in the square of the area ratio denoted as δA_r^* where A_r^* is used to denote the square of the area ratio. Eq. (29) gives an example of the calculation.

$$\delta A_r^* = 2A_r^* \frac{\delta A_r}{A_r} \quad \textbf{Eq. (28)}$$

$$\delta A_r^* = 2(.011) \frac{.0008}{.105} \cong .0002 \quad \textbf{Eq. (29)}$$

Using Eq. (17), the equation of state, and addition in quadrature, Eq. (30) can be derived to calculate the uncertainty in density, $\delta\rho$. Eq. (31) gives an example of the calculation with the parameters that were used during testing.

$$\delta\rho = \rho \sqrt{(\frac{\delta P_a}{P_a})^2 + (\frac{\delta T}{T})^2} \quad \textbf{Eq. (30)}$$

$$\delta\rho = 1.176 \sqrt{(\frac{.5}{989})^2 + (\frac{.5}{293})^2} \cong .002 \quad \textbf{Eq. (31)}$$

Now with all the variables used in calculating the uncertainty in the velocity, it can finally be calculated using Eq. (32). Eq. (33) is an example of the calculation for a nominal Reynolds number of 25,000.

$$\delta U = U \left(\frac{1}{2}\right) \sqrt{(\frac{\delta \Delta P}{\Delta P})^2 + (\frac{\delta \rho}{\rho})^2 + (\frac{\delta A_r^*}{A_r^*})^2} \quad \textbf{Eq. (32)}$$

$$\delta U = 4.14 \left(\frac{1}{2}\right) \sqrt{(\frac{.01}{.04})^2 + (\frac{.002}{1.176})^2 + (\frac{.0002}{.011})^2} \cong .518 \quad \textbf{Eq. (33)}$$

With the calculated uncertainty in the free stream velocity and the known uncertainty from the other measured terms the uncertainty in the Reynolds number can finally be calculated using Eq. (34). Eq. (35) shows an example of the calculation for nominal Reynolds number of 25,000.

$$\delta Re = Re\sqrt{(\frac{\delta P_a}{P_a})^2 + (\frac{\delta U}{U})^2 + (\frac{\delta C}{C})^2 + (\frac{\delta T}{T})^2} \quad \textbf{Eq. (34)}$$

$$\delta Re = 25{,}000\sqrt{(\frac{.5}{989})^2 + (\frac{.518}{4.14})^2 + (\frac{.03}{3.9})^2 + (\frac{.5}{293})^2} \cong 3138 \quad \textbf{Eq. (35)}$$

Uncertainty for Blockage

Starting with Eq. (7) used in calculating the blockage in the test section an uncertainty in the blockage can be calculated. In the blockage derivation section it was shown that the blockage is a function of the frontal area of the model which is the sum of the wing models y-component and the end plate disk frontal area. The uncertainty in the frontal area of the endplate can be calculated using addition in quadrature as show in Eq. (37) where W_d is the width of the end plate disk, $D_d$is the diameter of the end plate disk, and $A_d$is the frontal area of the disk as calculated by Eq. (36). Eq. (38) is the actual uncertainty calculation for the end plate disk frontal area.

$$A_d = W_d D_d \quad \textbf{Eq. (36)}$$

$$\delta A_d = A_d\sqrt{(\frac{\delta W_d}{W_d})^2 + (\frac{\delta D_d}{D_d})^2} \quad \textbf{Eq. (37)}$$

$$\delta A_d = .42\sqrt{(\frac{\frac{1}{64}}{\frac{3}{32}})^2 + (\frac{\frac{1}{32}}{4.5})^2} \cong .07 \quad \textbf{Eq. (38)}$$

To calculate the uncertainty in the y-component of the model, Eq. (11) from the derivation of blockage must be utilized along with Eq. (39), the rule to calculate uncertainty in trigonometry function, specifically

for sine, to derive Eq. (40). It must also be known that there was an uncertainty of .5° in the angle of attack (α).

$$\delta \sin(\alpha) = \sin(\alpha + \delta\alpha) - \sin(\alpha) \quad \textbf{Eq. (39)}$$

$$\delta C_y = C_y \sqrt{(\frac{\delta C}{C})^2 + (\frac{\sin(\alpha+\delta\alpha)-\sin(\alpha)}{\sin(\alpha)})^2} \quad \textbf{Eq. (40)}$$

$$\delta C_y = 1.085 \sqrt{(\frac{.03}{3.94})^2 + (\frac{\sin(16+.5)-\sin(16)}{\sin(16)})^2} \cong .0341 \quad \textbf{Eq. (41)}$$

Now to calculate the uncertainty in the y-component of the leading edge radius that is above the tip of the chord, Eq. (10) from the derivation of blockage must be used and following the same rule for tangent as was used for sine Eq. (42) can be derived. In Eq. (42) the uncertainty in the radius of the leading edge, δR_{le}, is the same as the uncertainty in the chord. Eq. (43) is the calculation of the actual uncertainty.

$$\delta R_{ley} = R_{ley} \sqrt{(\frac{\delta R_{le}}{R_{le}})^2 + (\frac{\tan(\alpha+\delta\alpha)-\tan(\alpha)}{\tan(\alpha)})^2} \quad \textbf{Eq. (42)}$$

$$\delta R_{ley} = .044 \sqrt{(\frac{.03}{.06})^2 + (\frac{\tan(16+.5)-\tan(16)}{\tan(16)})^2} \cong .022 \quad \textbf{Eq. (43)}$$

Using addition in quadrature for the summation of the uncertainties in radius of the leading edge y-component and the model chord y-component, the total uncertainty in the wing y-component, δY_{wing}, can be calculated by Eq. (44) with the actual calculation shown in Eq. (45).

$$\delta Y_{wing} = \sqrt{(\delta R_{ley})^2 + (\delta C_y)^2} \quad \textbf{Eq. (44)}$$

$$\delta Y_{wing} = \sqrt{.022^2 + .0341^2} \cong .041 \quad \textbf{Eq. (45)}$$

With the uncertainty in the span, δS, known to be (1/32) in. the uncertainty in the entire frontal area uncertainty, δA_{wing}, can be calculated using Eq. (46). Eq. (47) is the calculation of the uncertainty in the frontal area.

$$\delta A_{wing} = A_{wing}\sqrt{(\frac{\delta Y_{wing}}{Y_{wing}})^2 + (\frac{\delta S}{S})^2} \quad \textbf{Eq. (46)}$$

$$\delta A_{wing} = 3.387\sqrt{(\frac{.041}{1.13})^2 + (\frac{\frac{1}{32}}{3})^2} \cong .128 \quad \textbf{Eq. (47)}$$

With the uncertainty in the wing frontal area and the end plate disk uncertainty combining them gives the total frontal area uncertainty for the model setup. Eq. (48) shows the equation used to combine the uncertainties and Eq. (49) is the calculation carried out.

$$\delta A_{frontal} = \sqrt{(\delta A_{wing})^2 + (\delta A_d)^2} \quad \textbf{Eq. (48)}$$

$$\delta A_{frontal} = \sqrt{(.128)^2 + (.07)^2} \cong .146 \quad \textbf{Eq. (49)}$$

With the uncertainty in the frontal area of the whole model known and with the uncertainty in the test section equal to the uncertainty in A_2 in Table 3 the uncertainty in the percent blockage can finally be calculated using Eq. (50) and is calculated in Eq. (51).

$$\delta\%BL = \%BL\sqrt{(\frac{\delta A_{frontal}}{A_{frontal}})^2 + (\frac{\delta A_{ts}}{A_{ts}})^2} \quad \textbf{Eq. (50)}$$

$$\delta\%BL = 10.57\sqrt{(\frac{.146}{3.807})^2 + (\frac{.265}{36})^2} \cong .41 \quad \textbf{Eq. (51)}$$